

# Observing Cooperative Behavior with Molecular Surface Structures

**Inauguraldissertation**

zur

Erlangung der Würde eines Doktors der Philosophie

vorgelegt der

Philosophisch-Naturwissenschaftlichen Fakultät

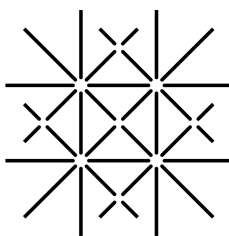
der Universität Basel

von

Manfred Matena

aus Essen (Deutschland)

Basel, 2009



UNI  
BASEL

Genehmigt von der Philosophisch-Naturwissenschaftlichen Fakultät auf Antrag von

Prof. Dr. Hans-Joachim Güntherodt

PD Dr. Meike Stöhr

Prof. Dr. Lutz H. Gade

Dr. Thomas A. Jung

Basel, den 15.09.2009

Prof. Dr. Eberhard Parlow, Dekan

# Zusammenfassung

Leitthema dieser Arbeit ist das Wechselspiel adsorbierter Moleküle untereinander sowie mit der Oberfläche im Ultrahochvakuum (UHV).

Kapitel 3 behandelt die molekulare Erkennung durch Wasserstoffbrücken (H-Brücken). Aufbauend auf einem in Supramolekularer Chemie bekannten H-Brückenmotiv wird die Selbstorganisation dreier Moleküle auf Ag(111) untersucht. In weiteren Experimenten, die sich auf eines dieser Moleküle konzentrieren, wird die durch Wärmezufuhr verursachte Umformung eines porösen Netzwerks in ein dichtgepacktes Netzwerk beobachtet. Untersuchungen mittels Rastertunnelmikroskopie (STM) und Beugung langsamer Elektronen (LEED) zeigen, dass beide Oberflächenstrukturen wohlgeordnet und kommensurabel zum Ag-Substrat sind. Dabei ist der Übergang zur dichtgepackten Struktur durch eine Änderung der Molekülkonformation gekennzeichnet, die in Lösung nicht beobachtet wird.

Kapitel 4 widmet sich Untersuchungen des Perylenderivats 1,3,8,10-Tetraazaperyren (TAPP) auf Cu(111). TAPP zeichnet sich durch Bildung verschiedener Oberflächenstrukturen aus, die durch unterschiedliche Wechselwirkungen zwischen den Molekülen charakterisiert sind. Oberflächenstrukturen, die durch schwache van-der-Waals-Kräfte zwischen den Molekülen ausgebildet werden, werden bei Wärmezufuhr durch ein wohlgeordnetes, zum Cu-Substrat kommensurables poröses Netzwerk abgelöst, dessen Molekül-Molekül-Wechselwirkung auf der Koordination freier Cu-Adatome zu den N-Atomen des TAPP basiert. Bei weiterer Wärmezufuhr bilden über kovalente C-C-Bindungen verknüpfte TAPP-Moleküle Ketten. Röntgenphotoemissionsspektroskopische Untersuchungen (XPS) und dichtefunktionaltheoretische Rechnungen (DFT) weisen auch bei den Ketten auf eine Koordination zu Cu-Adatomen hin. Erste Versuche, die Polymerisation im UHV auf zwei Dimensionen auszudehnen, deuten an, dass die fehlende Selbstkorrektur, die reversiblen Wechselwirkungen zu eigen ist, hier der Ausbildung wohlgeordneter Oberflächenstrukturen entgegenwirkt.

Die Wechselwirkung eines wohlgeordneten, porösen Netzwerks mit der Oberfläche ist Gegenstand von Kapitel 5. Dabei zeichnet sich das vom Perylenderivat 4,9-Diaminoperylen-chinon-3,10-diimin (DPDI) auf Cu(111) gebildete und auf H-Brücken basierende Netzwerk durch eine für diese Bindungsklasse ungewöhnlich hohe Stabilität aus. Insbesondere die durch spektroskopische Untersuchungen mittels stehender Röntgenwellenfelder (XSW) ermittelte Adsorptionshöhe der Moleküle spricht gegen eine starke Wechselwirkung zwischen Perylenkern und Cu-Oberfläche. Zur Erklärung der Stabilität wird darum angenommen, dass zusätzlich Cu-Adatome mit den N-Atomen der Moleküle wechselwirken. Darüber hinaus zeigen rastertunnel- (STS) und winkelaufgelöste photoelektronen-spektroskopische (ARPES) Untersuchungen, dass die periodische Störung des Cu(111)-Oberflächenzustandes zur Bildung eines (elektronischen) Energiebandes führt.



# Abstract

In the work at hand the interplay between molecules as well as molecules and substrate is studied in ultrahigh vacuum (UHV).

In Chapter 3 hydrogen-bond (H-bond) recognition, which is based on an H-bonding motif well-known in supramolecular chemistry, is investigated on Ag(111) for a three component system. Moreover, for one of the molecules a thermally induced phase transition from a porous network to a close-packed structure is found. Scanning tunneling microscopy (STM) and low energy electron diffraction (LEED) show that both surface structures exhibit long-range order and are commensurate with the Ag-substrate. In particular, this transition involves a conformational change of each molecule that is not observed in solution.

Chapter 4 deals with the study of intermolecular interactions of the perylene derivative 1,3,8,10-tetraazaperopyrene (TAPP) on Cu(111). Different surface structures are observed which exhibit different types of intermolecular interactions. Surface structures formed by TAPP molecules interacting via weak van-der-Waals forces are transformed into a long-range-ordered porous network upon annealing. For this network, which is commensurate to the substrate, the intermolecular interactions are based on the coordination of Cu-adatoms to the N-atoms of TAPP. Upon further annealing covalent C-C couplings between TAPP molecules result in the formation of chains. X-ray photoelectron spectroscopy (XPS) and computational studies using density functional theory (DFT) show that the N-atoms of the chains can coordinate to Cu-adatoms as well. Moreover, in a preliminary study the attempt was undertaken to create polymerized structures in two dimensions. However, the formation of ordered structures is a challenging task since self-correction that is inherent to weak reversible interactions is missing.

The molecule-surface interaction of a long-range-ordered porous network formed by the perylene derivative 4,9-diaminoperylene-quinone-3,10-diimine (DPDI) on Cu(111) is studied in Chapter 5. This network whose molecular building-blocks interact via H-bonds exhibits an extraordinary stability. In particular, the molecular adsorption height above the Cu surface determined by X-ray standing wave experiments (XSW) indicates that the molecular perylene core is not directly involved in a strong interaction with the surface. Thus, it is assumed that Cu-adatoms interact with the molecular N-atoms in order to explain the stability of the network. Moreover, scanning tunneling spectroscopy (STS) and angle-resolved photoemission spectroscopy (ARPES) reveal the formation of an electronic band which is induced by the periodic influence of the molecular network on the surface state of Cu(111).



# Contents

<b>Zusammenfassung</b>	<b>3</b>
<b>Abstract</b>	<b>5</b>
<b>Abbreviations and molecules</b>	<b>9</b>
<b>1 Introduction</b>	<b>11</b>
<b>2 Fundamentals</b>	<b>13</b>
2.1 X-ray standing wave absorption . . . . .	13
2.1.1 X-ray diffraction . . . . .	15
2.1.2 Relation between the intensity of the standing wave field and the photoelectron yield . . . . .	16
2.1.3 Data analysis with DARE . . . . .	17
2.1.4 XPS analysis . . . . .	19
2.1.5 The fitting algorithm for the XPS peaks . . . . .	20
2.1.6 Conclusions . . . . .	23
2.2 Introduction to scanning tunneling microscopy and spectroscopy . . . . .	24
2.2.1 Scanning tunneling microscopy . . . . .	24
2.2.2 Scanning tunneling spectroscopy . . . . .	26
2.3 Angle-resolved photoemission spectroscopy . . . . .	29
2.4 Experimental setup . . . . .	32
<b>3 Using concepts from supramolecular chemistry for building surface structures</b>	<b>35</b>
3.1 H-bond recognition on Ag(111) . . . . .	35
3.2 Surface induced change of molecular conformations . . . . .	38
<b>4 Controlling intermolecular interactions on metal surfaces</b>	<b>43</b>
4.1 Tetraazaperopyrene (TAPP) on Cu(111) . . . . .	43
4.1.1 Aggregation at low temperatures . . . . .	44
4.1.2 Metal coordination . . . . .	45
4.1.3 C-C coupling between TAPP molecules . . . . .	50
4.1.4 Summary . . . . .	57
4.2 Preliminary studies on the formation of covalent couplings in other systems . . . . .	58
4.2.1 Tetraazapyrene (TAP) on Cu(111) . . . . .	58
4.2.2 Polymerization in two dimensions . . . . .	59

<b>5</b>	<b>A porous molecular network on Cu(111)</b>	<b>63</b>
5.1	Stability of the porous network . . . . .	64
5.1.1	Determination of the adsorption height . . . . .	64
5.1.2	The valence bands . . . . .	66
5.1.3	Discussion . . . . .	69
5.2	Band formation from coupled quantum wells . . . . .	72
5.2.1	STS: Confinement of the surface state . . . . .	72
5.2.2	ARPES: The formation of an electronic band . . . . .	73
5.2.3	A strong confinement . . . . .	76
5.2.4	Summary . . . . .	77
5.3	Comments on the lateral confinement of the surface state within pores . . . . .	77
<b>6</b>	<b>Conclusions and Outlook</b>	<b>83</b>
<b>A</b>	<b>Appendix to Chapter 3</b>	<b>85</b>
A.1	The interplay between enthalpy and entropy . . . . .	85
A.2	LEED of (3) on Ag(111) . . . . .	86
<b>B</b>	<b>Appendix to Chapter 4</b>	<b>89</b>
B.1	Analysis of the metal coordinated close-packed assembly (assembly 2) . . . . .	89
B.2	The supply of the metal coordinated structures with Cu-adatoms . . . . .	91
B.3	Open questions . . . . .	92
<b>C</b>	<b>Appendix to Chapter 5</b>	<b>95</b>
C.1	XSW: Separation of the nitrogen species . . . . .	95
C.2	ARPES studies of DPDI/Cu(111) . . . . .	96
C.3	Electronic states and bands . . . . .	97
C.4	Quantum confinement . . . . .	98
	<b>Bibliography</b>	<b>101</b>
	<b>Acknowledgements</b>	<b>113</b>
	<b>Publications</b>	<b>115</b>
	<b>Curriculum vitae</b>	<b>117</b>



# Abbreviations and molecules

## Abbreviations

ARPES	Angle-resolved photoemission spectroscopy
DOS	Density of states
EDC	Energy dispersion curves
LDOS	Local density of states
LT	Low temperature
LUMO	Lowest unoccupied molecular orbital
ML	Monolayer
NIXSW	Normal incidence X-ray standing wave
PES	Photoemission spectroscopy
QMB	Quartz crystal microbalance
QMS	Quadrupole mass spectrometer
RMS	Root mean square
RT	Room temperature
SBZ	Surface Brillouin zone
STM	Scanning Tunneling Microscopy Scanning Tunneling Microscope
STS	Scanning Tunneling Spectroscopy
UHV	Ultrahigh vacuum
UPS	Ultra-violet photoelectron spectroscopy
vdW	van der Waals
XPS	X-ray photoelectron spectroscopy
XSW	X-ray standing wave

Molecules

Abbr.	Name of molecule	Sketch
DIBOTAP	N,N',N'',N'''-diborylene-3,4,9,10-tetraaminoperylene	
DPDI	4,9-diaminoperylene-quinone-3,10-diimine	
TAP	1,3,6,8-tetraazapyrene	
TAPP	1,3,8,10-tetraazaperopyrene	
TMA	Benzene-1,3,5-tricarboxylic acid (Trimesic acid)	
<b>1</b>	1-Hexyl-6-[(anthracen-9-yl)ethynyl]uracil	
<b>2</b>	1,1'-hexyl-6,6'-[(phen-1,4-diyl)diethynyl]bisuracil	
<b>3</b>	4,4'-[(phen-1,4-diyl)diethynyl]bis(2,6-diacetylaminopyridine)	

# 1 Introduction

**Surprise and fortune** may to a large extent define scientific excitement while curiosity may provide the motivation for scientific effort. This statement also applies to the work at hand.

“New ideas, technologies and products are the happy by-products of research in good times.” [1] From this viewpoint the transfer of scientific findings to technological innovation may rather be considered as artful but important skill than mandatory necessity. *Organic* and *molecular electronics* represent a fraction of such potential technological innovation and are often related to studies of molecular adsorbates on surfaces – the subject of this thesis.

The concepts of *organic electronics* are based on those of semiconductor device fabrication in which differently doped semiconductors, metals and insulators are combined to passive (e.g. resistors and capacitors) or active (e.g. transistors) electronic components. Their assembly to logic gates that perform Boolean logic operations represent the heart of current microprocessors. In organic electronics the basic elements, especially (inorganic) semiconductors, are replaced by organic molecules [2, 3]. Potential advantages like specific tuning of the electronic properties (such as band gaps and charge carrier mobility) and the combination with flexible or transparent substrates are accompanied by a generally lower charge carrier mobility compared to (poly-)crystalline silicon [3, 4]. Currently, printed (i.e. low-cost) and flexible electronics<sup>1</sup> [6], as well as illumination [7] and display technologies [8] based on organic materials (Organic Light Emitting Diode, OLED) or organic photovoltaics [9] are considered as (potentially) emerging technologies. Also the nano.de-Report 2009 of the German Federal Ministry of Education and Research (BMBF) [10] identifies organic electronics as potential future technology of nanoelectronics.

The aforementioned report also mentions *molecular electronics* in which active electronic components or even whole logic gates would be replaced by molecules [11]. An often cited capability of this approach involves space requirements: Currently, the estimated area of a logic gate<sup>2</sup> is  $1.3 \mu\text{m}^2$  whereas the projected area in 2022 amounts to  $0.08 \mu\text{m}^2$  [13]. However, at this level of miniaturization the question arises, whether the use of electrons as information carrier and Boolean logic operations as basic elements of data-processing are still suitable [11]. The relevance of this aspect is also emphasized in the International Technology Roadmap for Semiconductors 2007 which dedicates a whole paragraph to these “alternative information processing devices” [14].

---

<sup>1</sup>It is noted that the implementation of flexible electronics is not constrained to organic electronics [5].

<sup>2</sup>In the currently used 45 nm semiconductor manufacturing process the area of a SRAM cell (containing 6 transistors) is  $0.35 \mu\text{m}^2$  [12]. The area of a logic gate (containing 4 transistors) is approximately 3.7 times larger than the SRAM cell area [13].

**Studies of molecular adsorbates** are nowadays a vital part of surface science. This includes studies on single molecules [15, 16] as well as on the formation of long-range-ordered surface assemblies [17–20]. In particular, the use of “large” molecules with flexible functional groups involves conformational issues [21–24] which may influence molecular adsorption and intermolecular interactions. In Chapter 3 an example is studied in which a thermally induced transition between two long-range ordered structures is accompanied by a conformational change of the molecular building blocks. The formation of such molecular surface networks is mainly based on reversible (“weak”) intermolecular interactions.

The Nobel Prize in Chemistry for 2007, awarded to G. Ertl, has drawn much attention to *surface chemistry* and reflects the strong relationship between the industrial need for efficient chemical processes and the scientific importance of studies on chemical processes at surfaces and interfaces [25]. The implementation of a well-defined and ultra-clean surface in ultrahigh vacuum (UHV) as a workbench which chemical reactions occur on also offers the potential to create stable surface templates [26]. Recently, the extension of “weak” intermolecular interactions to “strong” covalent bonds between molecules on surfaces in UHV has drawn much attention in surface science [27–33]. The polymerization of a perylene derivative on Cu(111) is one of these examples which is discussed in detail in Chapter 4. For this system the interplay between the metal substrate, its free adatoms and the molecules is intended to provide insight in potential processes being relevant for the formation of covalent couplings. For this purpose, detailed studies of this molecular adsorbate in dependence of the annealing temperature of the sample were performed which revealed further intermolecular interactions (van-der-Waals forces and metal coordination).

A major drawback in the creation of long-range-ordered two-dimensional surface structures based on covalent bonds is the missing self-correction that is inherent to reversible intermolecular interactions [34]. This ongoing challenge, e.g. [31, 33], is addressed in Chapter 4 as well. However, the creation of such surface structures in two dimensions offers an overlap with organic electronics, in particular if it is possible to create conjugated polymers in two dimensions [34]. This step may increase the inherently slow charge carrier mobility of organic semiconductors and includes the possibility of tuning their electronic properties [3, 34].

Ordered ad-layers in two dimensions may also involve new cooperative properties, resulting from the high periodicities of the ad-layers which are expected to significantly influence the electronic structure of either predominantly the ad-layer itself or the whole system consisting of ad-layer and substrate, e.g. [35]. The latter case is addressed in Chapter 5 in which the cooperative influence of a porous molecular network [36, 37] on the free-electron-like surface state is studied which results in the formation of a weakly dispersed electronic band.

## 2 Fundamentals

In this chapter the main experimental techniques used for the thesis at hand are introduced with a focus on X-ray standing wave (XSW) absorption. Besides an introduction to scanning tunneling microscopy (STM) and spectroscopy (STS), angle-resolved photoemission spectroscopy (ARPES) is briefly described with an emphasis on its complementarity to STS. The combination of both techniques allows for detailed studies of the electronic structure of the surface. For further techniques that are used in this work – in this case X-ray photoemission spectroscopy (XPS) and low energy electron diffraction (LEED) – it is e.g. referred to [36, 38]. In the last section of this chapter the different experimental setups are described and information on the sample preparation is given.

### 2.1 X-ray standing wave absorption

In this work X-ray standing wave (XSW) absorption was used to gain information on distances between molecular adsorbates and the surface of the underlying substrate with high accuracy (the typical error in this work is in the order of  $0.05\text{\AA}$ ). With this technique not only the distance (or height) of an adsorbate but the heights of different chemical species making up the adsorbate can be determined. However, as XSW is a laterally averaging technique a reasonable order of the adsorbate with respect to the parameters under investigation (height and possibly the lateral position) is necessary.

This section is based on the reviews by J. Zegenhagen [39] and D.P. Woodruff [40] that include beside experimental issues a detailed theoretical background. After a very brief introduction to the basic theoretical ideas this section will concentrate on how the data analysis is carried out.

The basic principle of XSW is shown in Figure 2.1. If a single crystal is irradiated with X-ray photons whose energy matches a Bragg condition the superposition of incident and reflected beam results in a standing wave field (Fig. 2.1.a). The phase difference between incident and reflected beam can be tuned by tuning the photon energy in a small range around the Bragg energy (here:  $\pm 2\text{ eV}$ ) (Fig. 2.1.c). This means that the nodes and antinodes of the standing wave field will move (arrow in Figure 2.1.a). Thus, the intensity of the standing wave field depends on both the height  $h_G$ <sup>1</sup> (of the adsorbate where the intensity is measured) and the photon energy. Therefore for each height (mod  $d_G$ )<sup>2</sup> a unique function (intensity vs. photon energy)

---

<sup>1</sup>The index  $G$ , e.g.  $G = (111)$ , specifies the Bragg planes that are used to form the standing wave field.

<sup>2</sup>The distance between neighboring Bragg planes  $d_G$  corresponds to the periodicity of the intensity of the standing wave field. Thus the functions (intensity vs. photon energy) are identical for

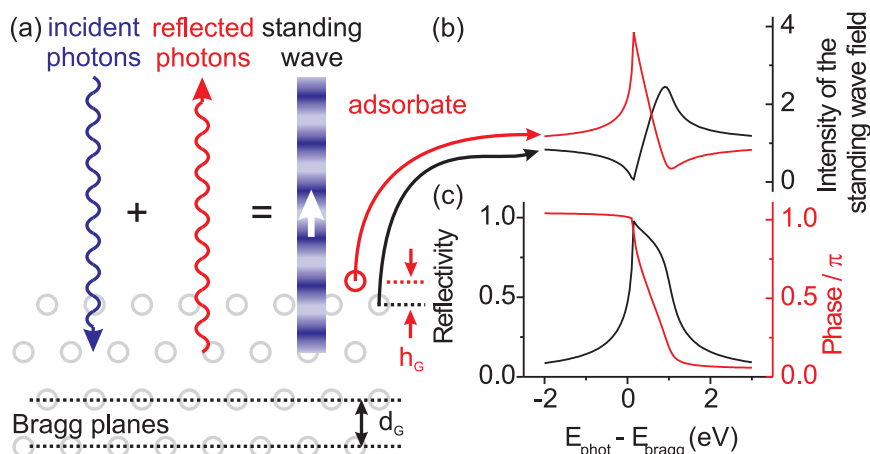


**Figure 2.1:** Basic idea of XSW. a) The superposition of incident and reflected beam creates a standing wave field at an energy that matches a Bragg condition. b) Intensity (normalized by the intensity of the incident beam) of the standing wave field vs. photon energy at two different heights. Beyond the Bragg condition the normalized intensity approximates the expected value 1. c) Reflectivity and phase difference between incident and reflected beam vs. photon energy.

is obtained as illustrated in Figure 2.1.b. The experimental goal is the determination of these functions (the intensity profiles in Fig. 2.1.b) which are used to calculate the heights of the adsorbates. These intensity profiles are determined indirectly by measuring the photoelectrons that are emitted by the adsorbate in a setup for X-ray photoemission spectroscopy (XPS). This approach makes sense because the photoelectron yield of the core-levels of an adsorbate directly depends on the intensity of the standing wave field at the adsorbate position. Moreover, this approach includes the above-mentioned possibility of determining the height  $h_G$  of each chemical species of the adsorbate.

In the following this section will focus on normal incidence XSW (NIXSW). For NIXSW the X-ray beam is perpendicular to the Bragg planes, i.e. the Bragg condition is met at a Bragg angle of close to  $90^\circ$ .<sup>3</sup> An important prerequisite for performing NIXSW measurements is the possibility to tune the photon energy to meet the Bragg condition. Thus, synchrotron radiation is necessary. By using different Bragg planes it is in principle possible to triangulate the position of the adsorbate, i.e. to determine beside the height also the lateral position with respect to the underlying substrate.

It is noted that instead of tuning the photon energy changing the angle between sample and X-ray beam basically results in the same effect of traversing the Bragg condition. In this way the first successful XSW measurements were carried out. In this case the Bragg condition is met in an off-normal setup and thus laboratory X-ray

---

all heights  $h_G + n \cdot d_G$  ( $n \in \mathbb{N}$ ) and the determined height of an adsorbate always contains the undefined offset  $n \cdot d_G$ .

<sup>3</sup>Depending on the Bragg planes that are used NIXSW does not necessarily imply that the X-ray beam is perpendicular to the surface.

sources can be used whose energy cannot be tuned. However, such an approach makes high demands on both the experimental setup (angles have to be tuned in a range significantly smaller than  $1^\circ$ ) and the quality of the crystal (small mosaicity). To a certain extent these constraints are overcome with NIXSW as the width of the curves (Fig. 2.1.b and c) exhibit a maximum at a Bragg angle of  $90^\circ$ .

### 2.1.1 X-ray diffraction

In the introduction it is already indicated that a detailed knowledge on the quantitative behavior of the standing wave field with respect to the photon energy and the height  $h_G$  is necessary to calculate the latter value. For this purpose theories on X-ray diffraction are used. A very well known approach is the *kinematical theory of (X-ray) diffraction* in which an incoming plane wave interferes with spherical waves arising from each point (atom) of the crystal under study. This interference is calculated at a distance that is large compared to the dimensions of the crystal. Including the periodicity of the crystal lattice and the information on its basis, the determination of both the Laue condition which is equivalent to the Bragg condition and the structure factor which describes the relative “intensity of the Bragg points” is possible. One drawback of this approach is the negligence of the extinction of the incoming plane wave: A spherical wave that departs from the inside of the crystal has the same weight as a wave departing from an equivalent position of its surface. Moreover, each atom “generates” only one spherical wave. Thus, multiple scattering events are neglected.

The constraints of the *kinematical theory of (X-ray) diffraction* are overcome in the theory of *dynamic (X-ray) diffraction* which allows an accurate description of the diffraction at the crystal. Within this theory the intensity of the wave field at a specific height  $h_G$  and at an energy  $E$  is:

$$I_G^{\text{WF}}(h_G, E) = 1 + R(E) + 2 \cdot \sqrt{R(E)} \cdot \cos\left(\nu(E) - 2\pi \frac{h_G}{d_G}\right) \quad (2.1)$$

- $I_G^{\text{WF}}$  Intensity of the (standing) wave field (WF) normalized by the intensity of the incident beam (cf. Fig. 2.1.b)
- $R(E)$  Reflectivity (cf. Fig. 2.1.c)
- $\nu(E)$  Phase between the incident and reflected beam (cf. Fig. 2.1.c).

The reflectivity and the phase can be extracted from the ratio of the electric fields:

$$\frac{\mathcal{E}_G(E)}{\mathcal{E}_0(E)} = \sqrt{R(E)} \cdot e^{i\nu(E)} \quad (2.2)$$

- $\mathcal{E}_G$  Electric field of the wave reflected at the Bragg planes characterized by G
- $\mathcal{E}_0$  Electric field of the incident wave.

As the reflectivity approximates 0 outside the Bragg condition (Fig. 2.1.c) the normalized intensity of the wave field approximates 1 (Equation 2.1). In other words:

Outside the Bragg condition the intensity of the wave field corresponds to the intensity of the incident wave and the standing wave field ceases to exist. If the energy dependent intensity at the position of the adsorbate is known Equation 2.1 can be used to fit this curve with the parameter  $h_G$ .

### 2.1.2 Relation between the intensity of the standing wave field and the photoelectron yield

The intensity of the standing wave field at the adsorbate position is determined indirectly by measuring the photoelectron yield for the core levels of the different chemical species making up the adsorbate. In first order the intensity of the standing wave field is assumed to be proportional to the photoelectron yield, i.e. the intensity (area) of the XPS peak. However, XPS measures the signal of every element (of the same chemical species) with the (probably varying) height  $h_{G,i}$ . The XPS intensity at a photon energy  $E$  should then be proportional to the sum of the intensities  $I_G^{\text{WF}}(h_{G,i}, E)$  at the element positions  $h_{G,i}$ :

$$I_G^{\text{XPS}}(E) \propto \sum_i I_G^{\text{WF}}(h_{G,i}, E) \quad (2.3)$$

$I_G^{\text{XPS}}(E)$	Intensity of an XPS core level peak measured at the photon energy $E$
$I_G^{\text{WF}}(h_{G,i}, E)$	Intensity of the standing wave field at the position of element $i$ (cf. Eq. 2.1).

The sum of the *cos*-terms in Equation 2.3 (cf. Equation 2.1) containing the same variable  $\nu$  but different phases  $2\pi \cdot h_{G,i}/d_G$  results in a *cos*-term with a new phase  $\bar{h}_G$  and a new amplitude  $F_G$ . The XPS signal is then proportional to:

$$I_G^{\text{XPS}}(E) \propto 1 + R(E) + 2 \cdot \sqrt{R(E)} \cdot F_G \cdot \cos(\nu(E) - 2\pi P_G) \quad (2.4)$$

$F_G$	Coherent fraction
$P_G$	Coherent position: $P_G = \bar{h}_G/d_G$ .

The coherent fraction  $F_G$  indicates the disorder<sup>4</sup> of the element that is studied. A coherent fraction of 1 indicates a perfect order, i.e. every element adsorbs at the same height whereas a decreasing coherent fraction indicates increasing disorder.

Until now a proportionality between the intensity of the standing wave field and the photoelectron yield was assumed. This approximation is valid as long as the wave length of the wave field significantly exceeds the dimensions of the atom. In the experiments described in this work the X-ray wavelength is 4.3 Å. Thus, deviations from this so called dipole approximation have to be taken into account. This becomes even more important if the electron distribution of an atom is asymmetric since the

---

<sup>4</sup>This disorder only refers to the axis perpendicular to the Bragg plane  $G$ , i.e. varying heights  $h_{G,i}$  of the element  $i$  induce disorder.



**Table 2.1:** Quadrupole parameters on Cu(111) taken from [42].

	Carbon(1s)	Nitrogen(1s)
$S_R$	1.76	1.77
$ S_I $	1.382	1.388
$\Psi$	-0.055	-0.067

reflected wave might be absorbed in a different way than the incident wave. These deviations are accounted for as quadrupole parameters  $S_R$  and  $S_I$  that are included in Equation 2.4 in the following way:

$$I_G^{\text{XPS}}(E) \propto 1 + R(E) \cdot S_R + 2 \cdot \sqrt{R(E)} \cdot |S_I| \cdot F_G \cdot \cos(\nu(E) - 2\pi P_G + \Psi) \quad (2.5)$$

$$S_I = |S_I| \cdot e^{i\Psi}$$

The parameter  $S_I$  is a complex number with absolute value  $|S_I|$  and phase  $\Psi$ . It is noted that another parametrization of these non-dipolar contributions exists which, however, is used less in literature. It was introduced by Nelson et al. [41] and consists of the two independent parameters  $q$  and  $\Delta$ . The quadrupole parameters normally depend on the experimental geometry, the element number, the photon energy and the orbital symmetry of the initial state. For the analysis presented in this thesis the quadrupole parameters (Table 2.1) were taken from [42] where they were determined for NIXSW measurements on Cu(111).

The energy dependent photoelectron intensity  $I_G^{\text{XPS}}(E)$  (Eq. 2.5) of a specific element is called *photoelectron yield curve* in the following. Each value of the photoelectron yield curve at photon energy  $E$  represents the intensity of a core-level peak (XPS-spectrum) taken with photon energy  $E$ .

### 2.1.3 Data analysis with DARE

Together with the reflectivity (Fig. 2.1) which is called *rocking curve* in the following, the photoelectron yield curve (Equation 2.5) is used to determine coherent fraction and position. For this procedure the software DARE developed by J. Zegenhagen is used. In the following the basic concept of the software is described with emphasis on several aspects which are relevant for the analysis of the experimental data presented in this work.

In a first step, DARE recalibrates the energy scale and the intensity scale of the rocking curve to determine the energy-dependent behavior of the reflectivity  $R(E)$  and the phase  $\nu(E)$ . This is done after subtracting an offset. This is reasonable as the reflectivity is supposed to approximate 0 outside the Bragg condition. Deviations of the experimental photon energy scale from the theoretically determined scale may be due to both monochromator drift and the not negligible mosaicity of the crystal.

In a second step, the information on reflectivity and phase are used to fit the photoelectron yield curve and to extract coherent fraction and phase. Because the diffraction of the crystal is already fully characterized after the first step the fit of the photoelectron yield curve is an unambiguous (non-critical) process with respect to the fit parameters: Either the fit works and coherent fraction and position are determined or the curve cannot be described by the theoretical model. Thus, the most critical step is the fit of the rocking curve. Because of this, the rest of the paragraph is dedicated to the effects of monochromator drift and mosaicity of the crystal that both influence the rocking curve.

For performing XSW measurements a photon energy just below the Bragg condition is used as initial value. After recording the relevant XPS spectra the energy is increased a bit and the recording of the XPS spectra is repeated at the new photon energy.

The experimental setup used for this work exhibited a noticeable monochromator drift. Thus, in order to reduce the monochromator drift (backlash) a photon energy lower than the initial value was chosen. By this the (real) initial value for the XSW experiment was stepwise approached from below. The residual drift should result in a deviation of the theoretical energy range from the experimental one whereas the intensity should not be affected.

In [43] real and thus imperfect crystals are considered as a conglomeration of tiny, perfect crystals (mosaic blocks) which have slightly different orientations. There, mosaicity is defined as the “width of the distribution of mis-orientation angles of all the unit cells in a crystal”. Each mosaic block matches the Bragg condition at a slightly different photon energy. In principle each mosaic block provides its own rocking curve which is shifted on the photon energy scale compared to the rocking curves of other mosaic blocks. Summing up all individual rocking curves thus leads to a broadened rocking curve. Its intensity in comparison to a rocking curve of a crystal without mosaicity is lower. Hence, for occurring mosaicity the energy range of the rocking curve determined by DARE is narrowed compared to the energy range used in the experiments. DARE can mimic mosaicity to a certain extent by artificially increasing the divergence of the photon beam which is caused by the monochromator and described through the asymmetry parameter  $b$ . This divergence can be adjusted such that the two energy ranges mentioned above agree with each other.

While monochromator drift should result in rocking curves of identical intensity but different width the experimental data within this work exhibit two different features: Rocking curves taken at different positions on the same sample differ in peak position, intensity and width (Fig. 2.2.c). However, some curves are nearly identical (Fig. 2.2.d). Thus, the dominating influence on the rocking curve results from mosaicity which is therefore taken into account in the XSW analysis of this work. However, it is important to note how the “consideration” of mosaicity affects coherent fraction and position. This is shown in Fig. 2.2.a and b. The addition of mosaicity involves an average systematic deviation of -0.1 for the coherent fraction and an increase of height of 0.01 Å for the adsorbate. Especially the latter deviation does not exceed the typical error of the coherent positions determined in this work. Hence, neither monochromator drift nor mosaicity seem to lead to significant errors in our case.

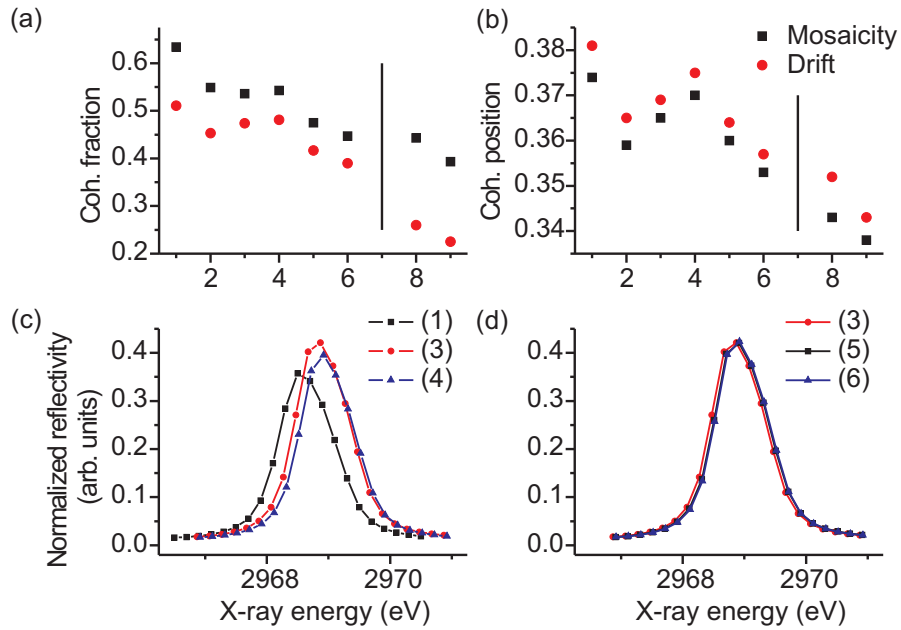


**Figure 2.2:** Coherent fraction (a), coherent position (b) and rocking curves (c, d) determined at different positions on two Cu(111) crystals (labeled from 1 to 9). The coherent position and fraction are determined for the N1s peak of the NH group of the perylene derivative DPDI forming a disordered assembly on the surface (Section 5.1). The positions 1–6 refer to one crystal whereas 8 and 9 refer to a another one.

### 2.1.4 XPS analysis

In order to determine a photoelectron yield curve, which is used as input for DARE (cf. Section 2.1.3), a set of XPS spectra taken with different photon energies has to be analyzed. The task is to calculate the peak intensity of each spectrum which can be done in two ways: The XPS spectra are either first fitted and subsequently, the area of the peak is calculated from the fit or the area is directly determined from the measured data. The advantage of the latter method is its simplicity because no assumptions are made e.g. for the shape of the peak. However, a fit may be necessary if two peaks are close to each other, i.e. if the peak positions for the same element within different chemical environments only differ by a few eV. This is the case for the experiments presented in this work. In order to have “comparable errors” the fitting strategy is always used, whether necessary or not.

Figure 2.3 compares both strategies for a set of XPS spectra of the same chemical species. The coherent positions exhibit a systematic deviation of 0.01 which corresponds to a difference in height of 0.02 Å. For the coherent fraction the choice of one strategy does not seem to induce a systematic error (Fig. 2.3). In the case of the direct determination of the peak area (filled squares in Fig. 2.3), the deviations from the average coherent position seem to be smaller compared to the deviations from the average coherent fraction. Furthermore, the coherent fractions, calculated from the direct determination of the peak area, seem to differ more strongly from the

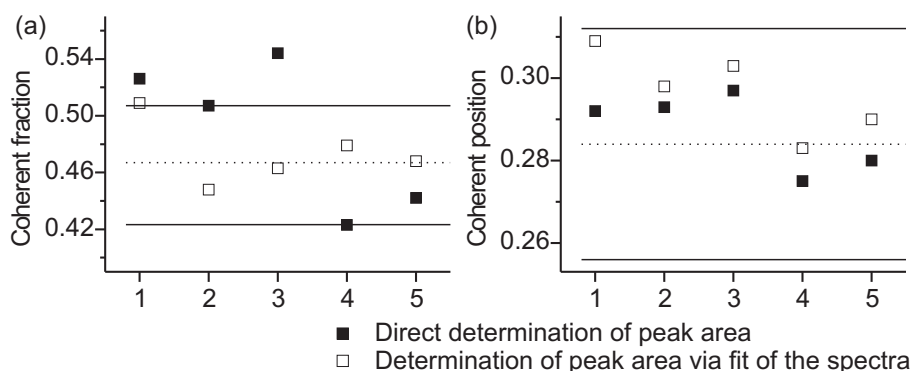


**Figure 2.3:** Coherent fraction (a) and position (b) for five different sample positions. Two strategies were used to analyze the XPS spectra at five different positions on the sample (labeled 1 to 5). For the hollow squares the XPS spectra were fitted and the area of the peak was calculated from the results of the fit whereas for the filled squares the area of the peak was determined directly. The black dotted lines show the average coherent fraction and position, respectively. The straight lines indicate the corresponding standard deviations. These statistical values were obtained by the first strategy and include besides the five positions shown here ten additional positions. Coherent fraction and position are displayed for the C1s peak of the perylene derivative DPDI adsorbed on Cu(111) in a disordered phase (Section 5.1).

average coherent fraction than those whose calculation is based on the fits of the XPS spectra. Although the statistics is not sufficient to make a rule from this observation, it can be qualitatively understood in the following way. While the coherent position is determined by the shape of the photoelectron yield curve the coherent fraction is determined by its deviation from 1. For XPS spectra with low peak intensity (low photoelectron yield) noise might significantly affect the direct determination of the peak area. In contrast, the fit with a fixed peak position and width might result in a noise reduction. Moreover these considerations show the robustness of the XSW technique with respect to the determination of the coherent position, i.e. the height of the adsorbate.

### 2.1.5 The fitting algorithm for the XPS peaks

Due to the massive data acquisition of XPS spectra<sup>5</sup> their analysis has been automatized. The corresponding script has to consider parameters like shake up, linear and/or Shirley background and the peak positions. In general, a large set of adjustable fit parameters creates significant dependencies between these parameters. In the worst case the fitting procedure becomes untrustworthy. Moreover, the fitting procedure is further complicated as beam damage sets an upper limit to the data acquisition time what results in rather noisy XPS spectra (Fig. 2.4.b).

<sup>5</sup>Each photoelectron yield curve is the result of the analysis of approximately 20 XPS curves. Two different assemblies are studied with focus on the N1s and C1s spectra.

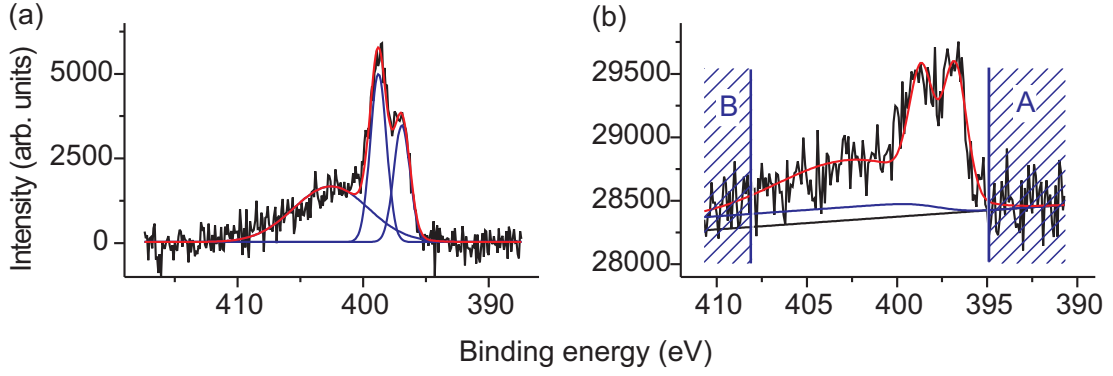


**Figure 2.4:** N1s spectra together with the corresponding fits for submonolayer coverage of DPDI on Cu(111). a) Spectrum recorded with “good” statistics after background subtraction in order to gain reliable information on peak positions and widths. b) Fit of one XPS spectrum that is part of an “XSW-set” (the analysis of the XPS spectra of one set results in one photoelectron yield curve). The effects that are considered by the fitting algorithm are exemplarily illustrated: The overall curve (red) is the sum of the fits of the two N1s peaks and the shake up, the Shirley background (blue) and the linear background (black).

Hence, the aim of an optimized script includes the reduction of the number of adjustable fit parameters. For this reason the peak shape is described by a Gauss profile and not by a perhaps more accurate Voigt profile assuming that the Gauss profile of the analyzer will dominate the peak shape. Thus, the following fit function has been used:

$$\begin{aligned}
 \text{Fit}(E) = & \underbrace{C + L \cdot E}_{\text{Linear background}} + \underbrace{B \cdot \text{shi}_{\tilde{E}, \tilde{w}}(E)}_{\text{Shirley background}} + \\
 & \underbrace{A_{SU} \cdot \exp\left\{-\frac{(E - E_{SU})^2}{2 \cdot w_{SU}^2}\right\}}_{\text{Shake Up}} + \underbrace{A_P \cdot \exp\left\{-\frac{(E - E_P)^2}{2 \cdot w_P^2}\right\}}_{\text{XPS peak}} \quad (2.6) \\
 \text{shi}_{\tilde{E}, \tilde{w}}(E) = & \int_{-\infty}^E \exp\left\{-\frac{(\mathcal{E} - \tilde{E})^2}{\tilde{w}^2}\right\} d\mathcal{E}
 \end{aligned}$$

- |                          |  |
|--------------------------|--|
| $C, L$                   | Offset and slope of the linear background                            |
| $B, A_{SU}, A_P$         | Amplitudes of the Shirley background, the shake up and the peak      |
| $\tilde{E}, E_{SU}, E_P$ | (Peak) energies of the Shirley background, the shake up and the peak |
| $\tilde{w}, w_{SU}, w_P$ | (Peak) widths of the Shirley background, the shake up and the peak.  |

- **Peak energies and widths.** XPS spectra with better statistics (Fig 2.4.a) were used to determine the positions and widths of the peaks(s) and the shake up.<sup>6</sup> Also in the case of two neighboring peaks only one shake up is assumed. The determined widths are used as constant parameters for the fit function (Eq. 2.6). The difference in energy between the peak and the shake up (and in the case of two peaks also the difference between them) are the other constant parameters. Thus, only one adjustable peak position (the reference energy) is left that determines the “lateral position” of the fit function on the energy axis.<sup>7</sup> Originally, this parameter should compensate for monochromator drift within the XPS-spectra of one “XSW-set”.<sup>8</sup> For this purpose, however, the signal-to-noise-ratio was too bad. Hence, the parameter was set constant for the XPS spectra of one “XSW-set”. By repeating the fitting algorithm and varying this parameter it was then manually adjusted. In this context it is noted that even an arbitrary change of this reference energy did not change the shape of the photoelectron yield curve significantly.
- The **Shirley background** considers secondary electrons (photoelectrons that are scattered inelastically on their way to the analyzer) [36,44]. With increasing binding energy (decreasing kinetic energy) the intensity of the (Shirley) background also increases. Assuming a proportionality between the number of secondary electrons and the intensity of the peak (that is responsible for these secondary electrons) the Shirley background can be described as [36]:

$$\text{Shirley background}(E) \propto \int_{-\infty}^E \text{Peak function}(\mathcal{E}) d\mathcal{E}. \quad (2.7)$$

This term is denoted as  $\text{shi}(E)$  in Equation 2.6. In the case of a Gauss profile this integral is proportional to the error function. A Shirley background is only considered for the main peak(s), but not for the shake up so that

$$\tilde{E} = E_P \quad \tilde{w} = w_P.$$

In order to limit the number of fit parameters only one Shirley background is also assumed in the case of two neighboring peaks ( $E_{P,1}$ ,  $w_{P,1}$ ,  $E_{P,2}$ ,  $w_{P,2}$ ) resulting from different chemical environments of one element. In this case the following parameters were used:

$$\tilde{E} = (E_{P,1} + E_{P,2})/2 \quad \tilde{w} = (w_{P,1} + w_{P,2})/2.$$

<sup>6</sup>For this purpose a photon energy is used that significantly differs from the Bragg condition (here:  $E_{\text{Bragg}} - 5$  eV). Thus, the standing wave field is not formed and each atom is irradiated with the same intensity.

<sup>7</sup>However, besides this peak position there are still other adjustable parameters, such as amplitudes of peaks and Shirley background.

<sup>8</sup>The XPS analyzer measures the kinetic energy of the photoelectrons. Thus, it is necessary to know the exact photon energy to be able to calculate the binding energy accurately. However, the photon energy is affected by monochromator drift.

- **The linear background.** If the average intensity behind the peak (area B in Fig. 2.4.b) is higher than in front of the peak (area A) the assumption of a Shirley background is reasonable. In the other case, a linear background is considered and  $C$  and  $L$  are derived by applying a linear fit to the values in area A. The reduced number of points together with the bad statistics result in significant errors, especially for  $L$ . Thus, its range is constrained. A reasonable upper limit is 0. The lower limit was arbitrarily chosen by applying the script to several XPS spectra. In this context it was observed that the Shirley background was negligible ( $B \approx 0$ ) if  $L \geq 0$ . Thus  $B$  is set to 0 in this case. In summary: Either a constant background (characterized by the parameter  $C$ ) or a combination of a linear background with  $L < 0$  and a Shirley background are subtracted.  $L$  and  $C$  are determined before applying the fit function 2.6 so that they are used as constant parameters in that fit.
- **Applying the fit function.** Due to the previously described prearrangements the “only” adjustable parameters for function 2.6 are the amplitudes of the peak(s), of the Shirley background and of the shake up. The information needed for the photoelectron yield curve are the peak amplitudes.<sup>9</sup>

### 2.1.6 Conclusions

The previous paragraph shows that the analysis of the XPS spectra is a compromise between the consideration of different effects (such as background, shake up, shape of the peaks) and the applicability of the fitting algorithm. Moreover, the results of XSW are influenced by further effects: In the previous paragraphs monochromator drift and mosaicity of the crystal are discussed. Additionally the photon beam and thus the monochromator are thought to influence the shape of the rocking curve.

As the XSW analysis is based on several steps, the accuracy of the results is not considerably improved by improving only one step while other steps are neglected. However – and this is the most astonishing result from my point of view – XSW proved to be very robust against the effects that are discussed in the previous paragraphs. Especially the coherent position<sup>10</sup> is not significantly affected by the different approaches (drift versus mosaicity, direct determination of the peak area versus fit of the peak, the fit algorithm itself). It is noted that the influence on the coherent fraction is generally higher what might have to be considered in other cases. However, in general the observations made in this section make XSW a very reliable and powerful technique.

<sup>9</sup>In principle it should be the area of the peak. However, assuming a constant width the area of a Gauss profile is proportional to its amplitude.

<sup>10</sup>The coherent position is the most important result in our case as it gives information on the height of the adsorbate.

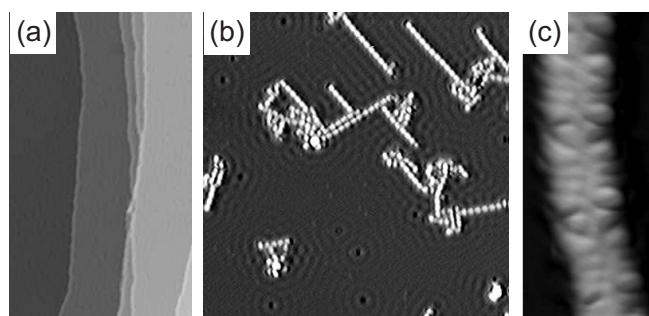


**Figure 2.5:** STM images illustrating the electronic and topographic contribution to the tunneling current. a) Steps on Cu(111) ( $76 \times 128 \text{ nm}^2$ ). b) The waves on the atomically flat terrace are an electronic effect whereas the chains are molecular adsorbates ( $50 \times 50 \text{ nm}^2$ ). c) The sensitivity to the electronic structure may become handy for the study of molecules allowing for the imaging of molecular orbitals ( $1.8 \times 4 \text{ nm}^2$ ).

## 2.2 Introduction to scanning tunneling microscopy and spectroscopy

### 2.2.1 Scanning tunneling microscopy

The invention of the scanning tunneling microscope (STM) in 1981 by Gerd Binnig and Heinrich Rohrer [45], who were rewarded the Nobel Prize in 1986, significantly influenced surface science as it allowed for the systematic study of surfaces on the (sub-)nanometer scale in real space. In an STM, a metal tip is approached very closely ( $\sim 10 \text{ \AA}$ ) to a (semi) conducting sample surface. Although a bias between tip and sample ( $|V| \leq 3 \text{ V}$ ) would not permit the overcoming of the barrier between them in classical physics quantum mechanics introduces a probability for a tunneling event between them. This probability and hence the resulting tunneling current decreases exponentially with increasing tip-sample distance. By scanning the sample line by line<sup>11</sup> and measuring the tunneling current at each point information on the height profile of the sample is gained.<sup>12</sup> Moreover, the exponentially decreasing tunneling probability ensures that only the “tip of the tip” – the tip-apex – is involved in the tunneling process, one reason for the high resolution that can be achieved by STM.

A further important aspect of STM can be motivated by considering that electrons tunnel from (electronic) states of the tip to states of the sample or vice versa. Assuming a constant density of states (DOS) of the tip<sup>13</sup>, the tunneling current basically depends on both the electronic structure of the sample and the distance between tip and sample. Thus, an STM image shows both aspects as illustrated in Fig. 2.5.

<sup>11</sup>For an accurate control of the position in the nanometer range piezoelectric elements are used.

<sup>12</sup>Normally the *constant current mode* is used in which a feedback loop ensures a constant current by controlling the position of the tip perpendicular to the sample surface (z-position). The acquired STM image then shows this z-position.

<sup>13</sup>Although the electronic structure of the tip cannot be “characterized directly” a known electronic structure of the sample can be used to “calibrate” the tip so that its DOS is featureless.



The steps in Fig. 2.5.a represent the topography of the sample whereas the waves on the atomically flat terrace (Fig. 2.5.b) are an electronic effect.<sup>14</sup> The white protrusions in Figure 2.5.b are molecular adsorbates which change topography as well as the electronic structure compared to the metal surroundings. Thus, they are not necessarily imaged as protrusions. [48] Besides, the sensitivity of the STM to the electronic structure of the sample motivates the imaging of molecular orbitals [49], exemplarily illustrated in Fig. 2.5.c.

This qualitative illustration of STM, which can mathematically be based on the calculation of the tunneling *probability* (between two “electron reservoirs”) and thus on the solution of the stationary Schrödinger equation, explains the (most important) effects very well. However, it considers the *probability* of tunneling events rather than a tunneling *rate* that can directly be interpreted as a tunneling current. In this context it is noted that in 1963 Simmons [50] derived a “formally correct” expression for a current density by considering two *metal* electrodes separated by a gap. This approach describes the topographic aspect of tunneling quite well. The STM community normally refers to Bardeen [51] who considered tunneling between separated planes. Using the time dependent Schrödinger equation, Bardeen studied the transition from a “ground state” to a state in which an electron has tunneled. For this purpose, he used an approach resembling time dependent perturbation theory. The result is formally identical to the transition probability in first order perturbation theory with a constant perturbation. Thus, Fermi’s golden rule can be applied to obtain a tunneling rate that can be interpreted as a tunneling current [52].

$$I \propto \int_0^{eV} \sum_{m,n} |M_{m,n}|^2 \delta(E - E_m) \delta(E - E_n) dE \quad (2.8)$$

$I$	Tunneling current
$m, n$	Summation indices that refer to states of the sample and the tip
$M_{m,n}$	Transition matrix element between a state of the sample and the tip.

For low temperatures the Fermi functions can be replaced by Heaviside functions. This is taken into account in Eq. 2.8. With the definition  $E_{Fermi} \equiv 0$ , tunneling events in the range  $0 \dots eV$  between tip and sample states have to be considered (integral in Eq. 2.8). The sum in the integrand considers all states of an allowed (Eigen-)energy (indices  $m, n$  in Eq. 2.8), selected by the  $\delta$ -functions.<sup>15</sup> Eq. 2.8 and its motivation which are not explicitly described in Bardeen’s original work are picked up in [54] which extensively discusses Bardeen’s approach with respect to STM including the assumptions and origins this approach is based on. Bardeen himself derived a sim-

<sup>14</sup>The electrons of the surface state which are responsible for this effect can be considered as free electrons in two dimensions (a two-dimensional plane parallel to the surface) that may scatter at defects such as steps or adsorbates. The interference of the electron waves may result in standing wave patterns that can be observed in this image [46, 47].

<sup>15</sup>It is noted that Eq. 2.8 is sometimes used without integral, e.g. [53]. The sum is then just extended to different energies. Here, the integral is included to illustrate analogies to the expression used in the next section where tunneling spectroscopy is discussed.

plified expression for the transition matrix  $M_{m,n}$  which was picked up by Tersoff and Hamann.

They [53] applied the aforementioned ideas to the geometry of the STM and calculated the tunneling current for low biases (close to the Fermi energy) and low temperatures (approximation of the Fermi-Dirac distribution by a Heaviside function).

$$I \propto V \cdot \rho_{\text{tip}}(E_F) \cdot \rho_{\text{sample}}(E_F, \vec{r}) \quad (2.9)$$

$I$	Tunneling current
$V$	Bias voltage
$\rho_{\text{tip}}(E)$	DOS of the tip (number of states per unit volume and unit energy)
$\rho_{\text{sample}}(E, \vec{r})$	DOS of the sample at the position of the tip.

It is noted that the proportionality between tunneling current and bias voltage is a result of the Taylor expansion of the Fermi functions in 1<sup>st</sup> order and thus a result of the low bias approximation. Hence, this aspect is not relevant in the following section in which “higher” bias voltages are considered.

Moreover, the tunneling current is proportional to the density of states of the sample at the Fermi energy at the position of the tip (Eq. 2.9). This demonstrates the sensitivity of the tunneling current to the electronic structure of the sample. The topographic aspect – the tunneling probability – is “hidden” in the words “at the position of the tip” as the sample wave function decays exponentially into the vacuum.

### 2.2.2 Scanning tunneling spectroscopy

Because of its sensitivity to the electronic structure of the sample, the STM is a promising tool for spectroscopic studies providing on the one hand a high spatial resolution and on the other hand an easy way to “control” the “energy of the electrons” (the tunneling voltage). In recent publications in which general (and experimental) aspects of STS are discussed, e.g. [55–57], the following equation is used as a starting point (cf. Figure 2.6).

$$I(d, V) \propto \int_0^{eV} \rho_{\text{sample}}(E) \cdot T(d, V, E) \cdot \rho_{\text{tip}}(E - eV) dE \quad (2.10)$$

$I$	Tunneling current
$V$	Tunneling voltage
$d$	Distance between tip and sample
$T(d, V, E)$	Tunneling probability, e.g. according to [56]
$\rho_{\text{tip}}(E)$	DOS of the tip
$\rho_{\text{sample}}(E)$	DOS of the sample.

In most cases, this approach is referred to as 1D WKB model. Eventually, it is the mathematical form of the descriptive introduction to STM in the first part of the previous section. Its roots can be traced back to publications by Feuchtwang et

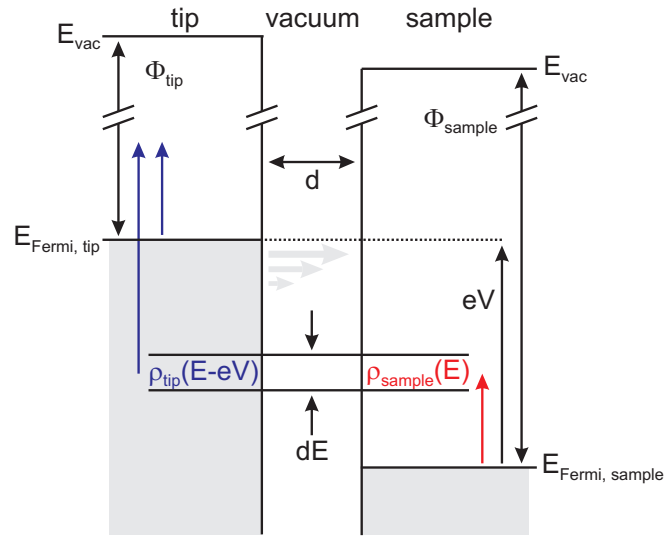


**Figure 2.6:** Motivation of Eq. 2.10. The DOS of tip  $\rho_{\text{tip}}(E)$  and sample  $\rho_{\text{sample}}(E)$  is measured with respect to the corresponding Fermi energy (red and blue lines). For completeness the work functions for tip and sample  $\Phi$  are indicated. The gray lines of different lengths indicate the influence of the tunneling probability on the tunneling current: Electrons with a higher energy exhibit a higher tunneling probability.

al. [52], Selloni et al. [58] and Lang [59] who introduced similar approaches, however using different motivations, based on either the expression of the tunneling current as a rate (Fermi's golden rule, Eq. 2.8) or the Tersoff-Hamann model itself (Eq. 2.9).

In the following, the motivation for Eq. 2.10 based on Lang [59] is briefly introduced in order to emphasize the approximative character of this equation. For his motivation, Lang did not refer to the Tersoff-Hamann model itself (Eq. 2.9), but to a discussion on the tunneling current between the sample and a tip which is replaced by a point probe in the publication of Tersoff and Hamann [53]. There, Tersoff and Hamann argued that the transition matrix element (Eq. 2.8) would be proportional to the amplitude of the wave functions of the sample  $\Psi_m(\vec{r})$  at the position of the tip  $\vec{r}$ . However, they applied this argument assuming that low bias voltages are used, whereas Lang extended this argument to “higher” bias voltages (cf. Eq. 2.8):

$$I \propto \int_0^{eV} \rho_{\text{tip}}(E - eV) \cdot \rho_{\text{sample}}(E, \vec{r}) dE. \quad (2.11)$$

For this equation, the DOS of the sample has to be known at the position of the tip (local DOS: LDOS) [53], i.e. the exponential decay of the wave functions into the vacuum has to be considered:

$$\rho_{\text{sample}}(E, \vec{r}) \equiv \sum_m |\Psi_m(\vec{r})|^2 \delta(E - E_m) \quad (2.12)$$

$\Psi_m(\vec{r})$  Wave functions of the sample at the position of the tip  $\vec{r}$ .

Lang [59] separated this problem by introducing the tunneling probability  $T(d, V, E)$ :

$$\rho_{\text{sample}}(E, \vec{r}) \equiv \rho_{\text{sample}}(E) \cdot T(d, V, E). \quad (2.13)$$

Substituting in Eq. 2.11 directly results in the desired expression (Eq. 2.10). It is noted that the terms DOS and LDOS are used according to Wagner et al. [56]

$$\begin{aligned} \rho_{\text{sample}}(E) &\equiv \text{DOS}(E) \\ \rho_{\text{sample}}(E, \vec{r}) &\equiv \rho_{\text{sample}}(E) \cdot T(d, V, E) \equiv \text{LDOS}(E). \end{aligned} \quad (2.14)$$

The voltage dependent tunneling probability considers an influence of the bias voltage on the LDOS, i.e. on the wave functions of the sample *at the position of the tip*. However, the influence of the electric field, induced by the bias voltage, on the wave functions of tip and sample is neglected. Such an influence was observed in STS, e.g. in [60, 61]: The metal surface state of Cu(111) and Ag(111) was shifted when taking spectra at different tip sample distances. This effect could be modeled by the Stark effect.

It is important to note that Eq. 2.10, which will be still further approximated, was introduced by Lang [59] as a “crude” approximation. However, in the same publication, in which he compared this approach to a more accurate description of the tunneling current, he states that this “simple model provides a good account of the qualitative features of the results of the full calculation”.

Eq. 2.10 was further approximated to the well-known proportionality between the  $dI/dV$ -signal and the sample DOS by assuming a constant DOS of the tip and by characterizing the energy- and voltage-dependence of the transmission probability as a (slowly changing) background, cf. e.g. [56]. In this context the peak positions in a  $dI/dV$ - $V$ -spectrum can be attributed to states in the DOS of the sample. However, it is important to note that the  $dI/dV$ - $V$ -spectrum does *not map* the sample DOS.

Especially at high voltages, other effects influencing the  $dI/dV$ - $V$ -spectrum may hide features of the sample DOS. Thus, different “algorithms” were introduced to recover (a better representation of) the DOS from a  $dI/dV$ - $V$ -spectrum. The most probably best known was introduced by Stroscio et al. [62], a normalization of the  $dI/dV$ -signal:  $\frac{dI/dV}{I/V}$ .<sup>16</sup> While this method may diminish the background, it may also result in peak shifts [56, 57]. In 1996 Ukraintsev [55] presented another approach for a normalization based on the tunneling probability. Moreover, he pointed out that the DOS of the tip (its unoccupied states) may dominate the  $dI/dV$ - $V$ -spectrum while probing the occupied states of the sample<sup>17</sup>: Electrons at higher energies exhibit a higher tunneling probability (cf. Fig. 2.6). While probing the occupied states of the sample the electrons with highest energy tunnel from the (Fermi energy of the) sample to the unoccupied states of the tip. Thus, they exhibit a higher influence on the tunneling current than those electrons that tunnel from the occupied states of the sample to the (Fermi energy of the) tip as the latter ones have the lowest

<sup>16</sup>A detailed discussion can be found e.g. in [56].

<sup>17</sup>This effect was already illustrated by Lang [59].

energy. This effect depends on the slope of the tunneling probability and increases with an increasing tip-sample distance [56]. Thus, it can be diminished by using small distances.<sup>18</sup> However, small tip-sample distances result in high tunneling currents which may affect the stability of  $dI/dV$ - $V$ -measurements, especially when studying (molecular) adsorbates.

In two recent contributions [56, 57] from 2007 further approaches for a DOS recovery are introduced. Besides, these publications are worth reading as both consider also experimental aspects and explicitly discuss the approaches in the context of known methods (direct interpretation, normalizations according to Stroscio and Ukraintsev). Wagner et al. [56] present an algorithm to recover peak positions from  $dI/dV$ - $V$ -spectra. Koslowski et al. [57] introduce two approaches to recover the sample DOS from the experimental results, with one being a linear combination of the  $dI/dV$ -signal and the tunneling current  $I$  and the second one being an iterative technique.<sup>19</sup> It is noted that these methods (together with their discussions and implications on exemplary DOS) are based on the approximative Eq. 2.10. However, more sophisticated considerations automatically involve more sophisticated mathematical models what limits their applicability for the interpretation of experimental results.<sup>20</sup>

The numerical derivation of the  $I$ - $V$ -spectrum is one possibility to gain the  $dI/dV$ -signal. However, the applicability of this approach is constrained by noisy results in many cases. In this work, the very common lock-in technique is used which allows for a direct determination of the  $dI/dV$ -signal. Therefore the tunneling voltage is modulated with a sinusoidal function  $V(t) = V_0 + V_1 \cdot \sin(\omega t)$ . The amplitude of the first harmonic of the tunneling current, which is detected by the lock-in, is proportional to the  $dI/dV$ -signal what can be illustrated by using a Taylor expansion:

$$I(V(t)) = I(V_0 + V_1 \cdot \sin(\omega t)) = I(V_0) + \left. \frac{dI}{dV} \right|_{V=V_0} \cdot V_1 \cdot \sin(\omega t) + \dots \quad (2.15)$$

Although a high modulation amplitude  $V_1$  would result in a better signal to noise ratio it has to be small in comparison to  $V_0$  to legitimate the Taylor expansion.

## 2.3 Angle-resolved photoemission spectroscopy

In photoemission spectroscopy (PES) photons are used to eject electrons of the sample whose kinetic energy is measured. Thus, information on the energetic position of electronic states is gained. This technique is enhanced when used in a setup for angle-resolved photoemission spectroscopy (ARPES) providing the dispersion of such states, i.e. the dependency between energy and the wave vector/the electron momentum – the function  $E(\vec{k})$ . In this work the electronic structure close to the Fermi energy

<sup>18</sup>Ukraintsev used a tip-sample distance of 11.7 Å resulting in a nearly full suppression of features in the occupied states of the sample.

<sup>19</sup>Both methods are based on a constant DOS of the tip. However, it is also discussed how to consider a tip with an energy dependent DOS.

<sup>20</sup>One example for such a simulation of STS-spectra is found in [63].

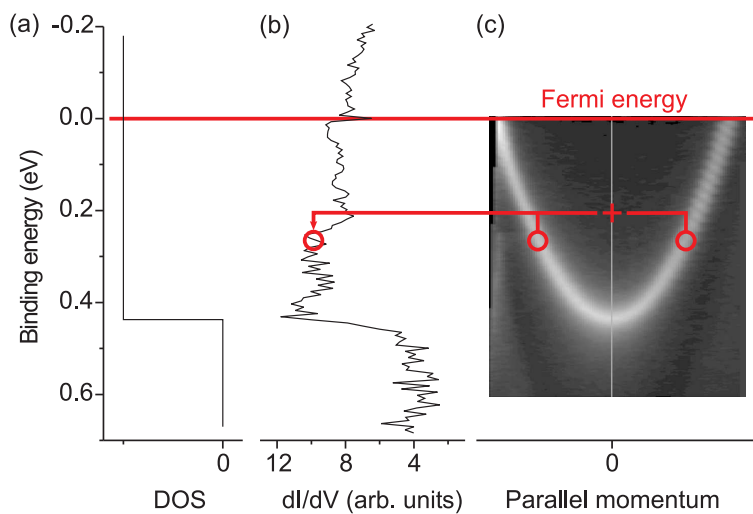


**Figure 2.7:** STS versus ARPES. a) The DOS of free electrons in two dimensions is a constant. b) The DOS of the surface state electrons, which can be considered as free electrons in two dimensions, measured with STS. c) ARPES additionally allows the discrimination of the electron momentum and is thus able to show the dispersion of the surface state, taken from [64].

( $E_{\text{Fermi}} - 7\text{ eV} \lesssim E \leq E_{\text{Fermi}}$ ) was studied. For this purpose UV light was used to excite the electrons.

ARPES is a laterally averaging technique, since a macroscopic part of the sample is irradiated. In contrast to STS, which provides a very high spatial resolution, ARPES is sensitive to the electron momentum. It is noted that in special cases this “disadvantage” of STS can be overcome, e.g. by studying standing wave patterns of surface state electrons. These electrons are scattered at defects or steps and from analysis of the occurring standing wave patterns the dispersion can be determined [65]. In general ARPES and STS allow for a complementary study of the electronic structure of surfaces, illustrated in Fig. 2.7. Surface state electrons can be considered as a free electron gas in two dimensions that is described by the dispersion

$$E_{\text{kin}} = \frac{\hbar^2}{2m} (\vec{k})^2. \quad (2.16)$$

Their DOS is a constant. Thus, the minimum energy of the surface state electrons is expected to be the onset of a Heaviside function (Fig. 2.7.a). The  $dI/dV$ - $V$ -spectrum in STS resembles this DOS (Fig. 2.7.b) as the tip virtually sums up the signals of different wave vectors. In contrast, ARPES shows the dispersion of the surface state electrons (Fig. 2.7.c, cf. Eq. 2.16).

In the following, a brief introduction to this sensitivity to the electron momentum is given. It is mainly based on an extensive and very good introduction to ARPES in [66]. In the *three step model* (Fig. 2.8.b) the photoemission process is simplified and divided into different steps:

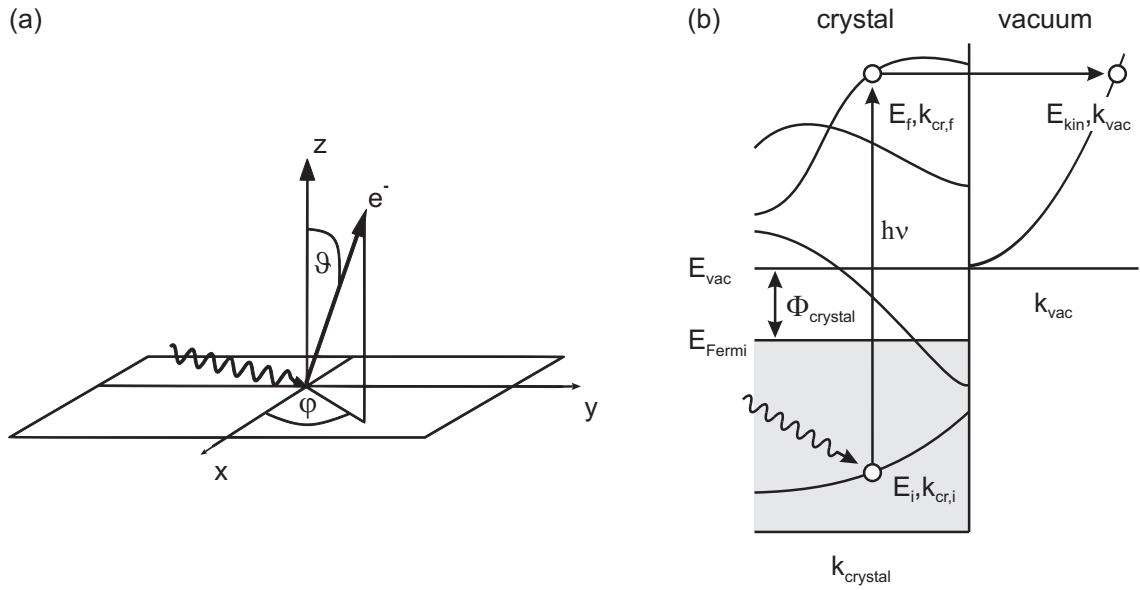


**Figure 2.8:** a) Geometry of the ARPES experiment. The position of the sample with respect to the analyzer is changed during the experiment allowing for the determination of the momentum of the photoelectrons in addition to the measurements of their kinetic energy. b) Illustration of the three step model. The kinetic energy is referred to the vacuum level  $E_{\text{Vac}}$  whereas the energies within the crystal are referred to its Fermi energy. Taken from [66].

(i) An electron with (initial) energy and momentum  $(E_i, \vec{k}_{\text{cr},i})$  is excited to a final (unoccupied) state of the crystal  $(E_f, \vec{k}_{\text{cr},f})$  by a photon of energy  $h\nu$  (Fig. 2.8). For the energies used here ( $h\nu \approx 20$  eV) the momentum of the photon can be neglected [66]. Thus conservation of momentum and energy results in

$$E_f = E_i + h\nu \quad \vec{k}_{\text{cr},f} = \vec{k}_{\text{cr},i} + \vec{g}_{\text{cr}} \quad (2.17)$$

- $E_{i/f}$  Energy of the electron inside the crystal with respect to the Fermi energy before (i) and after excitation (f) by the photon with energy  $h\nu$
- $\vec{k}_{\text{cr},i/f}$  Momentum of the electron inside the crystal before (i) and after excitation (f)
- $\vec{g}_{\text{cr}}$  Reciprocal vector of the crystal.

(ii) In the second step the electron propagates to the surface. The demand for conservation of electron energy and momentum in the previous step forbids now any scattering processes with the system.

(iii) The third step describes the transition to vacuum for which the conservation of energy is valid if inelastic processes are still ruled out. In this case the conservation of electron momentum only applies to the momentum parallel to the surface:

$$E_{\text{kin}} = h\nu - (E_i + \Phi_{\text{crystal}}) \quad \vec{k}_{\text{vac},\parallel} = \vec{k}_{\text{cr},i,\parallel} + \vec{g}_{\parallel} \quad (2.18)$$

$E_{\text{kin}}$	Kinetic energy of the excited electron in the vacuum with respect to the vacuum level $E_{\text{vac}}$
$\Phi_{\text{crystal}}$	Work function of the crystal
$\vec{k}_{\text{vac}}$	Corresponding momentum of the electron in vacuum
$\vec{g}_{\parallel}$	Reciprocal vector parallel to the surface.

The vector  $\vec{g}_{\parallel}$  is usually a reciprocal vector of the crystal parallel to the surface. Moreover, the electronic structure of the crystal might be influenced by a periodic structure on its surface, e.g. a reconstructed surface or a periodic (self-assembled) ad-layer. In this case  $\vec{g}_{\parallel}$  can also be a reciprocal vector of the unit cell of the periodic surface structure. This effect will become relevant in Chapter 5. As the unit cell of such an overlayer is usually larger than the unit cell of the crystal surface periodicities in the dispersion of electronic states are then induced “first” by the (reciprocal vectors of the) overlayer.

The position of the crystal with respect to the manipulator is determined by the emission angles  $\vartheta$  and  $\varphi$  (Fig. 2.8.a). As the electrons in vacuum obey the well known parabolic dispersion (Eq. 2.16) their momentum is determined by

$$\begin{pmatrix} k_{\text{vac},x} \\ k_{\text{vac},y} \end{pmatrix} = \sqrt{\frac{2m \cdot E_{\text{kin}}}{\hbar^2}} \cdot \sin \vartheta \cdot \begin{pmatrix} \cos \varphi \\ \sin \varphi \end{pmatrix}. \quad (2.19)$$

## 2.4 Experimental setup

The experiments were performed in a UHV (Ultrahigh Vacuum) system consisting of different chambers for sample preparation and characterization, at a base pressure of  $10^{-10}$  mbar. The single crystals were prepared by subsequent cycles of sputtering with Ar<sup>+</sup> ions and annealing at approximately 500°C. The molecules were deposited onto the metal surfaces from a glass crucible that was heated inside a commercial evaporator (Kentax UHV equipment). Normally, the rate was controlled by a quartz crystal microbalance (QMB). In some cases, especially for light molecules whose sublimation could not be controlled properly by the temperature of the crucible, the QMB was not able to detect the molecules. Instead a quadrupole mass spectrometer (QMS) from Pfeiffer (Prisma, analyzer: QMA200, electronics: QME200) which can detect masses with up to 300 u (atomic mass units) was used to detect the sublimed molecules which the preparation chamber was exposed to. The thickness could be controlled by tuning partial pressure and exposure time.

In the facilities in Basel two UHV-STM can be used, a homebuilt machine working at room temperature and a commercial low temperature STM (LT-STM from Omicron NanoTechnology GmbH) which is operated both at 77 K and 4 K. The LT-STM is



either equipped with wire cut PtIr tips or etched tungsten tips. For the homebuilt STM the bias voltage is applied to the sample whereas for the LT-STM it is applied to the tip. In order to facilitate comparisons to literature and other techniques like ARPES, the bias voltages given at the thesis at hand – concerning both STM images and spectra – refer to a grounded tip. For both systems the Nanonis SPM control system (Specs GmbH) was used. The software WSxM [67] was used for data processing of the STM images.

The Nanonis SPM control system provides an internal lock-in amplifier which was used for STS. As the cut-off frequency of the pre-amplifier of the LT-STM is 800 Hz the bias voltage was typically modulated with frequencies around 500 Hz and voltages of approximately 8 mV (rms)<sup>21</sup>. For the acquisition of STS spectra, STM tips were initially “calibrated” by reproduction of the well-known spectrum of the surface state for Cu(111) and Ag(111).

The preparation chamber of the LT-STM provides the possibility to deposit molecules onto a cooled or heated substrate. For the work at hand substrate temperatures between 150 K and 700 K were used during either deposition of molecules or annealing of the sample. Without significantly influencing the substrate temperature the sample can be transferred into the STM. The STM working at either 77 K or 4 K is thought to immobilize the molecules on the surface. Thus, temperature induced changes could be investigated. For this the sample was studied before and after annealing. In this context “annealing at a temperature  $T_{\text{final}}$ ” means that the sample was placed on the manipulator (the station used for preparation) at a temperature  $T_{\text{initial}} \ll T_{\text{final}}$  and then slowly heated to  $T_{\text{final}}$ . The time for this process varied between 15 min and 45 min.

For the LEED measurements the sample was held at room temperature. The sample was slightly tilted with respect to normal incidence to provide a better visibility of the diffraction spots of first order that would otherwise interfere with the electron gun. The software LEEDpat 2.1 [68] was used to simulate the LEED patterns.

ARPES spectra were acquired at RT (unless otherwise stated) at the COPHEE end-station located at the Swiss Light Source (SLS) using a commercial monochromatized He-lamp source. The energy (angular) resolution was 90 meV (0.5°) at 21.22 eV and the spot size was 6 mm. Thus, the sample was completely illuminated during data acquisition. Further ARPES studies were carried out at RT as well as 7 K at the CASSIOPEE end-station located at SOLEIL using synchrotron radiation. For these measurements a commercial analyzer (VG Scienta R4000) was used. The spot size was approximately 100  $\mu\text{m}$  x 50  $\mu\text{m}$  (vertical x horizontal size). In the latter case beam damage had to be accounted for during the study of molecular adsorbates as a degradation of the surface state was observed within one minute of illumination.

XSW and XPS measurements were performed at the beamline ID32 at the European Synchrotron Radiation Facility (ESRF) in Grenoble using synchrotron radiation tuned at an energy of approximately 2.97 keV in order to create a standing wave field on Cu(111). For both XSW and XPS measurements the surface, the (111) plane, was rotated by approximately 90° with respect to the incident X-ray beam. Further XPS

<sup>21</sup>Root mean square:  $\hat{U}/\sqrt{2}$ .  $\hat{U}$ : (Zero-to-)peak amplitude of modulation voltage.

measurements were performed at the Paul Scherrer Institute with a SPECS Phoibos 150 hemispherical electron energy analyzer using an Al-K $_{\alpha}$  X-ray source. For all measurements time-dependent studies of the N1s peak indicated if and especially after which exposure time the peaks were affected by the beam. Thus, a reasonable time frame was chosen to reduce the influence of beam damage on the spectra.

# 3 Using concepts from supramolecular chemistry for building surface structures

To date, concepts of supramolecular chemistry [69] have been successfully applied to surfaces, e.g. [20, 70]. In order to study such supramolecular surface structures, the STM, imaging real space with high resolution, has proved to be a convenient tool. In section 3.1 a further example that adds to this field and involves interactions between three molecular adsorbates is described. However, the transition from solution to surfaces involves, besides the constraint to two dimensions, molecule substrate interactions. Both aspects may lead to experimental results that are not expected from wet chemistry. One example for such an unexpected result is a conformational change of a molecule. This is described in section 3.2. The experimental work presented here was done in collaboration with the group of Prof. Prato and Prof. Bonifazi at the University of Trieste.

## 3.1 H-bond recognition on Ag(111)

The results discussed in this section are published in [71].

The formation of supramolecular structures via self-assembly of molecular building blocks is based on molecular recognition, which takes advantage of spontaneous and reversible non-covalent interactions, e.g. hydrogen bonding (H-bonds). In [20] molecular recognition is characterized as selective association of complementary functional molecular groups. The complementary functional groups studied in this section can undergo triple H-bonding between a uracil (acceptor-donor-acceptor functionality for H-bonding) end group on the one hand and 2,6-di(acylamino)pyridyl (donor-acceptor-donor) on the other hand [72]. With these functional groups as end groups two molecular linkers (**2** and **3** in Fig. 3.1.c and d) and a molecule that is thought to stop the formation of chains by the linkers (**1** in Fig. 3.1.b) were synthesized in the group of Prof. Prato and Prof. Bonifazi.<sup>1</sup> This concept allows to study H-bond recognition by combining either both linkers (**2** and **3**) or **1** with **3**. Moreover, the combination of all molecules may allow to study the competition between **1** and **2** when interacting with **3**.

Subsequent deposition of both molecular linkers on Ag(111) resulted in the formation of extended linear bi-molecular wires, where the two modules alternate within the

---

<sup>1</sup>Details on the synthesis are found in [71] and its supporting information.

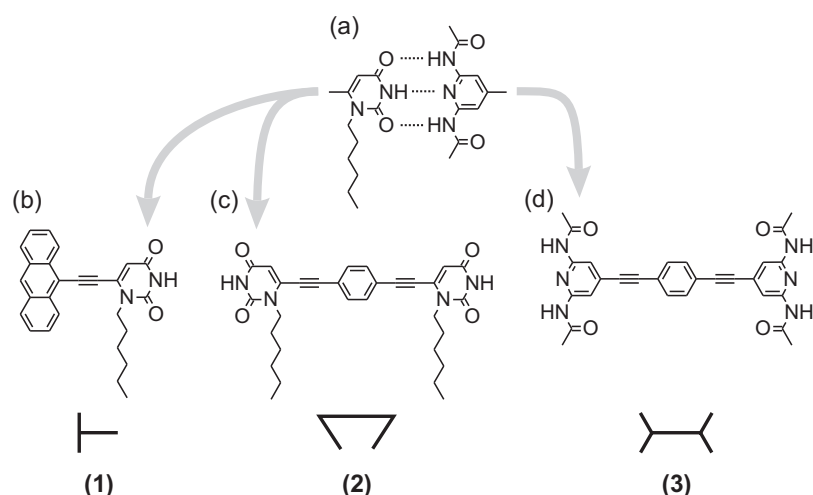


**Figure 3.1:** a) The H-bond motif [72] that is used in this work. b) Structure of 1-Hexyl-6-[(anthracen-9-yl)ethynyl]uracil (**1**). c) Structure of 1,1'-hexyl-6,6'-[(phen-1,4-diyl)diethynyl]bisuracil (**2**). d) Structure of 4,4'-[(phen-1,4-diyl)diethynyl]bis(2,6-diacetylaminopyridine) (**3**). The symbols shown below the molecular structures are used to highlight the different molecules in the STM-images to facilitate their identification.

linear assembly (Figure 3.2). As both modules are symmetric and bear complementary recognition groups (ADA and DAD for **1** and **2**, respectively), the development of the wires confirms the formation of the expected intermolecular triple H-bonds. In Figure 3.2 the two different molecules are highlighted by the symbols introduced in Figure 3.1.

The large unit cell ( $37 \text{ \AA} \pm 4 \text{ \AA} \times 24 \text{ \AA} \pm 2 \text{ \AA}$ , included angle:  $58^\circ \pm 4^\circ$ ) measured for this arrangement derives from the fact that the distance between the bimolecular wires is alternating (marked by a, b, and c in Figure 3.2.b). For the formation of a densely packed arrangement shorter inter-wire distances should be preferred. However, as **2** has two lateral hexyl chains, densely packed arrangements are limited by the space requirements of these chains. **2** adopts a cis configuration in which the hexyl chains point towards the neighboring row exhibiting the larger distance (e.g., see hexyl chains of row c pointing towards b or vice versa). However, one hexyl chain may point towards the other neighboring row, exhibiting the smaller distance, i.e. it then points towards the space between both end groups of **3**. So **2** may exhibit a trans-configuration which is rarely observed on the surface (white dotted circle, Figure 3.2.b). These observations indicate that both molecular linkers pack as dense as possible.

As the orientation between two adjacent **3** of neighboring rows flips irregularly<sup>2</sup> (indicated by blue and green lines in Fig. 3.2.b), the assembly divides into two mirror domains denoted as A and B which are described by identical unit cells that are mirrored along an axis parallel to the chains. The irregular width of both regions can be observed in larger images (data not shown here).

<sup>2</sup>It flips irregularly in space, not in time. The observed patterns are stable at 77 K.

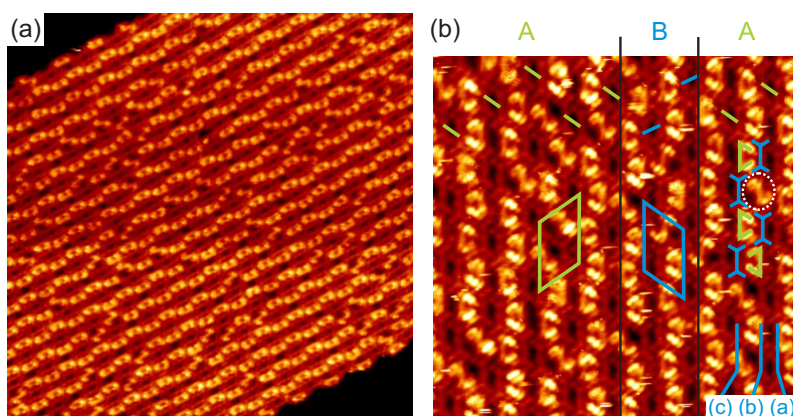


**Figure 3.2:** STM images for submonolayer coverage of both molecular linkers after annealing at 120°C. During the deposition the Ag(111) crystal was held at room temperature. a) 42 x 42 nm<sup>2</sup>, -1.3 V/12 pA. b) 17.5 x 17.5 nm<sup>2</sup>, -1.7 V/20 pA. The assembly divides into two mirror domains denoted as A and B.

The uracil-bearing molecules **1** and **2** do not assemble in an ordered mixed layer but instead disordered phases consisting of only **1** as well as mixed but disordered assemblies of **1** and **2** were observed. The latter is shown in Figure 3.3.c. The molecules were deposited consecutively while the sample was held at approximately 100°C.

Sequential sublimation of **1** and both molecular linkers **2** and **3** on Ag(111) resulted in assemblies shown in Figure 3.3.a-b. In contrast to the principally endless wire-like assemblies in Figure 3.2 the wires are terminated with **1**. Besides the long oligomers, short linear trimeric and pentameric miniatures have also been observed by STM as displayed in Figure 3.3.b.

Assemblies between **3** and **2** rely on the same H-bond motif as those between **3** and **1**; consequently **2** and **1** are expected to equally compete for binding to **3**. However, the aggregation of **1** in small disordered islands (Fig. 3.3.a and inset) despite the possible incorporation into chains (whose length would be shortened) indicates a preferred interaction between **2** and **3**. Especially in the case of weak intermolecular interactions like H-bonds the formation of ordered structures heavily relies on the interplay of enthalpy ( $H$ ) and entropy ( $S$ ). In order to minimize the free energy ( $\Delta G = \Delta H - T\Delta S$ ,  $T$ : temperature) the decrease of enthalpy has to compensate for the decrease of entropy. During the self-assembly process the formation of intermolecular interactions lowers enthalpy whereas the consequent immobilization of translational and conformational freedoms of the molecules lowers entropy [73]. This aspect is discussed in detail in the thesis of Nikolai Wintjes [74] and could be applied successfully to molecular self-assembly on surfaces in UHV. In the case at hand, **2** exhibiting two uracil units is favored in comparison to **1** as the latter one bears only one uracil unit capable of establishing energetically favored H-bonds (cf. Appendix A.1).

In this context the formation of ordered structures between both linkers is expected to occur earlier than the aggregation of **1** (to **3** or in separated clusters) during the cooling procedure from RT (deposition) to 77 K (STM). In other words: As the

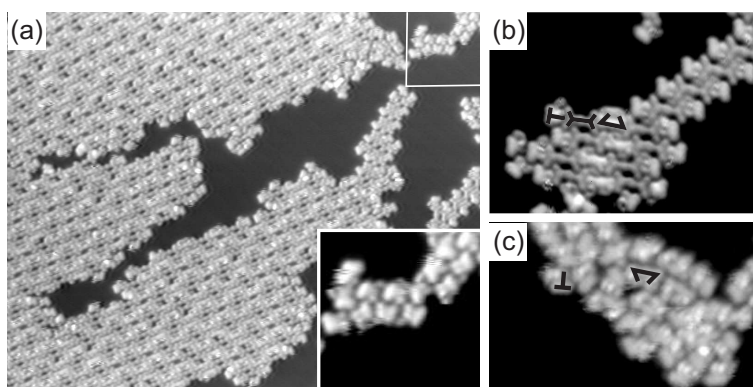


**Figure 3.3:** a) The combination of **1** and both molecular linkers (**2** and **3**) leads to chains that are terminated by **1** ( $50 \times 40 \text{ nm}^2$ ,  $-1.7 \text{ V}/20 \text{ pA}$ ). **1**, **2** and **3** were deposited in this sequence while the substrate was held at room temperature. The inset shows the upper right part (highlighted by a rectangle) in detail ( $7.7 \times 7.7 \text{ nm}^2$ ,  $-1.7 \text{ V}/20 \text{ pA}$ ). b) The interaction between the three molecules in detail after annealing at  $110^\circ\text{C}$  ( $14 \times 10 \text{ nm}^2$ ,  $-1.7 \text{ V}/20 \text{ pA}$ ). c) STM image for submonolayer of **2** and **1**. Both molecules were deposited while the sample was held at  $100^\circ\text{C}$  ( $13 \times 8 \text{ nm}^2$ ,  $-2.4 \text{ V}/13 \text{ pA}$ ).

temperature influences the term  $T \cdot \Delta S$  the linkers **2** and **3** are expected to compensate for the loss of entropy at higher temperatures when forming chains (compared to **1** when terminating the growth of the chains). Of course the order of deposition might influence this effect: If **1** was deposited after the linkers it would have to break open existing chains. In our case the sequence of deposition was **1**, **2** and **3**. Thus **1** and **2** which do not form ordered mixed patterns (Fig. 3.3.c) should equally compete for **3**. Moreover, small aggregates of **1** could still be observed after annealing at  $110^\circ\text{C}$  whereas aggregates of **2** were observed neither after deposition nor after annealing.

## 3.2 Surface induced change of molecular conformations

The results discussed in this section are published in [75].

Tailor-made molecules engineered for the creation of supramolecular structures via molecular self-assembly may feature conformational degrees of freedom, which allow for the tuning of their preprogrammed intermolecular interactions. With the invention of the STM the conformational flexibility of adsorbed organic molecules, e.g. [21–24], on surfaces could be addressed directly. In this section the formation of an H-bonded porous network by **3** (Fig. 3.1.d) is reported that, upon thermally-induced trans-cis inversion of the conformation of the amide groups ( $\text{CH}_3(\text{CO})\text{NH}-$ ), evolves into a close-packed rhombic pattern. This conformational change is not expected from wet chemistry.

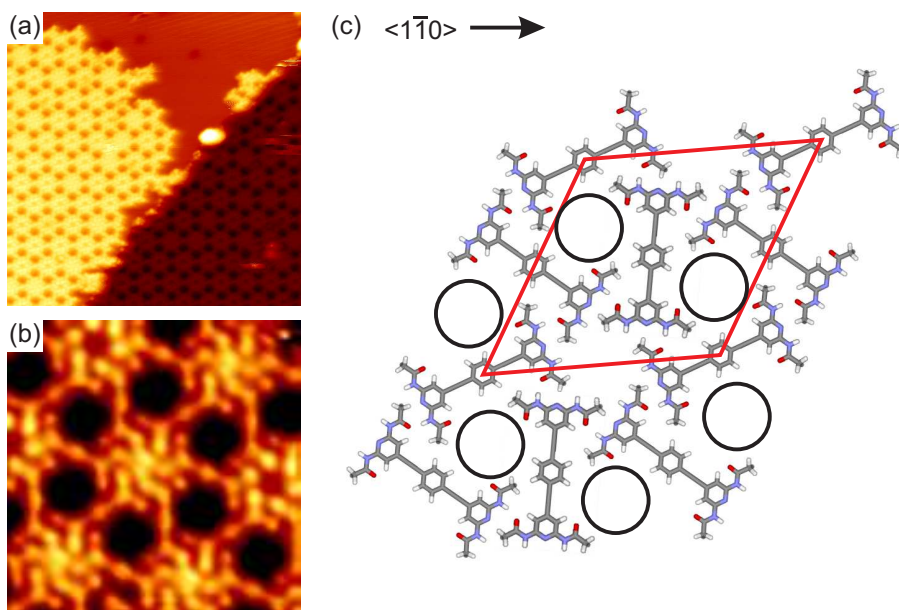


**Figure 3.4:** STM images recorded at 77 K of **3** on Ag(111) showing the porous network. a)  $34 \times 34 \text{ nm}^2$ ,  $-1.7 \text{ V}/20 \text{ pA}$ . b)  $7 \times 7 \text{ nm}^2$ ,  $-1.7 \text{ V}/20 \text{ pA}$ . c) Proposed model. The red rhombus indicates the unit cell, the black circles highlight the pores, and the arrow the high symmetry direction of Ag(111).

In a first step, the self-assembly of **3** on Ag(111) was investigated for coverages  $< 1$  monolayer. For samples prepared at room temperature, the molecules arrange in a porous hexagonal network (Fig. 3.4). In addition, low-energy electron diffraction (LEED) measurements were performed to determine the size of the unit cell with respect to the underlying Ag(111) substrate (Appendix A.2). A commensurate superstructure has been found with the molecules arranged in a rhombic unit cell with dimensions of  $30.4 \times 30.4 \text{ \AA}^2$  and an angle of  $60^\circ$ . In the proposed structure (Fig. 3.4.c), for each molecule the four amide groups are in trans conformation (i.e., DAD). Each 2,6-di(acetylamino)pyridine residue interacts via two weak H-bonds with two neighboring moieties, which results in the formation of chiral hexameric units (Fig. 3.4, see also Fig. A.4.c and d on page 88). Consequently, each chiral pore is surrounded by three molecules exhibiting an angle of  $60^\circ$  relative to each other (Fig. 3.4.c), and is internally decorated by the 1,4-disubstituted phenyl spacers and the carbonyl groups.

Remarkably, after annealing the sample at  $150^\circ\text{C}$ , the hexagonal network is transformed into the close-packed 2D rhombic pattern shown in Figure 3.5.a and b. Notably, the intensity corresponding to the two acetyl ( $\text{COCH}_3$ -) units of the terminal 2,6-di(acetylamino)pyridine groups varies: one acetyl unit appears always brighter than the other one (white arrows in Fig. 3.5.a), indicating a conformational difference between the two acetyl groups. Both STM and LEED measurements support the arrangement of **3** in a commensurate superstructure with dimensions of  $20.2 \times 10.0 \text{ \AA}^2$  and an angle of  $68.2^\circ$  (Appendix A.2). In the proposed model, each molecule interacts with the neighboring modules along the long axis of the unit cell in a head-to-head

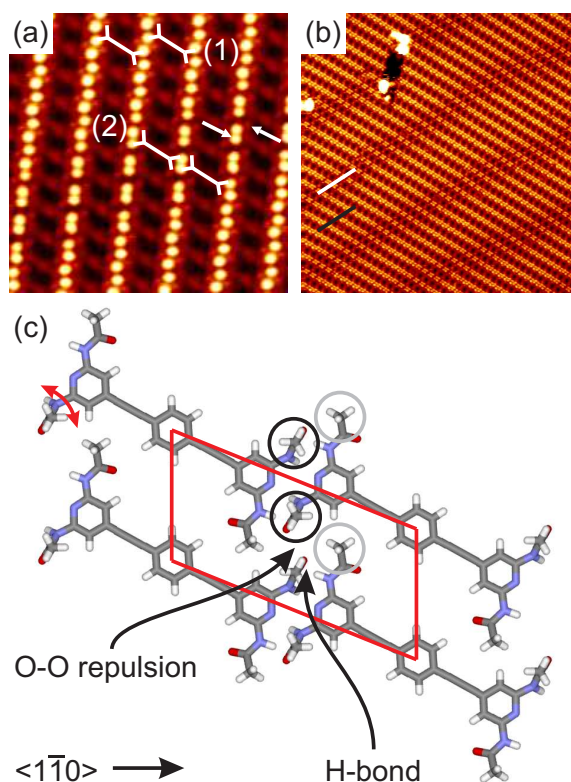


**Figure 3.5:** STM images recorded at 77 K of **3** on Ag(111) after thermal annealing at 150°C. a) 10 x 10 nm<sup>2</sup>, -2 V/12 pA. The white arrows highlight the acetyl groups (COCH<sub>3</sub>-). b) 39 x 39 nm<sup>2</sup>, -1.5 V/12 pA. The black and white bars represent areas with optimized O-O distance and H-bond length, respectively. c) Proposed model for the close-packed assembly with the high symmetry direction of Ag(111).

fashion over their terminal 2,6-di(acetylamino)pyridine groups. A simplified model of the proposed intermolecular interaction (Fig. 3.6) shows that **3** with one amidic unit in cis conformation would allow for the formation of four H-bonds between two molecules. Thus, the intermolecular interactions are enhanced with respect to **3** with both amidic units in trans conformation.

Figure 3.6 illustrates the basic idea of the proposed intermolecular interactions of **3** in the close-packed assembly. However, it only shows the molecular arrangement along the long axis of the unit cell of the close-packed assembly. If this arrangement was extended into the direction along the short axis of the unit cell the acetyl groups of neighboring rows would touch each other. Thus, the amide units are thought to display some flexibility in order to control the delicate balance between attractive (H-bonds) and repulsive (steric demands) interactions (Fig. 3.5.c). Depending on which interaction is better optimized, the conformation of the amidic group is slightly distorted and thus, the lateral position of the methyl group (CH<sub>3</sub>-) is affected (indicated by sketches (1) and (2) in Fig. 3.5.a). In other words: if the NH<sup>⋯</sup>O H-bond lengths are optimized, the O-O repulsion between neighboring COMe groups is increased and vice



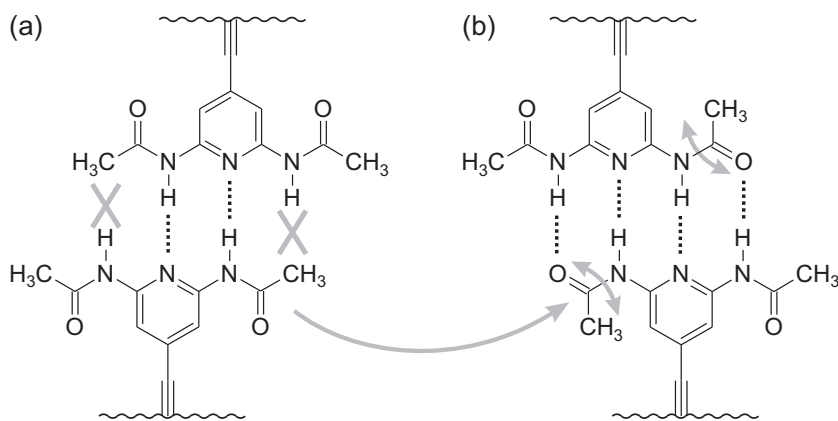


**Figure 3.6:** Model of the intermolecular interactions which **3** can undergo after annealing. a) The *trans* conformation is the expected and also observed conformation in solution [75]. This configuration allows for two H-bonds between two molecules. b) The intermolecular interactions are significantly enhanced if one of the two amide groups is in *cis* conformation. Now, the two molecules can form four H-bonds.

versa (black arrows in Fig. 3.5.c). It follows that the methyl group of the amidic unit in *cis* conformation has to be lifted from the surface. This explains the differences in brightness observed in the STM images (white arrows in Fig. 3.5.a): the methyl groups of the amidic units in *cis* conformation (indicated as black circles in Fig. 3.5.c) appear brighter than the methyl groups of the amidic units in *trans* conformation (indicated as gray circles in Fig. 3.5.c).

As both molecular surface structures are commensurate to the substrate, the molecule-substrate interaction is expected to be of significant importance for the formation of both structures. This indicates on the one hand that the surface structures are not only a result of restricting molecular movements to two dimensions. On the other hand, the commensurability indicates an adaptation of the molecular unit cell to the substrate lattice. Hence, the varying lateral positions of the methyl group observed for the close-packed assembly (Fig. 3.5.c) are considered to be influenced by the substrate as well as by the balance between H-bonds and steric demands of the molecules discussed in the preceding paragraph.

In summary, by choosing the recognition moieties appropriately, it is possible to thermally induce a phase transition for a 2D porous assembly (from a porous to a close-packed assembly). In particular, this *thermally induced* transition between both surface structures suggests that the formation of the porous network is kinetically controlled whereas the close-packed assembly represents the thermodynamically stable phase. Moreover, the formation of quadrupole H-bonds between 2,6-di(acetylamino)pyridine moieties in the close-packed assembly could be induced by exploiting the conformational *trans-cis* inversion of amide functional groups which is not observed in solution.



# 4 Controlling intermolecular interactions on metal surfaces

In this chapter the focus is changed from the *intramolecular* level, on which conformational effects were observed, to the *intermolecular* level, in particular to intermolecular interactions. The work presented here was done in close collaboration with the inorganic chemistry group of Prof. Gade at the University of Heidelberg. Moreover, the theoretical studies that are addressed in the following were carried out in the group of Prof. Persson at the University of Liverpool.

## 4.1 Tetraazaperopyrene (TAPP) on Cu(111)

The results discussed in this section are published in [29] or will be published [76].

To a very large extent this chapter deals with the perylene derivative 1,3,8,10-Tetraazaperopyrene (TAPP) (Fig. 4.1) that was synthesized in the group of Prof. Gade [77]. Its compact structure without flexible functional groups and its anticipated flat adsorption on the surface makes TAPP an ideal candidate for STM studies. Despite its at first glance simple structure, TAPP proves to reveal a versatile “surface chemistry”: Besides its four N-atoms that either may act as H-bond acceptors or coordinate to metal atoms, the CH bridge between the N-atoms offers the potential of tautomerization to an N-heterocyclic carbene isomer or may undergo metal-induced C-H activation at elevated temperatures.

On Cu(111) different substrate temperatures induce changes of the surface-assemblies of TAPP which also involve changes of intermolecular interactions. In order to study this behavior in detail TAPP was deposited on Cu(111) while the substrate was held at different temperatures. Alternatively, depositions at low substrate temperatures were followed by sample annealing. The temperatures ranged from  $-110^{\circ}\text{C}$  to  $280^{\circ}\text{C}$ . The experimental results are discussed in the following sections, which in particular address the role of Cu-adatoms for the “surface chemistry” of TAPP.

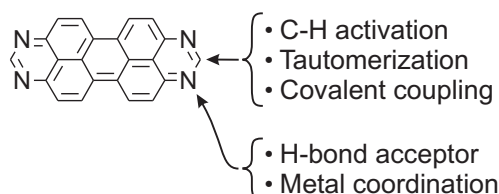


**Figure 4.1:** 1,3,8,10-Tetraazaperopyrene (TAPP). Taken from [76].

### 4.1.1 Aggregation at low temperatures

Upon deposition of TAPP at a substrate temperature of  $-110^{\circ}\text{C}$ , the formation of aggregates (“clusters”) is observed (Fig. 4.2.a) indicating an attractive intermolecular interaction. After deposition of TAPP at a substrate temperature of  $-90^{\circ}\text{C}$  first patches of an ordered close-packed assembly could be observed (Fig. 4.2.c) whose structure is showed in detail in Fig. 4.2.e. The unit cell was determined by STM to  $(17 \pm 1.7) \times (12 \pm 1.2) \text{ \AA}^2$  with an angle of  $(84 \pm 4)^{\circ}$ . According to the corresponding tentative model (Fig. 4.2.b) the molecules interact via weak vdW-forces forming an assembly that is related to the crystal structure of TAPP [76]. This similarity between the crystal structure of a molecule and its assembly on the surface was also found for the perylene derivative perylenetetracarboxyanhydride PTCDA [78].

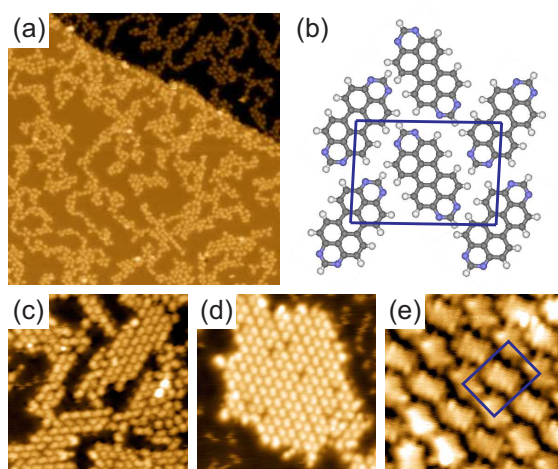


**Figure 4.2:** STM images of TAPP deposited on Cu(111). a) Deposition at a substrate temperature of  $-110^{\circ}\text{C}$  ( $66 \times 66 \text{ nm}^2$ ,  $-1.5 \text{ V}/12 \text{ pA}$ ). c) First ordered patches of a close-packed assembly after depositing at a substrate temperature of  $-90^{\circ}\text{C}$  ( $18 \times 18 \text{ nm}^2$ ,  $-0.7 \text{ V}/20 \text{ pA}$ ). d) Formation of larger islands after annealing at  $-45^{\circ}\text{C}$  ( $17 \times 17 \text{ nm}^2$ ,  $-1.5 \text{ V}/20 \text{ pA}$ ) e) The close-packed assembly in detail ( $5 \times 5 \text{ nm}^2$ ,  $-0.8 \text{ V}/90 \text{ pA}$ ) after annealing at  $40^{\circ}\text{C}$ . The unit cell is superimposed and the corresponding tentative model is shown in (b).

One reason for the formation of patches instead of large homogeneous islands may be a possible lattice mismatch between the molecular ad-layer and the substrate. This is supported by the rather weak intermolecular interactions (vdW) which have to compete with the interaction between molecule and substrate. As higher annealing temperatures result in the formation of larger vdW-islands a second reason might be the annealing temperature which is perhaps too low to induce the rearrangement of disordered clusters. A systematic investigation of this aspect was precluded by the emergence of new types of surface assemblies at higher temperatures which compete with (and finally supersede) the weakly interacting vdW structures. This transformation into ordered molecular surface networks based on stronger intermolecular interactions will be discussed in the following section.

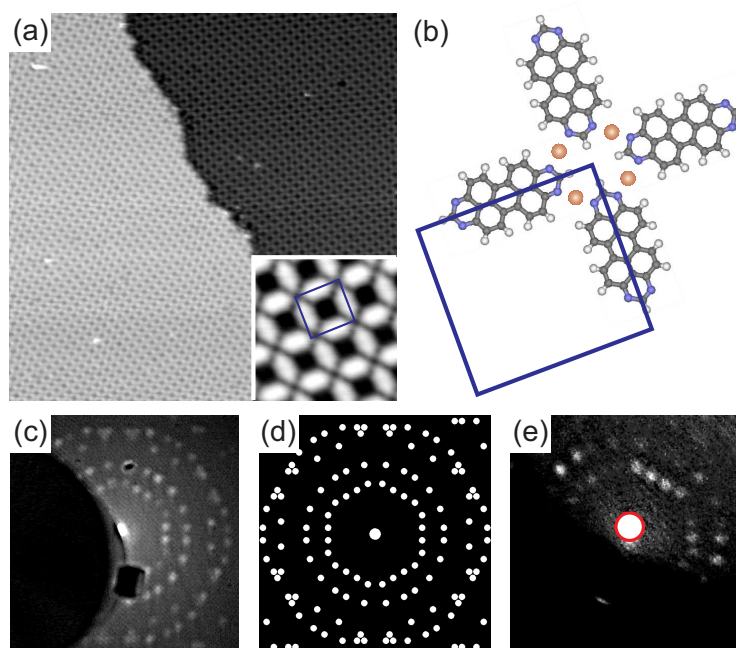


**Figure 4.3:** a) STM image of TAPP deposited on Cu(111) at a substrate temperature of 150°C (70 x 70 nm<sup>2</sup>, -1.4 V/20 pA). The inset in the lower right shows the porous structure in detail (5.3 x 5.3 nm<sup>2</sup>, -0.4 V/20 pA). b) Proposed model of the porous network. c) LEED pattern of the porous network taken with a beam energy of 29.5 eV. d) Simulated LEED pattern for comparison [68]. e) Zoom into first order spot of the Cu crystal (marked red). The LEED pattern was taken at 52 eV.

## 4.1.2 Metal coordination

### Formation of a porous coordination network

A highly ordered, porous network (Fig. 4.3) becomes the dominating structure after annealing at higher temperatures. This assembly is assigned as a coordination polymer in which the lone pairs of the nitrogen of TAPP coordinate to Cu adatoms (Fig. 4.3.b). While single pores are already observed after annealing at 0°C a full conversion into the porous network is achieved either by annealing the substrate at 150°C or by depositing TAPP while the substrate is held at 150°C. Both procedures allow the formation of large and homogeneous islands (Fig. 4.3.a).

The analysis of the LEED data (Fig. 4.3.c-d) supports a commensurate superstructure of the molecular ad-layer on the substrate. The matrix of the molecular ad-layer (Park and Madden) [79,80] was found to be:

$$\begin{pmatrix} 8 & 5 \\ -1 & 6 \end{pmatrix}.$$

Besides the fact that the LEED pattern (Fig. 4.3.c) is very well reproduced by the simulation (Fig. 4.3.d) using the above matrix there are two further aspects that

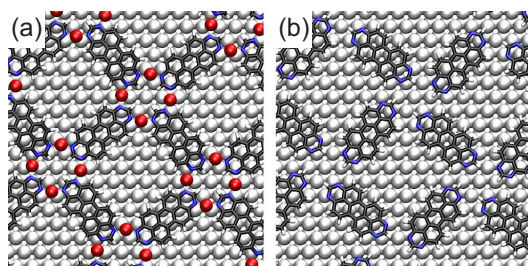


**Figure 4.4:** Minimal energy structures of the porous network of TAPP on Cu(111) with (a) and without adatoms (b). In the latter case the molecules interact via C-H...N hydrogen bonds. The DFT studies show that the metal coordinated structure (a) is energetically favored. Taken from [76].

support a commensurate ad-layer: On the one hand very large homogeneous islands of TAPP could be observed on the Cu surface (larger than  $100 \text{ nm}^2$  in size). On the other hand, the molecular LEED pattern around the (00)-spot (Fig. 4.3.c) is reproduced at the first order LEED-spot of the Cu substrate (Fig. 4.3.e).

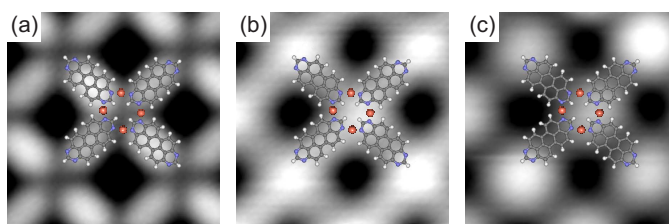
It is noted that the molecular layer is commensurate with the underlying Cu substrate which does not imply that the threefold symmetry of the underlying substrate has to result in a threefold symmetry of the molecular layer. For example, for PTCDA on Ag(111) an almost rectangular unit cell is observed which is commensurate to the Ag substrate [78].

### The role of metal atoms for the stability of the porous coordination network

Since the Cu-adatoms between the molecules of the porous network could not be identified by STM a molecular configuration stabilized by weak C-H...N hydrogen bonding would be another possibility to explain the observed structure. This is possible by slightly rotating the molecules (Fig. 4.4.b). DFT studies of the system, based on the unit cell of the porous network determined by LEED, with and without Cu adatoms (Fig. 4.4) show that the Cu coordinated system is energetically favored with respect to the metal-free two-dimensional aggregate.

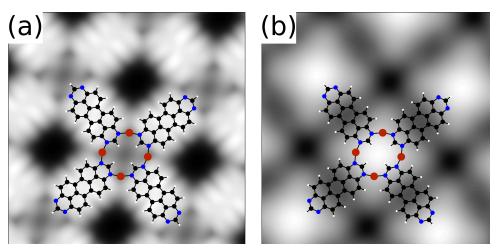
In absence of the adatoms TAPP relaxes into a structure stabilized by H-bonds between adjacent molecules. The adsorption energy in this case was found to be  $-0.33 \text{ eV/molecule}$  with respect to an isolated relaxed TAPP plus the relaxed Cu(111) surface. In the case of the coordinated assembly the adsorption energy was determined to  $-2.40 \text{ eV/molecule}$  relative to an isolated relaxed TAPP plus the relaxed Cu(111) surface with two adatoms. However, even if the energy cost for the creation of free adatoms from a step edge of  $0.76 \text{ eV/adatom}$  [81] is taken into account this structure is still energetically favored over the metal-free array. From the relaxed structure the N-Cu distance was determined to  $2.06 \text{ \AA}$  which agrees well with the values known from Cu coordination chemistry [82].

Besides this theoretical approach that supports the coordination to Cu-adatoms, a combined STM and DFT study allowed to indirectly evidence the Cu-adatoms.



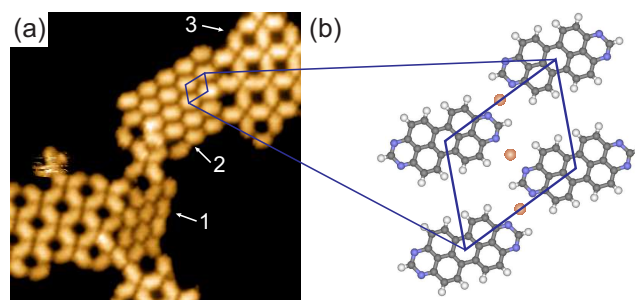
**Figure 4.5:** Series of STM images ( $4 \times 4 \text{ nm}^2$ ) of the porous network taken at 5 K at identical positions, but with different tunneling parameters: -1 V/20 pA (a), 2.7 V/1 pA (b), 3 V/1 pA (c). The molecular model is superimposed to illustrate equivalent positions. The crossing between the molecules dominates the STM image at sample voltages around 3 V.

Fig. 4.5 shows three STM images of the same area of the surface measured at different sample voltages. The superimposed molecular models highlight equivalent lateral positions. At a sample voltage of -1 V (Fig. 4.5.a) the STM topography is thought to depict the rectangular shape of TAPP. By increasing the sample voltage to 3 V the STM image changes significantly exhibiting now protrusions within the molecular crossings (Fig. 4.5.c). At first glance, these protrusions which emerge in the center of four Cu-adatoms may be related to an unoccupied resonance state that single Cu-adatoms exhibit on Cu(111) at an energy of 3.2 eV [83,84].



**Figure 4.6:** Simulated constant current STM images of the porous network of TAPP molecules on Cu(111) ( $4 \times 4 \text{ nm}^2$ ), with the LDOS integrated from the Fermi energy to (a)  $E_F - 1.0 \text{ eV}$  and (b)  $E_F + 3.2 \text{ eV}$ . This simulation was performed in the group of Prof. Persson.

In DFT studies this effect could be reproduced and is illustrated in simulated STM images of the relaxed porous surface coordination network on Cu(111) (Fig. 4.6). However, the bright protrusions are not observed in simulated STM images of the same structure without Cu-adatoms or the relaxed H-bond structure depicted in Fig. 4.4.b (data not shown here). Thus, the bright protrusion is considered as a “fingerprint” of the Cu-coordination. The DFT studies show that the protrusion originates from the orbital density localized on the Cu-adatoms. Although this state is thought to not contribute to the bonding between TAPP and the Cu-adatoms, the emergence of the protrusions is significantly influenced by the interaction of the adatoms with the nitrogen-lone-pair orbitals as well as with the LUMO of TAPP.



**Figure 4.7:** a) STM image of TAPP on Cu(111) after annealing at 80°C showing the close-packed assembly driven by vdW-interactions (1), a close-packed assembly driven by metal coordination (2) and the porous network (3) (17 x 17 nm<sup>2</sup>, -1.2 V/20 pA) b) Proposed model of assembly (2).

### A second surface network structure at sub-monolayer coverage

A second close-packed structure (“assembly 2” in Fig. 4.7.a) whose molecular interaction we also assign to be based upon Cu coordination is observed beside the vdW-structure (“assembly 1”) and the porous network (“assembly 3”) at annealing temperatures and times which are low enough to prevent the exclusive formation of the porous network, but high enough to activate Cu-coordination. Since this more densely packed array (assembly 2) is expected to prevail over the porous network (assembly 3) at coverages higher than the maximum TAPP coverage required for the porous network, all experiments were performed at sub-monolayer coverage in order to investigate its relationship with the other two ordered assemblies. Under these conditions the porous network discussed in the previous section was found to be the thermodynamically favored form of aggregation.

A detailed analysis of the STM images of assembly 2, considering different domains together with the symmetry of the substrate, results in two independent unit cells which do not overlap if rotations and mirror operations are constrained to those that are allowed by the symmetries of the substrate (see Appendix B.1). The dimensions of both unit cells only differ within the error margin of the STM and were found to be  $(11 \pm 1.1) \text{ \AA} \times (13 \pm 1.3) \text{ \AA}$ , included angle:  $64^\circ \pm 4^\circ$ . Using the information on the dimensions of both the unit cell and TAPP the overall N-Cu-N distance was found to be  $4 \text{ \AA} \pm 1.1 \text{ \AA}$ . At submonolayer coverages the fraction of molecules arranged in this structure did not exceed 15% compared to the overall number of molecules forming the three ordered structures (Fig. 4.7.a).

### The supply of Cu adatoms for the surface coordination network

Literature reports the formation of metal organic complexes [19, 85–87] both by co-deposition of metal atoms [19, 88, 89] and by coordination to free adatoms on Cu(100) and Cu(111) [18, 86, 90]. The latter publications [18, 90] describe the reservoir of Cu adatoms as a result of a continuous attachment/detachment of Cu atoms from step edges. While the formation of surface coordination networks on Cu(100) is already



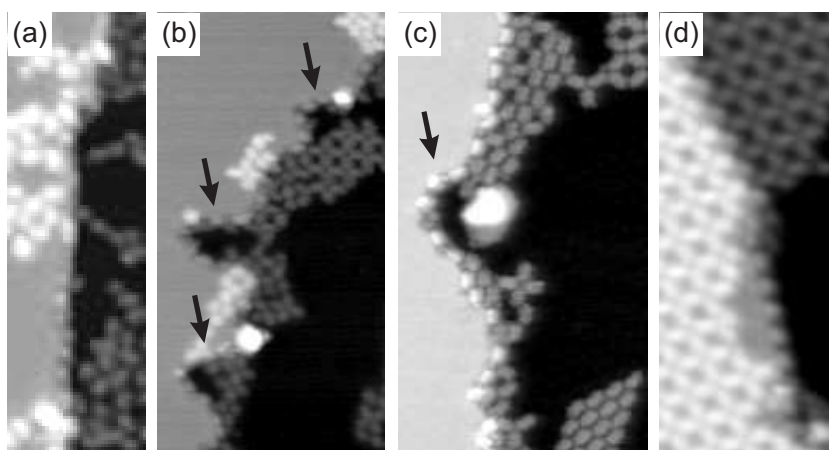


**Figure 4.8:** Step decoration at different temperatures: a)  $-110^{\circ}\text{C}$  ( $6 \times 19 \text{ nm}^2$ ,  $-1.5 \text{ V}/12 \text{ pA}$ ). b) Room temperature (RT) ( $19 \times 36 \text{ nm}^2$ ,  $-1.3 \text{ V}/20 \text{ pA}$ ). c) RT ( $15 \times 27 \text{ nm}^2$ ,  $-1.3 \text{ V}/20 \text{ pA}$ ). d)  $150^{\circ}\text{C}$  ( $9 \times 23 \text{ nm}^2$ ,  $-1.4 \text{ V}/20 \text{ pA}$ ). The black arrows highlight “bays” at the steps that are also decorated by TAPP molecules.

observed at room temperature (RT) [90] the coordination on Cu(111) is observed at elevated temperatures around  $150^{\circ}\text{C}$  [18]. At RT Schunack et al. [91] observed the formation of Cu nanostructures *below* molecules on Cu(110) mainly at step edges and very rarely on terraces. The latter effect has been related to the low concentration of Cu adatoms at RT, whilst the formation of nanostructures (both at steps and on terraces) was thought to be thermally activated as no nanostructures were observed after adsorption of the molecules at temperatures  $<150 \text{ K}$ . According to Giesen [92] the concentration of adatoms on Cu surfaces at RT is of the order of  $10^{-9}$  per surface atom. This is far too low to account for the formation of significant levels of surface coverage of coordination networks. Hence, the temperature dependent detachment/attachment rate of adatoms from kinks is of importance because it determines the time the system needs to compensate for a perturbation of the equilibrium concentration of free adatoms caused by their coordination to molecules.

Given the Arrhenius dependence of the detachment rate on Cu(111) [81] the observation of large assemblies based on Cu coordination after annealing at temperatures around or slightly above room temperature is an unexpected result. Comparison of the number of Cu atoms being expected to detach from kinks according to [81] to the number of atoms which are needed to form the metal coordinated assemblies (for an estimate, see Appendix B.2) raises the question of further possible mechanisms for the supply of Cu atoms required for the formation of the Cu/TAPP coordination networks.

At  $600 \text{ K}$  the mass transport on Cu(111) at step edges is reported to be dominated by the exchange of atoms with the neighboring terrace whereas the dominating mass transport at temperatures below  $500 \text{ K}$  is diffusion along steps [81, 93]. The latter range is relevant for the formation of the metal coordinated assemblies in our case and might explain the affinity of TAPP to step edges which can be observed as step

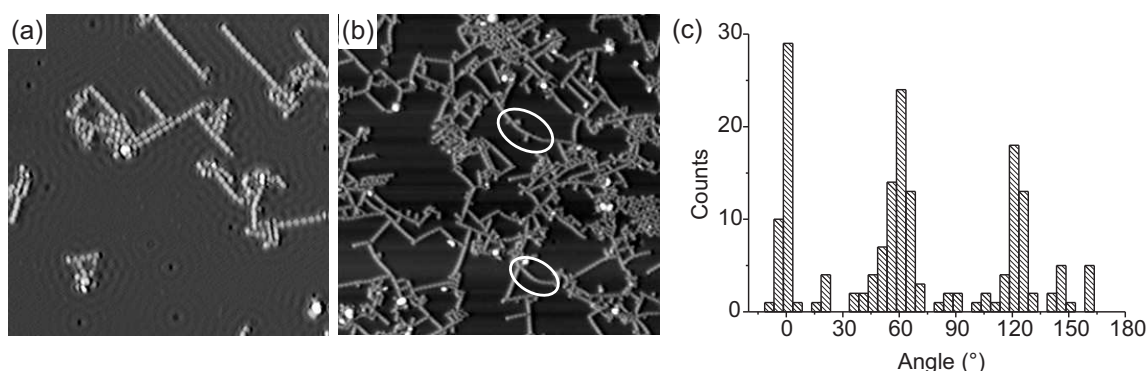


**Figure 4.9:** a) STM-image of the TAPP chains at low coverage ( $50 \times 50 \text{ nm}^2$ ,  $-0.1 \text{ V}/20 \text{ pA}$ ) obtained after annealing at  $240^\circ\text{C}$ . Owing to the low tunneling voltage used to acquire this STM image, standing wave patterns in the Shockley surface state of Cu(111) as they arise from scattering at chains as well as defects can be observed [46, 47]. b) Sample at higher submonolayer coverage after annealing at  $280^\circ\text{C}$  ( $80 \times 80 \text{ nm}^2$ ,  $-1 \text{ V}/90 \text{ pA}$ ). The areas highlighted by the ellipses show a curved arrangement of some chains, which is a first indication for a dominating intermolecular interaction. c) Histogram showing the directions of alignment of 178 chains at low coverage. An STM image with atomic resolution was used for calibration so that  $0^\circ$  corresponds to one of the high symmetry directions of the Cu substrate.

decoration at various temperatures (Fig. 4.8). Especially the observation of “bays” at room temperature (RT) (Fig. 4.8.b-c) is a first indication that the molecules are able to remove adatoms from step edges [86], in other words, they are thought to have a *direct “corrosive” effect* on the substrate. As previously referred to [91], the formation of Cu nanostructures below molecules at steps supports this interpretation as their strong affinity to metal atoms induces the detachment of Cu atoms from steps.

### 4.1.3 C-C coupling between TAPP molecules

#### Indications for covalent couplings

After annealing at temperatures of approximately  $250^\circ\text{C}$  TAPP forms covalently bonded chains (Fig. 4.9.a-b). This thermally induced formation of macromolecules is interpreted in terms of the tautomerization of the N-heterocyclic end units of the TAPP molecules to carbene intermediates, *iso*-TAPP (cf. Fig. 4.11). Whilst this postulated reaction pathway avoids high energy intermediates which would result from the direct C-H bond cleavage and the subsequent recombination of radical intermediates, the latter cannot be ruled out. This issue is addressed later in greater detail.

DFT studies in the gas phase carried out in the group of Prof. Gade showed that the formation of pyrimidine dimers through a carbene intermediate is an endothermic process whereas the formation of an *iso*-TAPP-dimer is thermoneutral. This trend is enhanced in the formation of oligomers, which becomes an exothermic process for the generation of the trimer and even more so for higher oligomers [29].

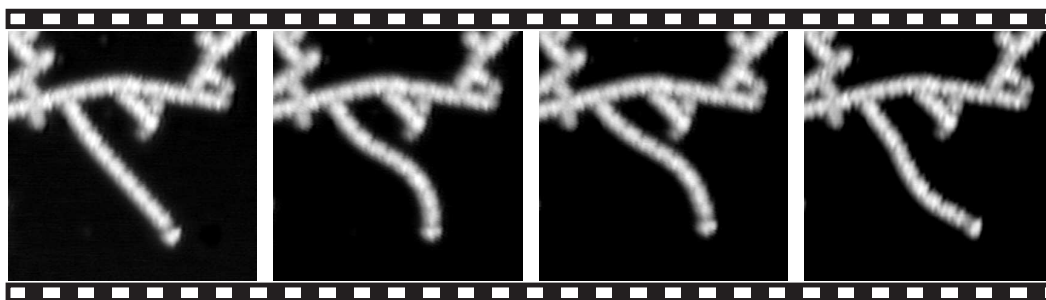


**Figure 4.10:** Consecutive STM images of the same area ( $16 \times 16 \text{ nm}^2$ ,  $-1.2 \text{ V}/20 \text{ pA}$ ). The STM tip was used in proximity to the sample to induce lateral motion of the chain between each of the micrographs displayed. These four images (taken from a sequence of nineteen images) demonstrate the successful and reversible bending of a chain that stays intact during the process. The degree of bending and the elasticity of the system are remarkable.

The curved arrangement of some chains shows that their orientation is not determined by the substrate lattice structure (Fig. 4.9.b). This gave a first indication that the interaction between the monomers in the chains dominates over the bonding to the metal surface.

An important consequence of the covalent linkage of the N-heterocyclic aromatic molecules on the metal surface and thus the strong bonding interactions between the monomeric units is the possibility to mechanically manipulate whole chain sections with the aid of the STM tip, see e.g. [94–96]. To this end, the following manipulation sequence was applied, the tunneling parameters being set to  $1.2 \text{ V}/20 \text{ pA}$  during this sequence: First, the STM tip was placed next to the chain, the feedback loop subsequently switched off, and the tip was slowly moved towards the surface by approximately  $0.7 \text{ nm}$  and then retracted to its initial position. The success of this procedure was checked by imaging the same region again. In Figure 4.10, four images are displayed which clearly show that such a manipulation has left the chain intact, thereby illustrating its elasticity as a whole. These four images are part of a manipulation series consisting of 19 manipulations of the chain. The intactness of the chain after the manipulation provides additional support for the assumption of a strong bonding of the monomers of the chain.

Despite the apparently arbitrary arrangement on the surface and the strong intermolecular interactions the Cu surface might still influence the growth of the chains. By statistical analysis of the orientations of the chains with respect to the principal directions of Cu(111), the possible influence of the surface on their alignment is studied. Samples with low molecular coverage were used for this study in order to minimize interactions between chains. The resulting histogram (Fig. 4.9.c) shows the alignment of 178 chains. It exhibits three pronounced directions with a difference of  $60^\circ$ . By considering the symmetry of the (111) surface (rotations by  $60^\circ$  and mirror operations along the high symmetry directions if the relevant surface is restricted to the topmost layer) the possibilities of attributing the pronounced directions to the underlying sub-

**Table 4.1:** Calculated overall reaction energies of three different types of chains. Taken from [76].

Type of chain	$E_{\text{react}}$ [eV/molecule]
poly( <i>iso</i> -TAPP)	-1.10
poly(TAPP)	+0.28
poly(TAPP-Cu)	-2.25

strate are reduced to either an alignment along the high symmetry directions or an alignment along an axis rotated by  $30^\circ$  with respect to the high symmetry directions. An STM image with atomic resolution was used to further reduce the number of possibilities to the first one so that  $0^\circ$  in the histogram corresponds to one of the high symmetry directions of the Cu(111) surface.

Both the distance of  $12.7 \text{ \AA}$  between the monomers determined by gas phase calculations [29] and the STM result of  $12 \text{ \AA}$  (cf. Fig. 4.13) are in good agreement to the fivefold distance of the lattice constant of the (111) surface ( $5 \times 2.56 \text{ \AA} = 12.8 \text{ \AA}$ ). This allows a commensurate arrangement of the majority of the chains thus implying that this arrangement may be energetically favored. However, a significant number of chains are not aligned along the high symmetry directions and many of the angles are too large to be explained by statistical errors (e.g. directions of  $90^\circ$  or  $150^\circ$ ). This observation indicates that the bonding between the monomer units in oligomeric molecules clearly dominates over the interaction with the metal surface.

### The chemical nature of the (TAPP)<sub>n</sub> chains

The proposed chemical nature of the polymeric chains generated in the surface-thermolysis of the Cu/TAPP network structure, along with a reaction pathway for their generation, is summarized in Figure 4.11. TAPP molecules could undergo a metal-mediated rearrangement to *iso*-TAPP on the copper surface and subsequently combine to the oligomeric chains poly(*iso*-TAPP) observed in our study. Moreover, in analogy to the thermal dehydrogenation reported for another perylene-derivative on Cu(111) [36,37] the chain structures here could undergo a dehydrogenation step subsequent to the coupling which results in poly(TAPP). This could allow for a coordination to Cu-adatoms leading to poly(TAPP-Cu). An alternative reaction path for the polymerization could be based on direct C-H bond activation and recombination of the resulting radicals (Fig. 4.11). Such a high energy reaction pathway has been postulated in a recent report on the surface polymerization of porphyrins [30].

Whilst the reaction pathway leading to the TAPP chains could not be established with the available theoretical and experimental tools, we focused on the detailed identification of the polymeric structures, in particular, to distinguish between the three possibilities represented in Figure 4.11, poly(*iso*-TAPP), poly(TAPP), poly(TAPP-Cu). For this purpose DFT studies were carried out to compare their overall reaction

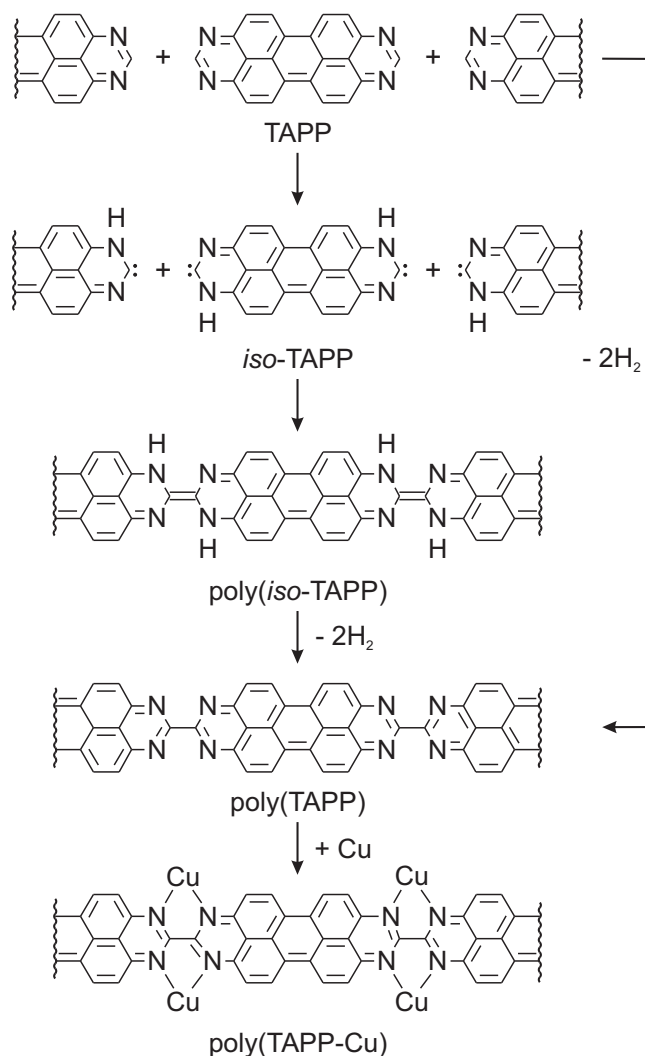


**Figure 4.11:** Proposed surface mediated transformation of TAPP to poly(TAPP) and its metal decorated form poly(TAPP-Cu). Taken from [76].

energies on the surface (Table 4.1). Isolated relaxed TAPP molecules and the relaxed Cu substrate (with adatoms for the adatom coordinated structure) were used as reference systems. For the dehydrogenation process the Cu substrate was assumed to work as catalyst, i.e. the energy of atomic hydrogen adsorbed on Cu(111) of approximately  $-3$  eV/atom is included in the overall reaction energies of poly(TAPP) and poly(TAPP-Cu).

Both poly(*iso*-TAPP) and the adatom coordinated poly(TAPP-Cu) chains are energetically favored with respect to the reference system whereas the formation of poly(TAPP) is clearly disfavored. Again, the generation of Cu adatoms from steps at  $0.76$  eV/atom [81] would reduce the exothermicity of the poly(TAPP-Cu) chain. However, at the elevated temperatures needed for the polymerization ( $T \approx 250^\circ\text{C}$ ) the detachment rate from kinks should allow for a supply with enough Cu adatoms.

**Table 4.2:** Calculated chemical shifts for the different types of chains using two different approaches. The reference is the N1s peak of the porous network. Besides the Z+1 approach a core-ionized potential was used to calculate the chemical shifts. Both approaches exhibit a good agreement. Taken from [76].

Type of chain	Z+1 [eV]	Core-ionized potential [eV]
poly( <i>iso</i> -TAPP)		
C-NH-C	-0.431	-0.433
C-N=C	1.708	1.535
poly(TAPP) (C=N-C)	-0.868	-0.824
poly(TAPP-Cu) (N-Cu)	-0.227	-0.234

The nitrogen atoms in the three chain structures of poly(*iso*-TAPP), poly(TAPP) and poly(TAPP-Cu) exhibit chemically different environments, which furthermore differ from the chemical environment in the porous surface coordination network. Thus XPS was used to differentiate between the three structural models. Being a laterally averaging technique XPS is in this case especially suitable to determine the dominating type of chain. The XPS data presented in [29] could be reproduced with high accuracy using synchrotron radiation. However, on the basis of the preceding structural discussion as well as the calculations of chemical shifts the original interpretation in [29] had to be reconsidered.

The XPS N1s spectra of the surface coordination network Cu/TAPP is depicted in Figure 4.12.e at the top, the single peak being consistent with the chemical equivalence of all N-donor atoms in the porous surface coordination network. After annealing and formation of the irregular surface assemblies of covalent chains this XPS peak is slightly broadened and shifted by 0.21 eV towards lower binding energies. Given the quality of the data, it is assumed that this spectrum also corresponds to a single N-atom environment. The similarity of the chemical shifts before and after thermolysis of the porous surface coordination network supports similar overall chemical environments of the N-atoms in both cases. The comparison of the calculated shifts (Fig. 4.12.a-c) to the experimental results (Fig. 4.12.d-e) illustrates excellent agreement between the calculated shift of poly(TAPP-Cu) and the fit of the XPS spectra. This indicates that poly(TAPP-Cu) prevails.

The good agreement between experimental results and theoretical studies is also reflected in the correspondence between simulated STM images of the chains at low voltages (Figure 4.13.a and c) and their experimental counterpart (Fig. 4.13.b). It is noted that the simulated STM images of poly(*iso*-TAPP) and poly(TAPP-Cu) do not reveal any visible differences. Both images exhibit a significant electron density between the TAPP monomers which is a further indication for a covalent linkage between the monomers.

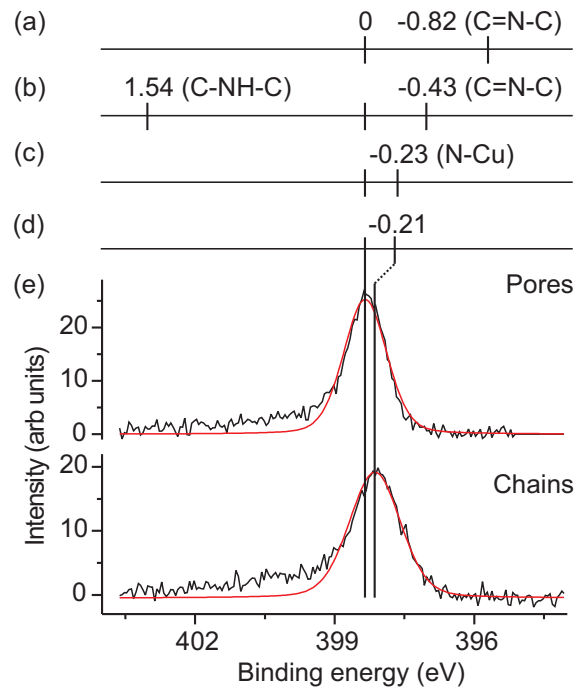


**Figure 4.12:** Chemical shifts using a core-ionized potential for poly(TAPP) (a), poly(iso-TAPP) (b) and poly(TAPP-Cu) (c); see Table 4.2. d) Chemical shift determined from the fits of the XPS N1s spectrum of the porous network and the chains (e). All chemical shifts are referred to the N1s peak of the porous network.

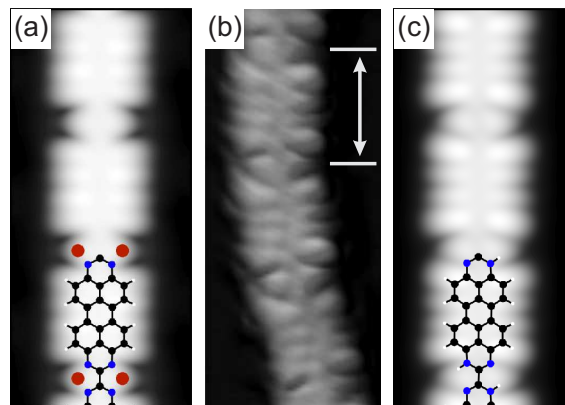


**Figure 4.13:** a) Simulated STM image of poly(TAPP-Cu). b) STM image of a TAPP chain in detail (1.8 x 4 nm<sup>2</sup>, -0.6 V/20 pA) which corresponds well to the simulated STM images in (a) and (c). The distance between the monomers (gray arrow) was determined by STM to  $(1.2 \pm 0.12)$  nm. c) Simulated STM image of poly(iso-TAPP). Both simulated STM images show the LDOS integrated from the Fermi level to -0.6 eV, thus corresponding in first order to a constant current image at -0.6 V.

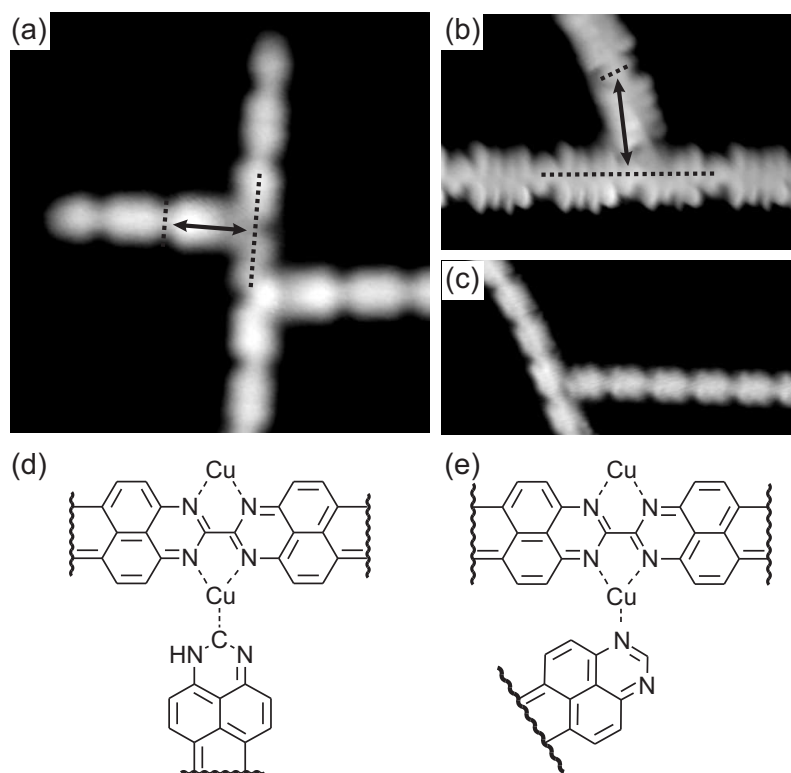


**Figure 4.14:** Different types of connections between chains. a) The first one ( $7.3 \times 7.3 \text{ nm}^2$ ,  $-1 \text{ V}/20 \text{ pA}$ ) typically exhibits a chain that attacks centrally between two monomers of another chain with an angle of approximately  $90^\circ$ . The proposed structure is shown in (d). b – c) The second type is shown in (b) ( $4.8 \times 3.1 \text{ nm}^2$ ,  $-0.6 \text{ V}/20 \text{ pA}$ ) and (c) ( $10.2 \times 4.9 \text{ nm}^2$ ,  $0.1 \text{ V}/20 \text{ pA}$ ). In this case the chain attacks slightly off center with variable angles between  $60^\circ$  and  $70^\circ$  which were determined by STM. The corresponding sketch (e) illustrates the proposed model. The distances between the midpoints of the black dotted lines in (a) and (b) are determined by STM to ( $16 \pm 1.6$ ) Å (a) and ( $15 \pm 1.5$ ) Å (b).

### The nature of inter-chain contacts

While a high (local) coverage may exhibit a quite cluttered picture of variously interacting chains, STM images at low (local) coverage indicate two major types of “junctions” (Figure 4.14). Our interpretation of the chain structures as poly(TAPP-Cu) readily offers an explanation for these structural motifs. In both cases the connection is thought to be based on Cu coordination occurring on one side between two adjacent nitrogen atoms in the interstice between two monomers of one chain. On the other side Cu coordinates either to the carbene of the tautomerized chain end (Fig. 4.14.d) or to one of the nitrogen atoms of the pyrimidine end group (Fig. 4.14.e). Both types can be distinguished by STM as the respective connecting angles are different. Furthermore detailed STM images show that the joining chain binds either centric (Fig. 4.14.a) or off-center (Fig. 4.14.b).



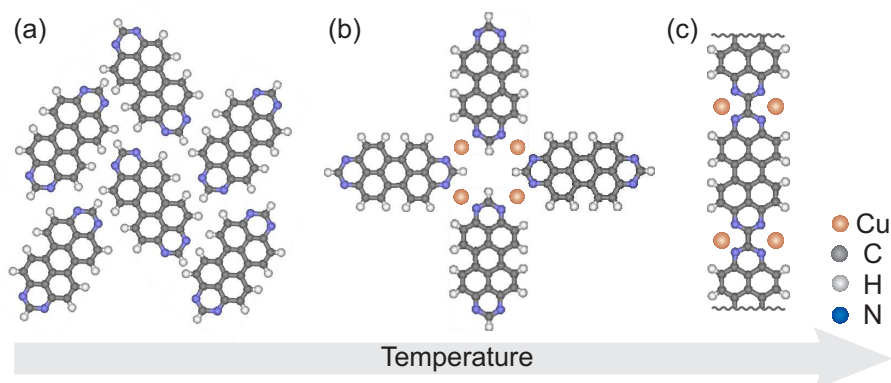


**Figure 4.15:** From vdW-interaction (a) via Cu-coordination (b) to covalent bonds (c). Thermal regimes of the assembly of 1,3,8,10-tetraazaperopyrene (TAPP) on Cu(111).

For a further characterization of the junctions the distances between the midpoints of the black dotted lines (as indicated in Fig. 4.14.a and Fig. 4.14.b) were determined to  $(16 \pm 1.6)$  Å (Fig. 4.14.a) and  $(15 \pm 1.5)$  Å (Fig. 4.14.b) by STM. They compare quite well to the values expected from the corresponding chemical models ( $17.0$  Å to  $17.8$  Å and  $16.1$  Å to  $16.8$  Å, respectively) in which a Cu-C distance of  $2.1$  Å is used and the Cu-N distance is varied between  $1.8$  Å and  $2.5$  Å. It is noted that the assumption of the minimal Cu-N distance results in a significant overlap of the vdW orbitals of adjacent hydrogen atoms.

#### 4.1.4 Summary

The combination of experimental techniques (STM and XPS) and DFT calculations allowed for a detailed study of the chemistry of tetraazaperopyrene (TAPP) on Cu(111) under UHV conditions. Depending on the annealing temperature TAPP forms three main assemblies at submonolayer coverage based on different intermolecular interactions: A close-packed assembly whose molecules interact via vdW-forces, a Cu coordinated porous network and covalently linked molecules that form chains (Fig. 4.15) were observed.

The Cu substrate is of crucial importance, in particular for the formation of the porous surface coordination network because it provides Cu-adatoms for the metal coordination. Moreover, DFT studies on the chains and XPS experiments indicate that the dominating type of chain is also coordinated to Cu adatoms. Here the Cu surface and its adatoms are thought to act catalytically for reaction pathways which are inaccessible in the bulk and for the stabilization of reactive intermediates before they recombine. Especially at elevated sample temperatures the supply with free Cu adatoms is expected to be provided by the detachment from steps. Due to the formation of surface coordination networks which could already be observed around room temperature a “corrosive” effect of TAPP on the step edges is discussed as an additional mechanism supplying the molecules with the necessary adatoms.

## 4.2 Preliminary studies on the formation of covalent couplings in other systems

### 4.2.1 Tetraazapyrene (TAP) on Cu(111)

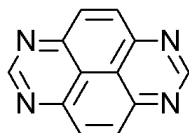


**Figure 4.16:** 1,3,6,7-tetraazapyrene (TAP)

This section deals with the question whether the “pyrimidine-based” polymerization of TAPP on Cu(111) can be extended to other (similar) molecules. This would help to establish a general mechanism for the formation of covalent couplings on surfaces in UHV by means of “surface chemistry”. For this purpose Tetraazapyrene (TAP) (Fig. 4.16) was synthesized in the group of Prof. Gade and studied on Cu(111).

The sublimation of TAP could not be detected by a quartz crystal microbalance (QMB). Instead a quadrupole mass spectrometer (QMS) was used that allowed to determine the temperature at which TAP begins to flood the chamber. Information on the partial pressure of TAP provided by the QMS and the time the substrate was exposed to TAP allowed for a rough control of the coverage. In this setup TAP was simply heated in a glass crucible (see section 2.4) to approximately 75°C. This setup could significantly be enhanced if TAP was heated in a separated vacuum and dosed into the preparation chamber via a leak-valve, in analogy to a liquid deposition system. Thus the partial pressure and the exposure time could be controlled accurately.

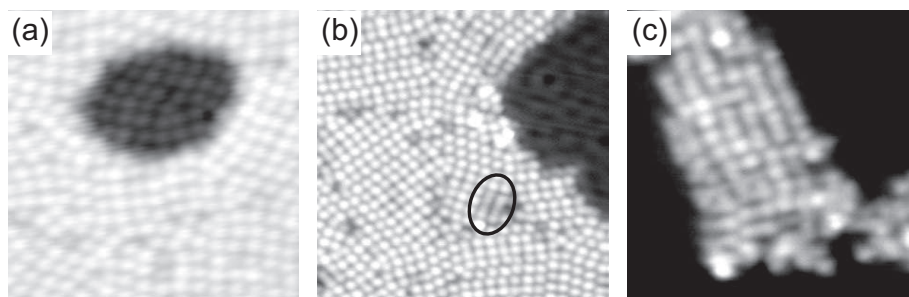


**Figure 4.17:** STM images of TAP after deposition on Cu(111) held at room temperature (RT). The coverage exceeds one monolayer (ML). a) TAP growing in two layers after annealing at 165°C (13 x 13 nm<sup>2</sup>, -0.1 V/10 pA). b) After annealing at 215°C a submonolayer of TAP is observed (20 x 20 nm<sup>2</sup>, -10 mV/10 pA). The black ellipse highlights chainlike structures. c) A notable change is observed after annealing at 265°C: Most of the TAP is desorbed and the remaining molecules form clusters (12 x 12 nm<sup>2</sup>, -10 mV/10 pA).

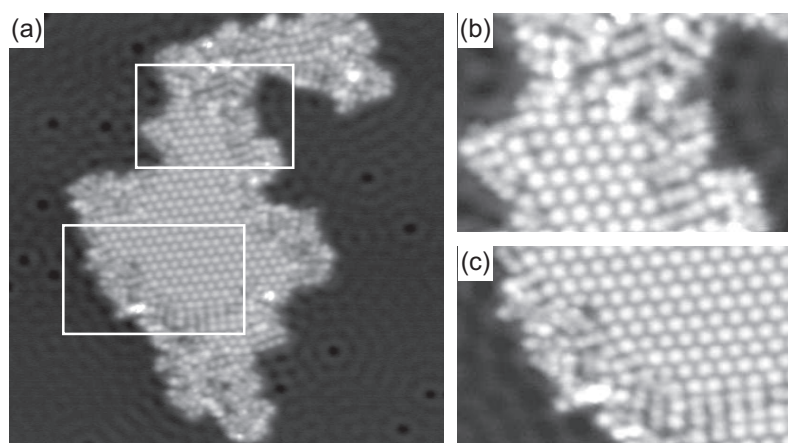


**Figure 4.18:** STM images of TAP/Cu(111) annealed at 245°C illustrating the transition to chainlike structures. a) The overview shows the preferential growth of these chainlike structures at the edge of the island (36 x 36 nm<sup>2</sup>, -10 mV/10 pA). The parts highlighted by the white rectangles are shown in detail in (b) (13 x 8.5 nm<sup>2</sup>, -10 mV/10 pA) and (c) (15 x 9 nm<sup>2</sup>, -10 mV/10 pA).

For the temperature dependent study in Fig. 4.17 the initial coverage exceeded 1 ML. Besides the observation of TAP growing in layers of different height (Fig. 4.17.a) the absence of the bare metal surface in STM indicated such coverage. It significantly reduced to a submonolayer upon annealing at 215°C (Fig. 4.17.b). Moreover first transformations to “chainlike structures” were observed (black ellipses in Fig. 4.17.b), i.e. the STM did not resolve single molecules. Annealing at 265°C resulted in a further decrease of the coverage and the formation of clusters. Some of them still exhibit chainlike structures (Fig. 4.17.c) although the missing reference of resolved single molecules does not exclude a bad resolution of the STM in this case. The formation of isolated long chains in analogy to TAPP/Cu(111) could not be observed. In additional experiments the annealing conditions for the transformation were further specified to a temperature range between 240°C and 250°C (Fig. 4.18). This allowed for the observation of these chain-like structures besides the close-packed structure of TAP. As the latter structure exhibits “separated” molecules it was used as reference to ensure that the observation of chain-like structures does not result from a bad STM resolution.

### 4.2.2 Polymerization in two dimensions

The formation of covalent bonds by means of chemical reactions that are directly induced on surfaces in UHV has drawn much attention recently [27–33]. The relevance of these studies in current research is further shown in [26, 34] in which the contributions to this field and their perspectives are discussed. In this context the formation of a porous network based on covalent bonds would significantly add to this field as its stability could exceed the stability of conventional approaches based on

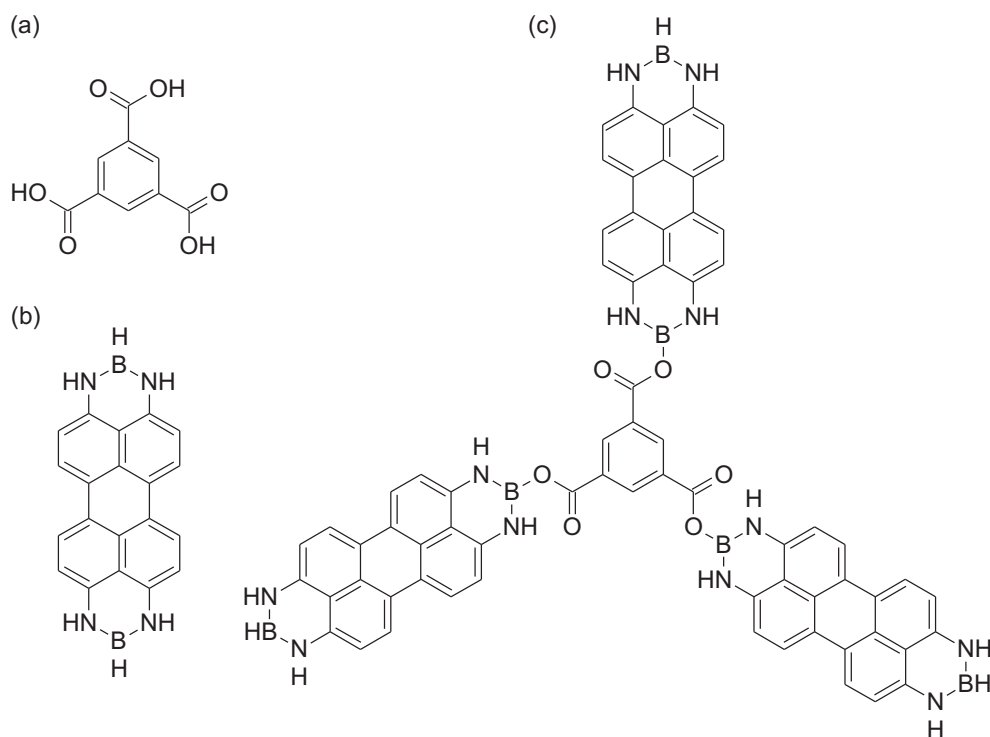


**Figure 4.19:** a) Benzene-1,3,5-tricarboxylic acid (trimesic acid – TMA). b) N,N',N'',N'''-diborylene-3,4,9,10-tetraaminoperylene (DIBOTAP). c) The covalent linking of TMA and DIBOTAP under the release of hydrogen may result in the formation of a two dimensional porous network.

H-bonds [37, 70] or metal coordination [19]. In principle this network would consist of a single macromolecule. The extension to two dimensions [28] and the formation of porous networks based on covalent bonds [31, 33] are first promising approaches that indicate the ongoing challenge to design highly ordered covalent structures in two dimensions on surfaces.

Our approach is based on the combination of N,N',N'',N'''-diborylene-3,4,9,10-tetraaminoperylene (DIBOTAP) and benzene-1,3,5-tricarboxylic acid (TMA) as illustrated in Fig. 4.19. After depositing first DIBOTAP and second TMA on a Ag(111) crystal held at room temperature single DIBOTAP (Fig. 4.20.b) as well as a honeycomb structure of TMA (Fig. 4.20.c) could be observed whereas an ordered mixed assembly of both molecules was not observed. The TMA network is described in [97,98]. Besides, the occasional observation of trimers already indicates the expected covalent coupling of both molecules (Fig. 4.20.b).

After annealing at 120°C pores with varying size and geometry were observed (Fig. 4.20.d). The observed protrusions inside some pores are assigned as TMA. Several pores exhibit the desired hexagonal structure (Fig. 4.20.e) whereas most angles between the DIBOTAP monomers differ from the expected 120°. The observation of varying angles between the DIBOTAP monomers is thought to be based on the conformational flexibility of the CO and OB bonds of the TMA-DIBOTAP building block

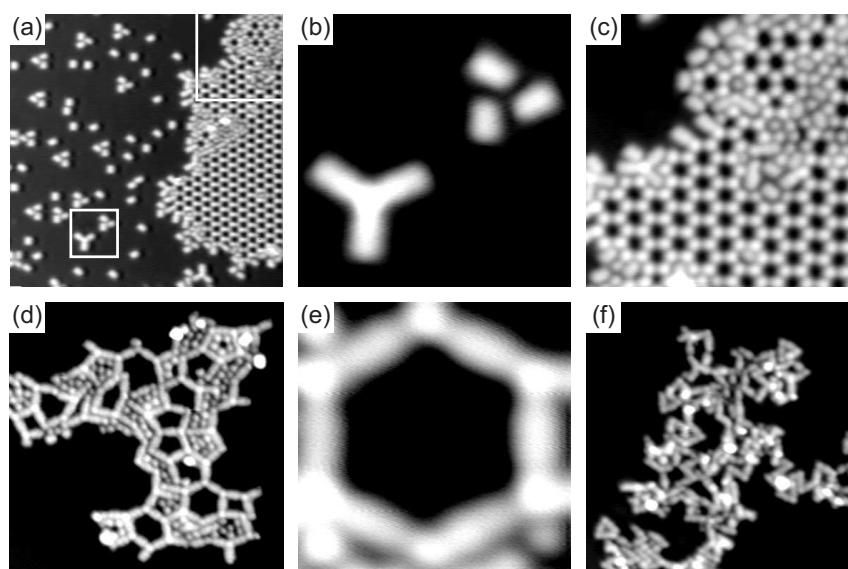


**Figure 4.20:** Submonolayer of DIBOTAP and TMA studied by STM at 5 K. The images were recorded after depositing first DIBOTAP and second TMA on a Ag(111) crystal held at room temperature. a) Overview ( $40 \times 40 \text{ nm}^2$ ,  $-1 \text{ V}/20 \text{ pA}$ ). b) Detail of (a): DIBOTAP and a crossing that is thought to show the desired combination of both building blocks according to Fig. 4.19.c ( $6.6 \times 6.6 \text{ nm}^2$ ,  $-0.1 \text{ V}/20 \text{ pA}$ ). c) Detail of (a): The porous TMA network ( $16 \times 16 \text{ nm}^2$ ,  $-1 \text{ V}/20 \text{ pA}$ ). d) After annealing at  $120^\circ\text{C}$  a porous structure is observed whose different pore geometries support varying angles between two DIBOTAP monomers ( $25 \times 25 \text{ nm}^2$ ,  $-1 \text{ V}/20 \text{ pA}$ ). The protrusions inside the pores are assigned as TMA. e) A hexagonal pore in detail ( $4.3 \times 4.3 \text{ nm}^2$ ,  $-0.5 \text{ V}/20 \text{ pA}$ ). f) An annealing temperature of  $270^\circ\text{C}$  led to decomposition effects ( $30 \times 30 \text{ nm}^2$ ,  $-1 \text{ V}/20 \text{ pA}$ ).

(cf. Fig. 4.19). Moreover, a dehydrogenation of the NH group cannot be ruled out so that the N-atoms may also be involved in covalent interactions. An annealing temperature of  $270^\circ\text{C}$  indicated a decomposition of the molecular assemblies (Fig. 4.20.f).

A reason for the absence of an ordered assembly may be the formation of covalent bonds: The concepts of self-assembly on surfaces which are inspired by supramolecular chemistry heavily rely on self-correction that is inherent to reversible and thus weak interactions, such as H-bonds. This principle is thwarted by the use of covalent bonds. In other words: If two molecules are covalently linked it is almost impossible to separate them to form a more suitable structure. Thus, the annealing procedure and in particular the cooling process is thought to affect the formation of an ordered assembly so that the choice of an appropriate preparation strategy may provide a homogeneous structure. In [34] the authors comment on this aspect of self-correction and discuss a reaction that was used in [27]. In this reaction an aldehyde ( $-\text{CHO}$ ) and an amine ( $-\text{NH}_2$ ) are linked to form an imine bond ( $-\text{CH}=\text{N}-$ ). For recovering the reactants the by-product water could hydrolyze the imine bond. However, such a strategy would become impossible in UHV.

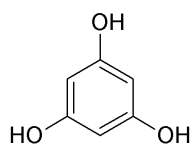


**Figure 4.21:** 1,3,5-trihydroxybenzene. In contrast to TMA this molecule, that was synthesized in the group of Prof. Gade at the University of Heidelberg, only exhibits hydroxyl groups instead of carboxylic groups.

An alternative molecular linker (Fig. 4.21) which carries an hydroxyl group instead of a carboxylic group might reduce the conformational variability of the DIBOTAP-TMA building block. This could result in more homogeneous structures. However, the small mass of the molecule did not allow for a “traditional” sublimation, i.e. molecules are heated and detected by a QMB. Alternatively, the previously described detection with a QMS (section 4.2.1) should also be possible in this case thus allowing for additional promising studies on this system.

## 5 A porous molecular network on Cu(111)

The work presented in this chapter is the direct continuation of one of the two projects in the PhD thesis of Markus Wahl [36]. In this project, done in collaboration with the inorganic chemistry group of Prof. Gade in Heidelberg, the perylene derivative 4,9-diaminoperylene-quinone-3,10-diimine (DPDI) [99], was studied on metal surfaces in UHV. On Cu(111), a dehydrogenation of DPDI induced by thermal annealing (Fig. 5.1.a) results in the formation of coverage dependent assemblies [36,37]. By choice of the appropriate molecular coverage before annealing this chemical reaction allows for the formation of a highly stable hexagonal porous network (Fig. 5.1.b) which is commensurate with the substrate. So far, this network was used as a stable template to study molecular guests that were trapped in the pores [36,100,101].

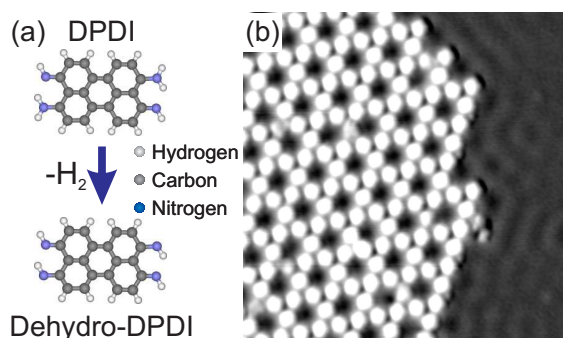


**Figure 5.1:** Interaction of the dehydro-DPDI network with the surface state of the underlying substrate. The formation of this porous network is based upon a thermally induced dehydrogenation of DPDI on Cu(111). a) Molecular structure of DPDI and its dehydrogenated form. b) STM image ( $29 \times 29 \text{ nm}^2$ ,  $-0.1 \text{ V}/50 \text{ pA}$ ) for submonolayer coverage of DPDI deposited on Cu(111) after thermal annealing at  $200^\circ\text{C}$ . Dehydro-DPDI acts as both hydrogen-bond donor and acceptor to produce a very stable self-assembled porous network [36,37]. The network periodicity is  $2.55 \text{ nm}$  with a pore diameter of  $1.6 \text{ nm}$ . Standing wave patterns in the Cu surface state arise from the scattering of the delocalized electronic states at the border of the adsorbate adlayer [46,47].

Against the background that the porous network exhibits an extraordinary high stability, the fact that the intermolecular interactions are based on H-bonding is surprising. In [37] a strong interaction of the network with the Cu support is discussed

**Table 5.1:** a) XSW results for DPDI/Cu(111) in the mobile phase which is present before annealing the sample. For each nitrogen species 14 photoelectron yield curves were analyzed, whereas for the carbon species 15 photoelectron yield curves were analyzed. b) XSW results for dehydro-DPDI/Cu(111) in the porous network which develops after annealing. In this case 8 photoelectron yield curves were analyzed for carbon as well as for nitrogen. The errors represent the standard deviations.

	a) Mobile phase		b) Porous network	
	Height	Coh. fraction	Height	Coh. fraction
Amine N	$2.20 \text{ \AA} \pm 0.03 \text{ \AA}$	$0.66 \pm 0.06$		
Imine N	$2.4 \text{ \AA} \pm 0.11 \text{ \AA}$	$0.27 \pm 0.06$	$2.83 \text{ \AA} \pm 0.03 \text{ \AA}$	$0.50 \pm 0.08$
Carbon	$2.68 \text{ \AA} \pm 0.06 \text{ \AA}$	$0.47 \pm 0.04$	$3.00 \text{ \AA} \pm 0.04 \text{ \AA}$	$0.46 \pm 0.05$

as a possibility to explain this stability. Thus, for the work at hand, the molecular adsorption heights as well as the electronic structure of DPDI/Cu(111) close to the Fermi energy were studied in detail. The results of these further investigations are discussed in Section 5.1. Besides this possibly stabilizing influence of the substrate on the molecular surface structure, which is discussed on the level of single molecules, the influence of the network as a periodic structure on the electronic structure of the substrate is studied in Section 5.2. This change of perspective gave rise to an extraordinary effect on the surface state of Cu(111).

## 5.1 Stability of the porous network

### 5.1.1 Determination of the adsorption height

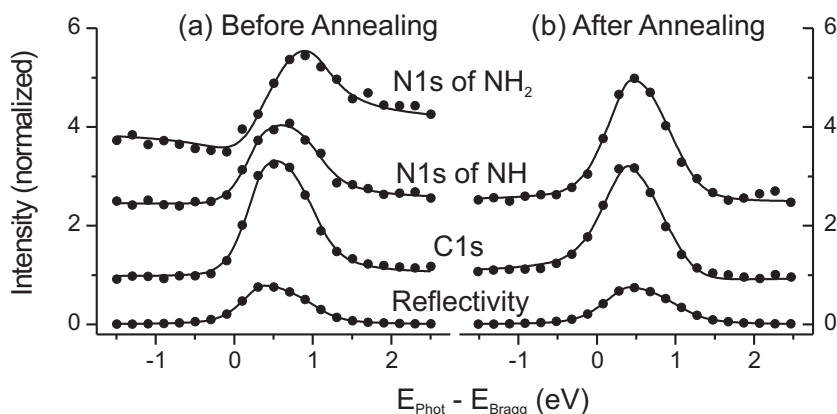
In order to gain insight into the molecule substrate interaction, XSW was used to study the adsorption height of DPDI/Cu(111) for the mobile phase as well as the adsorption height of dehydro-DPDI/Cu(111) for the porous network. In Section 2.1 the XSW technique is introduced and relevant aspects of the data analysis of the system at hand are discussed. Thus, this section concentrates on the results and their interpretation.

Figure 5.2 exemplarily shows both the reflectivity of the (111)-plane of Cu(111) and photoelectron yield curves for the different chemical species of DPDI and dehydro-DPDI whose fits yield coherent fractions and positions. It is noted that the coherent position represents the adsorption height modulo the distance between two Bragg planes.<sup>1</sup> This was considered when calculating the adsorption heights that are summarized in Table 5.1. These heights are visualized in molecular sketches in Figure 5.3.

In the mobile phase the C-atoms of DPDI (perylene core) exhibit a height of  $2.68 \text{ \AA}$ . This value agrees well to the height of the C-atoms of the perylene derivative

<sup>1</sup>Here (111)-planes of Cu, so the distance amounts to  $2.09 \text{ \AA}$ .





**Figure 5.2:** Photoelectron yield curves for the different chemical species of DPDI (a) and dehydro-DPDI (b) as well as reflectivity of the Cu(111) crystal before (mobile phase) and after annealing (porous network). Each black dot represents the peak intensity of a core-level spectrum (N1s or C1s) that was recorded at a different photon energy (the x-axis). The fits (black lines) of the photoelectron yield curves provide the coherent fraction and position whereas the fit of the reflectivity delivers the parameters that are needed to fit the photoelectron yield curves. The photoelectron yield curves of both N1s peaks before annealing were related to the amine and imine nitrogen species according to [36].

perylene tetracarboxylic dianhydride (PTCDA) on Cu(111) that was determined to 2.66 Å [102]. PTCDA is reported to interact strongly with the substrate [103]. In comparison to the perylene core the amine ( $-\text{NH}_2$ ) nitrogen (2.20 Å) as well as the imine ( $-\text{NH}$ ) one (2.4 Å) are bent down indicating an attractive interaction with the surface. The noticeable difference between the coherent fractions of the amine and imine nitrogens may be related to the fitting strategy that was used to discriminate between both species (Appendix C.1).

The different heights of the end groups compared to the average height of the perylene core indicate a bent molecule (Appendix C.1). This effect was observed and discussed for PTCDA on Ag(111) and Cu(111) [102, 104–106] as well as for other molecular adsorbates [42, 107, 108]. However, in particular in comparison to PTCDA the bending of DPDI is quite strong.

The height of the perylene core as well as the heights of the N-atoms indicate strong molecule-substrate interactions. This interpretation supports a “high” *desorption barrier* which is needed to prevent the desorption of DPDI during the annealing process. However, this interpretation is not thought to contradict a “low” *diffusion barrier* which is expected as the molecules are mobile [109].

After the formation of the porous network the imine nitrogens are lifted towards the perylene core. This lifting can be explained by the (intermolecular) H-bonds which evolve upon network formation. An analogous effect was observed for the formation of the herringbone structure of PTCDA/Ag(111) in which the oxygen atoms were lifted towards the perylene core to enable the formation of H-bonds. [110] The coherent

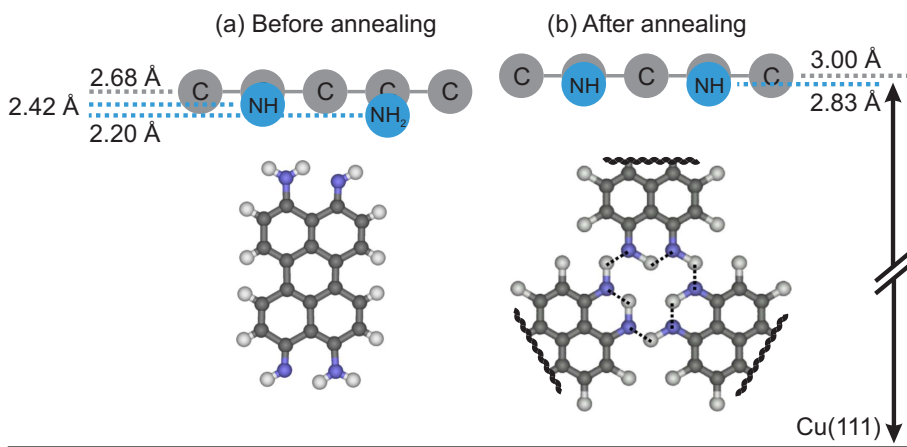


**Figure 5.3:** Graphical illustration of the XSW results showing the adsorption heights of the different chemical species (carbon, nitrogen of the amine (NH<sub>2</sub>) and imine (NH) group) of DPDI in the mobile phase before annealing (a) and dehydro-DPDI in the porous network after annealing (b).

fraction of the C atoms that was determined to 0.46 appears low, especially for a highly ordered structure. However, it agrees well with coherent fractions reported for the C-atoms of PTCDA on Cu(111) (0.48) and Ag(111) (0.52) [102].

The most puzzling result is the lifting of the whole molecule by approximately 0.3 Å after annealing. The height of the perylene core of 3.00 Å, which is comparable to the sum of the vdW radii of copper (1.4 Å) and carbon (1.7 Å), does not indicate a significant interaction between the perylene core and the substrate. This seems to contradict the initial working hypothesis of a strong molecule-substrate interaction as an explanation of the stability of the network. This issue is addressed in the following sections.

### 5.1.2 The valence bands

The detailed picture of the adsorption of PTCDA on various metal substrates that we can access nowadays is based on extensive studies using complementary surface science techniques. In [103], in which XSW and UPS studies of PTCDA on Au(111), Ag(111) and Cu(111) are summarized, an increasing molecule-substrate interaction can be associated with the formation of hybridized states between molecular orbitals and the valence band of the substrate. Such hybridized states were identified with UPS for PTCDA adsorbed on Ag and Cu as partially or completely filled LUMOs. This was interpreted as an electron transfer from the substrate to the molecules. Such a fingerprint of a strong molecule-substrate interaction is missing in the case of PTCDA/Au(111) which interacts weakly with the substrate. For PTCDA/Ag(111) the strong molecule-substrate interaction is mainly induced by the perylene core [111]. Further studies extended this view and considered the oxygen atoms of PTCDA which were reported to enhance the bonding to the Ag substrate [112]. Furthermore, the

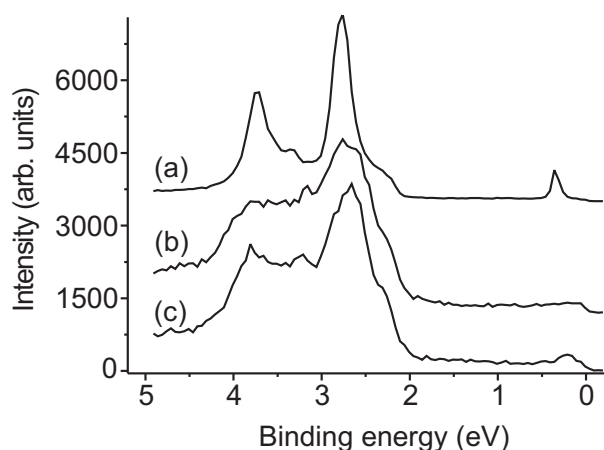


**Figure 5.4:** Normal emission spectra of the valence band of clean Cu(111) (a), 0.73 ML of DPDI before (b) and after annealing (c). The spectrum of clean Cu(111) was scaled by a factor of 0.35. The data were taken at room temperature at the COPHEE end-station (Swiss Light Source).

filling of the LUMO may promote additional bonds of the carboxylic oxygens to the Ag surface. [104–106]

It is noted that a (partial) filling of the molecular LUMO does not necessarily imply an electron transfer *from the substrate* to the molecule. For the porous surface coordination network of TAPP on Cu(111) (see Section 4.1) theoretical studies carried out in the group of Prof. Persson indicate an electron transfer *from the Cu-adatoms* to the molecular LUMO – a sort of “adatom-mediated chemisorption”.

Electron transfer from the substrate to the molecular LUMO is also reported for other organic adsorbates that interact strongly with the substrate like naphthalene-tetracarboxylic dianhydride (NTCDA) on Ag(111) [113], C<sub>60</sub>/Cu(111) [114] or tetra-fluoro-tetracyanoquinodimethane (F4-TCNQ) on Cu(111) [107]. Also in these cases, detailed measurements on the valence bands together with theoretical studies reveal complex electronic structures at the molecule-metal interface. For C<sub>60</sub>/Cu(111) an interface state is observed whose dispersion follows the periodicity of the molecular superstructure [35]. In the case of F4-TCNQ/Cu(111) the molecule-substrate interaction is based on a complex interplay between a metal-to-molecule electron transfer and a back transfer which deep-lying molecular orbitals are involved in [107].

Despite their complex structures at the molecule-metal interface, these strongly interacting systems have a significant (and detectable) influence on the valence bands in common. Thus the valence band structure of DPDI/Cu(111) was studied by ARPES in order to gain further insight into the molecular adsorption. In normal emission spectra of clean Cu(111) (Fig. 5.4.a) the surface state is observed at approximately 0.4 eV. However, it is suppressed in the spectrum of the mobile phase (Fig. 5.4.b). Coverage dependent studies reveal that the binding energy of the surface state measured at normal emission shifts towards the Fermi energy with increasing coverage of DPDI. Such an influence on the surface state induced by statistically distributed

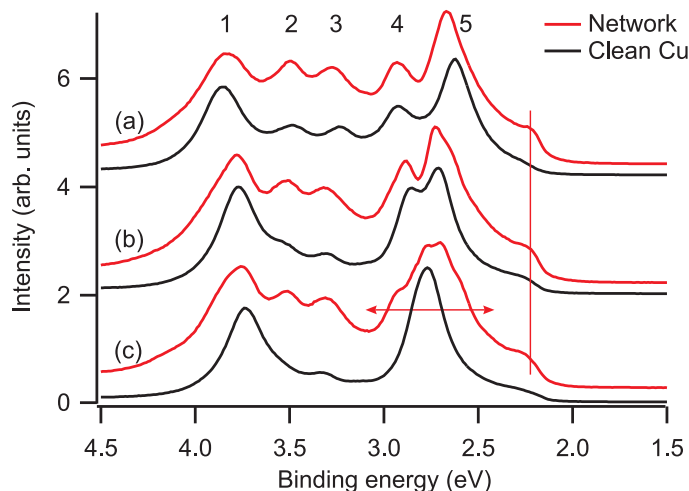


**Figure 5.5:** The d-bands of “pure” Cu(111) recorded at RT (black) as well as the d-bands of Cu(111) covered by the porous dehydro-DPDI network recorded at 7 K (red). The measurements were carried out at the CASSIOPEE end-station (Soleil). In order to gain information on the dispersion of the d-bands, spectra are shown for different emission angles (measured with respect to normal emission):  $10^\circ$  (a),  $5^\circ$  (b), normal emission (c). The angle-integration performed for each spectrum corresponds to an opening of the analyzer of  $0.6^\circ$ . The spectra of clean Cu are scaled by a factor of 0.6 to facilitate comparison. The whole dispersion is shown in Appendix C.2.

adsorbates is observed e.g. for Xe/Au(111) [115] and Na/Au(111) [116]. Besides this effect on the surface state, the spectrum does not exhibit any features at binding energies less than 2 eV that could be related to (hybridized) molecular orbitals. These observations basically hold true for the spectrum of the porous network (Fig. 5.4.c). The broad peak (binding energy of approximately 0.2 eV) that is observed close to the Fermi energy is related to the surface state and is discussed in Section 5.2 in detail.

The non-detection of a peak does not strictly imply its non-existence. In this case, measurements at grazing emission, which are commonly used to enhance surface sensitivity, could further elucidate this issue. However, STS studies on dehydro-DPDI (see Fig. 5.11 on page 76) agree well to the results of the normal emission spectrum as they do not exhibit a feature in the immediate vicinity below the Fermi energy. Instead, the first feature that could be related to a molecular state, e.g. to the LUMO, is observed at 70 mV above the Fermi energy (cf. Section 5.2.3 on page 76).

For both the mobile phase and the porous network a change of the Cu d-bands (binding energies between 2 eV and 4.5 eV) in comparison to pure Cu is observed. In order to gain more information on this change ARPES measurements were performed on the d-bands (Fig. 5.5). Copper exhibits a filled 3d-shell with five d-bands (labeled from 1-5 in Fig. 5.5). The d-bands 1 & 2 and 4 & 5 are observed to be degenerated at the  $\bar{\Gamma}$ -point (normal emission spectrum of clean Cu (black curve) in Fig. 5.5.c) for the photon energy of 21.22 eV [117]. However, as they disperse differently along the  $\bar{\Gamma K}$ -direction the degeneracy is removed and band splitting is observed for emission

angles that differ by  $5^\circ$  (Fig. 5.5.b) and  $10^\circ$  (Fig. 5.5.a) from normal emission. At the latter angle the five d-bands can be identified as separated peaks.

For the porous network, the degeneracy at normal emission is observed to be removed at least for the first three d-bands (1-3) (red spectrum in Fig. 5.5.c). At an emission angle of  $10^\circ$  the energies of the d-bands in both spectra (black and red spectrum in Fig. 5.5.a) match quite well. For the fourth and fifth d-band the interpretation is not straightforward. The broad feature at normal emission (highlighted by the red arrow in Fig. 5.5.c) seems to consist of at least four peaks (two peaks and one shoulder at each side). These additional peaks may be related to molecular orbitals. The shoulder visible in the valence band spectra of the porous network (highlighted by the red vertical line) may be at first glance assigned as a molecular orbital. However, it coincides quite well with the shoulder of the Cu spectra. Since the difference in intensity is to a large extent due to the scaling of the Cu spectra (factor of 0.6) the identification of the shoulder of the porous network with the one for “pure” Cu seems reasonable.

In summary, no indications for a hybridization of molecular orbitals with the valence band of the substrate is found in the energy window between the Fermi energy and 2 eV. Especially the widely reported electron transfer to the former molecular LUMO was not observed. However, a hybridization with deep-lying molecular orbitals cannot be excluded and the removal of degeneracy of the Cu d-bands as well as the features around 2.7 eV (Fig. 5.5.c) show an influence on the valence band of the substrate by the porous network.

### 5.1.3 Discussion

Due to the missing indications for a (partially) filled LUMO and in particular due to the height of the perylene core of  $3 \text{ \AA}$  above the Cu(111) surface, which exceeds the height of the perylene core of PTCDA/Cu(111) by  $0.34 \text{ \AA}$ , the molecule-substrate interaction is not thought to be based on an electron transfer from the substrate to the molecular LUMO. Moreover, it is concluded that the perylene core is not responsible for a strong interaction between the porous network and the surface.

However, the extraordinary stability of the network needs to be explained and it is still expected to be based on a stabilizing effect of the surface despite the counterintuitive results provided by XSW and ARPES. In this context it is noted that Kilian et al. [110] reported an XSW study of PTCDA/Ag(111) where the transition from an unordered to an ordered assembly is studied. On the one hand an effect for the end groups was observed in analogy to our results (see Section 5.1.1). On the other hand, the height of the perylene core of PTCDA increased by only  $0.06 \text{ \AA}$  which is small compared to the increase of height of  $0.32 \text{ \AA}$  we measured for DPDI. In contrast to PTCDA, the transition from the mobile DPDI phase to the porous network goes along with a dehydrogenation of DPDI. However, if the increase of height of  $0.32 \text{ \AA}$  is not exclusively related to the (chemical) difference between dehydro-DPDI and DPDI it indicates a further mechanism which is involved in the formation of the porous network. It is assumed that the increase of height allows for the space that is necessary for Cu-adatoms between substrate and molecular ad-layer. These Cu-adatoms

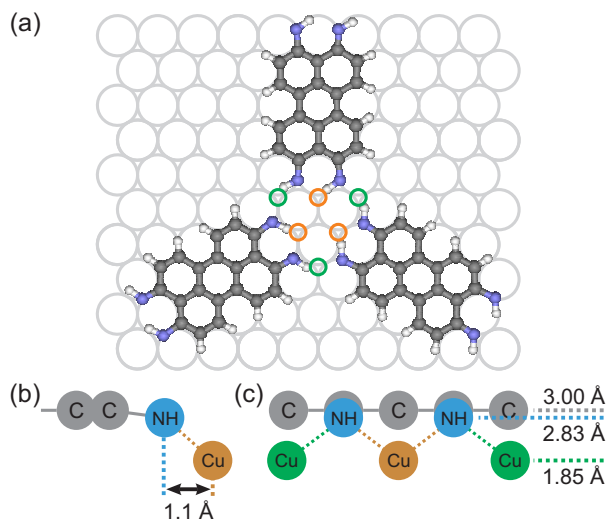


**Figure 5.6:** Suggested model for the porous dehydro-DPDI network that is additionally stabilized by interactions with Cu-adatoms. a) The topview shows the positions of dehydro-DPDI in the unit cell of the porous network. The surface atoms are indicated by large gray circles. The Cu-adatoms (small green and orange circles) highlight two possible configurations for a Cu-coordination. The lateral position of the unit cell with respect to the substrate is arbitrarily chosen. However, this choice results in equivalent adsorption sites of all end groups. [36] b–c) Side view of molecule and adatoms. The distance in (b) is estimated from the geometry in (a). The height of the Cu-adatoms in (c) of 1.85 Å corresponds to the height of free adatoms on Cu(111) [118]. The side views illustrate that the Cu coordination does not interfere with the formation of H-bonds. If the Cu-adatoms are assumed to adsorb at hollow fcc or hcp sites the N-Cu distance calculated from the proposed geometry amounts to approximately 2 Å.

could interact with the nitrogens thus providing an indirect coupling of the molecular ad-layer with the substrate. It is noted that this interaction is thought to occur in addition to the formation of H-bonds.

In Figure 5.6 two possible configurations on the Cu surface are depicted for the adatoms (green and orange). The adatoms are thought to adsorb at the preferred hollow sites [119]. Due to equivalent symmetries of the porous network and the Cu substrate<sup>2</sup>, all adatoms within a crossing either adsorb on hollow fcc sites or hcp sites.<sup>3</sup> For the configuration marked green each adatom binds to two dehydro-DPDI. However, another configuration (orange) is thought to be possible in which each dehydro-DPDI interacts with a separate adatom of an “adatom trimer”. In the latter case the intermolecular stability is enhanced by the interaction between the adatoms. It

<sup>2</sup>The porous network adsorbs in a p(10x10) superstructure. Its basis consists of 3 molecules that are rotated by 120° with respect to each other. [36]

<sup>3</sup>If the adatoms in one crossing adsorb at fcc sites the adatoms in the neighboring crossings adsorb at hcp sites. However, the difference in adsorption energies between hcp and the actually preferred fcc hollow site for a single Cu-adatom or an adatom dimer on Cu(111) is reported to be only 6 meV or 21 meV, respectively [119].

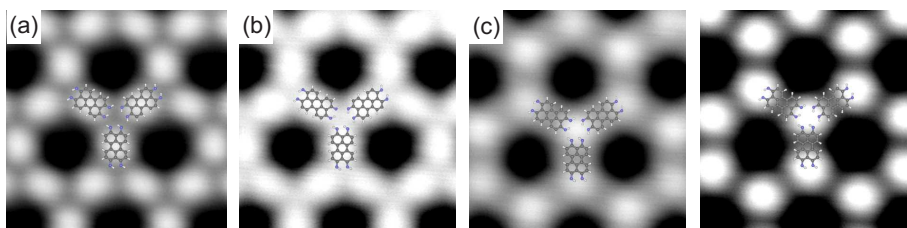


**Figure 5.7:** Series of STM images ( $5 \times 5 \text{ nm}^2$ , 10 pA) of the porous network taken at 5 K at the same position, but at different sample voltages: 1.5 V (a), 2.3 V (b), 2.9 V (c), 3.4 V (d). The molecular model is superimposed to illustrate equivalent positions. In analogy to the porous network of TAPP (see Section 4.1.2 on page 45) the crossing between the molecule dominates the STM image at sample voltages around 3 V.

is noted that the molecular adsorption sites are arbitrarily chosen in Fig. 5.6. However, this choice underlines the symmetry between substrate and molecular ad-layer as it provides equivalent adsorption sites for all molecules, in particular for all imine groups [36]. An adatom height of  $1.85 \text{ \AA}$  was assumed which corresponds to the height of free adatoms on Cu(111) [118]. According to the geometry proposed in Figure 5.6 the overall N-Cu distance would amount to approximately  $2 \text{ \AA}$ . This distance could be elongated by shifting the adatoms towards the neighboring bridge adsorption sites. However, this would decrease the interatomic distances of the orange configuration and the expected energetic penalty would have to be compensated by an optimized N-Cu interaction.

Unfortunately, the experiments until now did not provide any direct evidence for such Cu-adatoms. In analogy to the previously discussed system TAPP/Cu(111) (Chapter 4), theoretical studies are thought to allow for new insights into the molecule-substrate interactions when compared to the existing experimental results: For DPDI on Cu(111) XPS shows that the imine N1s peak of the porous network is shifted by 320 meV with respect to the imine N1s peak of the mobile phase [36]. This could be due to interactions with Cu-adatoms. This assumption could be verified by calculations of the chemical shift (cf. Section 4.1.2). Despite the missing direct evidence for the Cu-adatoms, an STM study (Fig. 5.7) at least indirectly supports the proposed model. In analogy to TAPP/Cu(111) (see Section 4.1.2), the same area of the porous network was imaged at different sample voltages. Like in the case of TAPP the transition to a sample voltage around 3 V resulted in a reversed contrast by which the crossing between three adjacent molecules appears as a bright protrusion dominating the STM image. This effect may also be related to unoccupied resonance states of Cu-adatoms on Cu(111) [83,84] as it is done in the case of the porous surface coordination network of TAPP (cf. Fig. 4.5 and 4.6 on page 47).

Hence, the interaction of dehydro-DPDI with Cu-adatoms is considered as a promising new working hypothesis that could explain the stability of the porous network as well as the counterintuitive XSW results. Moreover the verification of this model would support the outstanding relevance of the N-Cu interaction for the surface chemistry of the perylene derivatives TAPP and DPDI.

## 5.2 Band formation from coupled quantum wells

The results discussed in this section are published in [120].

The electronic and optical properties of crystalline solids exhibit properties which derive to a large extent from the periodic arrangement and interactions of their component quantum systems, such as atoms or molecules. Extending the principle of such periodic coupling beyond the molecular regime has given rise to metamaterials, which are composed of regularly repeated units, in most cases, nanoparticles [121,122]. Quantum effects that arise from confinement of electronic states have been extensively studied for surface states of noble metals which are characterized by a quasi two-dimensional (2D) electron gas. These may be visualized by scanning tunneling microscopy (STM) as standing wave patterns arising from scattering at steps and defects [46,47] or at large organic molecules [123]. Examples of such surface state confinement comprise thin films [124], artificial nanoscale structures [125,126], vacancy and ad-atom islands [127,128], self-assembled one-dimensional (1D) chains [129,130] and vicinal surfaces [131,132].

In spite of these previous examples, periodic quantum confinement in 2D at surfaces has always been elusive, mainly because of the difficulties encountered in the production of strictly regular nanopatterned structures that can trap electronic states. We note though that Collier, et al. observed coupling phenomena between quantum dots at a solid/liquid interface, namely between colloidal particles arranged in a Langmuir monolayer [133]. The design of such structures is more readily achieved using molecules as building blocks than atomic units, given the fundamental dimensions of these arrays. Potential candidates for molecular systems which might exhibit this zero-dimensional periodic electronic confinement are porous molecular surface networks. Their production is based on molecular self-assembly, which makes use of concepts established in supramolecular chemistry, and has the advantage that identical parts are produced at once. This is in contrast, for instance, to assembly based on atom-by-atom positioning techniques [125,126].

In this section it is reported on the interplay of the surface state electrons of Cu(111) with the porous network of dehydro-DPDI that leads to the formation of a 2D electronic band structure through the coupling of confined electronic states. Each pore of the network confines the surface state of the Cu substrate in what can be described as a quantum dot.

### 5.2.1 STS: Confinement of the surface state

STS was used to probe the (electronic) density of states (DOS). Spectra recorded inside a pore display a peak at -0.22 V that is not seen on the bare metal (Fig 5.8.a). Given the previous observations of discrete states in 2D nanostructures [47,126–128], this peak is assigned to the confinement of the surface state electrons inside the pore. The confinement of this discrete state is demonstrated by recording simultaneously topography (Fig. 5.8.b) and  $dI/dV$ -signal (Fig. 5.8.c) at the peak energy, the latter showing *in first order* the local distribution of this state. Because each pore features a confined state, it can be considered as a single quantum dot that confines electrons



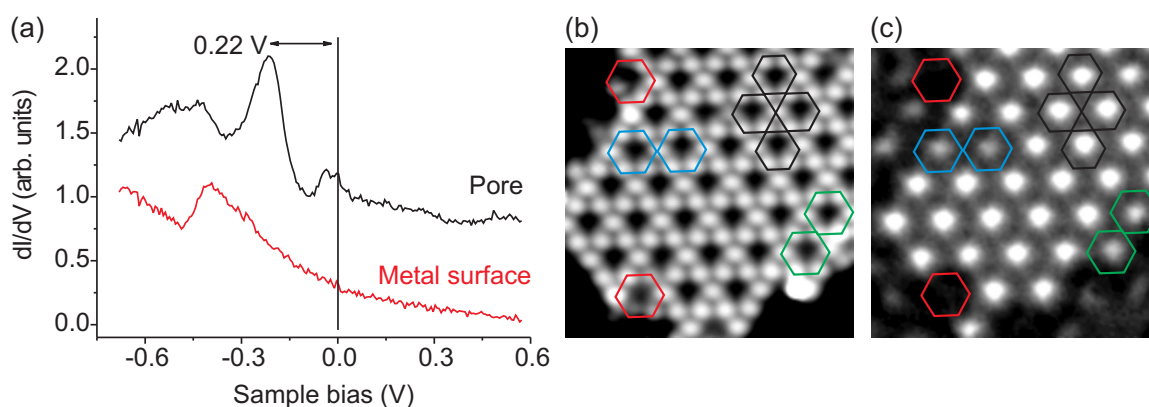


**Figure 5.8:** Study of the electronic confinement of the surface state within the pores of the network. a) STS spectra obtained at 5 K on the clean Cu surface (red) and inside a pore of the dehydro-DPDI network (black). The latter spectrum exhibits a maximum at  $-0.22$  V which is attributed to a confined surface state (Lock-In: 6 mV (rms), 513 Hz, initial tip parameters:  $-0.8$  V, 80 pA). b) STM image of the porous network ( $13.6 \times 13.6$  nm<sup>2</sup>,  $-0.2$  V/70 pA) and (c) simultaneously recorded dI/dV map at 5 K (Lock-In: 8 mV (rms), 513 Hz). A confined electronic state is observed inside the molecular pores. The black hexagons highlight the molecular positions. Defective pores severely affect the confined state (red hexagons) although not every defect annihilates the confined state (green hexagons). In some cases the confined state is affected although topography does not indicate any defects (blue hexagons). These observations could be explained by irregularities of the substrate within the pore (e.g. trapped Cu-adatoms or holes).

in all three directions. The inherent periodicity of the molecular network generates a regular “quantum dot array”.

Jensen et al. [128] studied the lifetime of confined states in vacancy islands on Ag(111). In their study the dominating process limiting lifetime and thus characterizing the imperfect confinement is lossy scattering at the confining boundary; inelastic electron-electron and electron-phonon scattering are thought to be less important. Likewise, for the 2D periodic dehydro-DPDI network, which is commensurate with the Cu(111) substrate, the confined electronic states are expected to “leak” into neighboring pores. This leakage would electronically couple quantum wells of neighboring pores, and this coupling should be visible in the electronic structure of the system.

### 5.2.2 ARPES: The formation of an electronic band

The electronic structure of the “quantum dot array” was investigated with angle-resolved photoemission spectroscopy (ARPES). In Figure 5.9.a, ARPES normal emission spectra recorded at room temperature (RT) are shown for the clean Cu substrate and for the Cu substrate covered by different amounts of the dehydro-DPDI network. For the extreme cases (the clean Cu substrate and the highest molecular coverage)

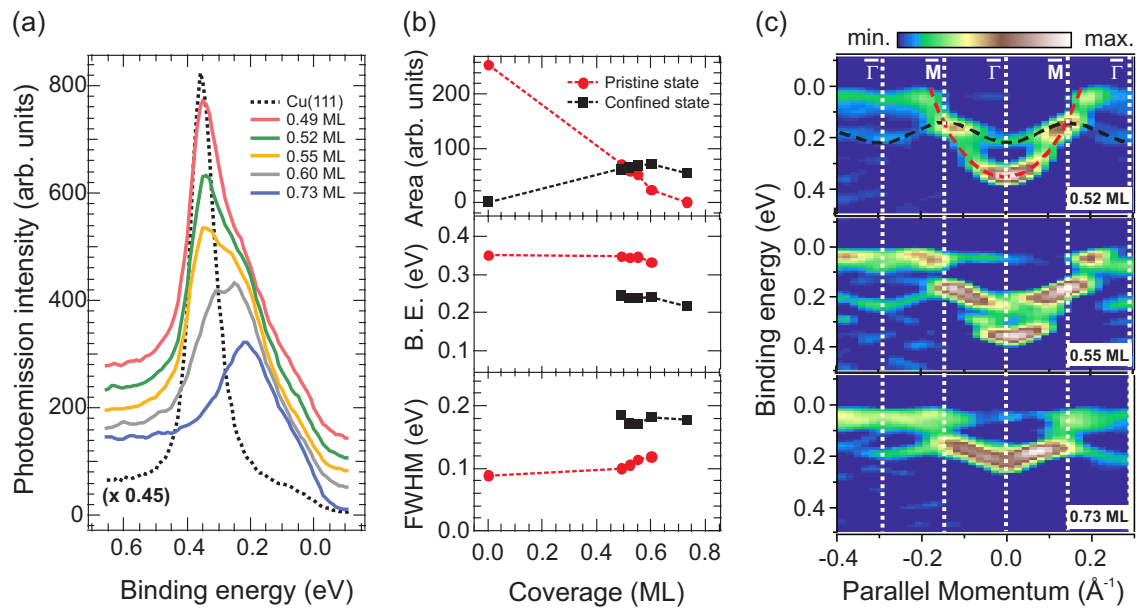


**Figure 5.9:** Band dispersion resulting from the periodic influence of the porous network on the surface state studied with ARPES for different molecular coverages. The measurements were performed at the COPHEE end-station (SLS). a) Normal emission spectra at RT showing the emerging confined state which progressively replaces the original Cu(111) surface state (scaled, black dotted line) with increasing molecular coverage. b) Peak area, binding energy (B.E.) and full width at half maximum (FWHM) resulting from the analysis of the pristine and the confined states presented in (a). c) Energy dispersion curves (EDC) of the pristine state (red dashed line) and the confined state (black dashed line) measured along the  $\bar{\Gamma}\bar{M}$  high symmetry direction and visualized as the 2<sup>nd</sup> derivative of the photoemission intensity for three different coverages. The 2<sup>nd</sup> derivative was used to enhance features of the EDC. Both EDCs at 0.52 ML and 0.73 ML have been acquired at RT, whereas 60 K was the acquisition temperature for 0.55 ML. The vertical white dotted lines refer to the new symmetry points induced by the molecular network. The red and black dashed lines on the top graph indicate the averaged positions of the maxima of both Lorentzian components fitted for all EDCs.

the spectra display a single component line shape, whereas all the other spectra exhibit a double-peak line shape. A detailed analysis of the spectra (fitted by using two Lorentzian components together with a constant background and multiplied by a Fermi-Dirac distribution) shows that the double peak consists of the components observed for the extreme cases, while only their relative intensities vary depending on the network coverage (Fig. 5.9.b). The component marked red is attributed to the clean surface state and maintains its binding energy and width throughout the molecular coverage range, but its intensity decreases as the molecular network coverage increases. It will be referred to below as the “pristine state”. The component marked black, however, is related to the influence of the molecular network and increases with

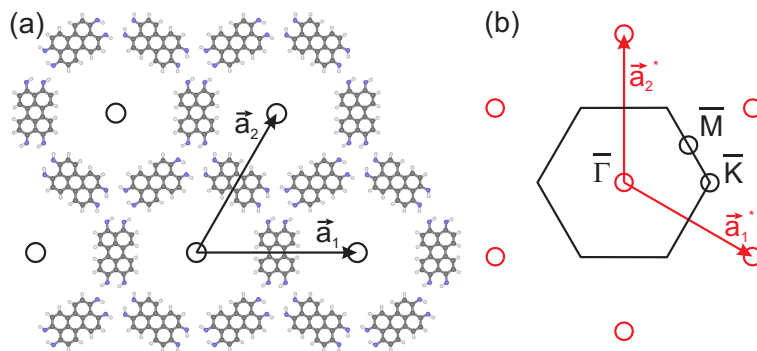


**Figure 5.10:** The surface Brillouin zone (SBZ) of the DPDI network. a) The unit cell of the DPDI network with its p(10x10) structure. The lengths of the unit-cell vectors:  $|\vec{a}_1| = |\vec{a}_2| \equiv a \approx 2.56$  nm. b) The unit cell in reciprocal space with the first Brillouin zone (black hexagon) and the critical points  $\bar{\Gamma}$ ,  $\bar{M}$  and  $\bar{K}$ . The lengths of the unit-cell vectors amount to  $|\vec{a}_1^*| = |\vec{a}_2^*| = 4\pi/\sqrt{3}a \approx 0.283$   $\text{\AA}^{-1}$ . The distances between the critical points are  $2\pi/\sqrt{3}a \approx 0.142$   $\text{\AA}^{-1}$  ( $\bar{\Gamma}\bar{M}$ ) and  $4\pi/3a \approx 0.164$   $\text{\AA}^{-1}$  ( $\bar{\Gamma}\bar{K}$ ).

increasing coverage. In analogy to the pristine case, it has a constant width and a constant binding energy. Its value of  $0.23 \pm 0.03$  eV is in very good agreement to the STS spectrum shown in Fig. 5.8.a. Because its binding energy and peak width are independent of the surface coverage, its origin can be attributed to a single pore with its surrounding molecular border while the overall island size shows no influence. This component will be referred to below as the “confined state”.

Isolated nanocavities exhibit discrete electronic states, but the periodic influence of the porous network on the 2D free electron gas of the surface state, along with the imperfection of its confinement, is expected to induce an electronic band in analogy to the band structure of a solid created by the periodic potential of its atoms. The existence of such cooperative behavior can be investigated by studying with ARPES the electronic structure of both the pristine Cu(111) surface state and the confined state as a function of the surface parallel momentum. The ARPES data displayed in Fig. 5.9.c exhibit for both states dispersive bands. One band (highlighted in red) follows the characteristic parabolic dispersion of the Cu surface state [64], whereas the second band (highlighted in black) is related to the periodic potential of the porous network. This interpretation is supported by the periodic continuation of the band within Brillouin zones of higher order that possess the same periodicity as the molecular network (10 times smaller than the substrate). This periodicity is indicated by white lines in Figure 5.9.c, which are separated by  $|k_{\text{parallel}}| = 0.142$   $\text{\AA}^{-1}$  (Fig. 5.10). Furthermore, weak photoemission intensity very near the Fermi energy and around the  $\bar{M}$  symmetry points can also be observed in Figure 5.9.c, especially for the case of 0.55 monolayer (ML) which was acquired at 60 K<sup>4</sup>. This intensity may be attributed to the existence of the 2<sup>nd</sup> subband which has its lowest binding energy at approximately

<sup>4</sup>New measurements with high resolution carried out at the CASSIOPEE end-station (Soleil) using synchrotron radiation confirm these findings with better quality (data not shown here).

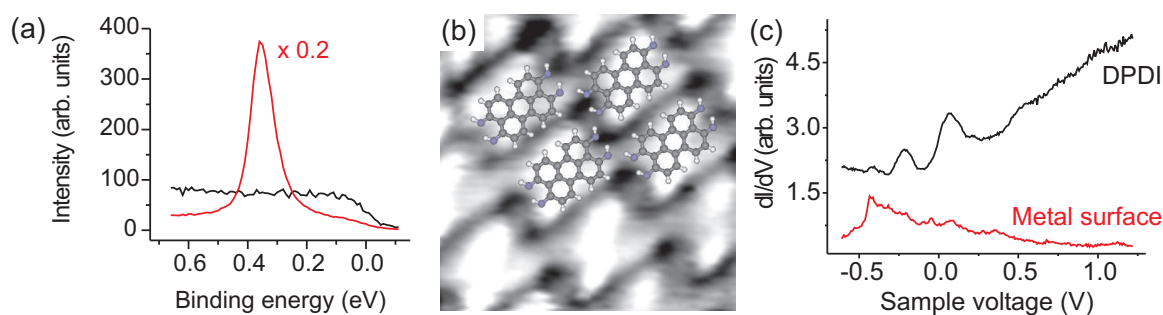


**Figure 5.11:** a) Normal emission spectra of pristine Cu (red) and a close-packed assembly of dehydro-DPDI (1 ML) (black) near the Fermi energy. The latter spectrum does not reveal any feature that can be related to the surface state. b) STM image for 1 ML of dehydro-DPDI on Cu(111) annealed at 500 K ( $3.5 \times 3.5 \text{ nm}^2$ ,  $-0.9 \text{ V}/84 \text{ pA}$ ). c) STS of the pristine Cu surface (red) and on top of dehydro-DPDI of the porous network (black). Lock-In: 7 mV (rms), 313 Hz, initial tip parameters:  $-0.8 \text{ V}$ , 90 pA.

60 meV. Thus, the energy gap between the subbands originating from the confined network is roughly 90 meV.

### 5.2.3 A strong confinement

The rather shallow dispersing band (bandwidth of approximately 80 meV) is an indication for the strong confinement of the surface state inside the pores. Further evidence for our interpretation stems from both STS measurements performed on top of dehydro-DPDI molecules (Fig. 5.11.d) and photoemission spectra. Both methods were used to gain information on the “direct influence” of dehydro-DPDI on the surface state.

The ARPES studies of the porous network (Fig. 5.9) show the result of a periodic perturbation on the surface state induced by the porous network and thus the combined influence of “molecules and pores” on the surface state. In order to “isolate” the molecular influence a sample fully covered by a close-packed structure of dehydro-DPDI was prepared (Fig. 5.11.c) [37] which is formed by the same building blocks and expected to be based on the same intermolecular interactions as the porous network. For this non-porous organic structure, no evidence of the surface state is found in the normal emission spectrum depicted in Figure 5.11.a.

STS has proven to be able to detect shifts of the surface state induced by molecules: In the case of PTCDA Nicoara et al. [134] could determine a small shift induced by the weakly bound molecules (physisorbed, according to [103]) when deposited on Au(111). The same molecules are strongly bound (chemisorbed, according to [103, 111]) when deposited on Ag(111) and in the corresponding STS spectra a characteristic feature is observed which resembles the surface state. This feature was initially interpreted as a dispersing state deriving from the LUMO+1 of the free PTCDA [135] and later as the upshifted Shockley state of Ag(111) [136].

The black spectrum in Figure 5.11.d was recorded on top of dehydro-DPDI of the porous network. The weak peak at -0.21 V matches the peak of the confined state (Fig. 5.8). It may be attributed to the (bad) resolution of the tip that still detects features from within the pore or to the wave function that penetrates the (finite) molecular barrier. At first glance, the second peak at 70 mV above the Fermi energy may be related to a molecular feature, e.g. the molecular LUMO, as it is not reproduced within the pores (Fig. 5.8). However, its onset coincides with the weak intensity in the ARPES measurements at the  $\overline{M}$  symmetry points (Fig. 5.9) that was tentatively attributed to the 2<sup>nd</sup> subband in the preceding section (cf. Appendix C.3). Noticeably, the onset of the surface state could not be observed. The missing onset does not necessarily imply the non-existence of the surface state. However, the preceding examples which show that STS can detect shifts of the surface state induced by molecules, together with the photoemission data support the interpretation of a strong influence of dehydro-DPDI on the surface state on Cu(111). Thus, the porous network is thought to act as a strong perturbation (and not as a weak modulation) of the surface state resulting in a shallow dispersing electronic band.

### 5.2.4 Summary

These results provide experimental evidence of periodic 2D confinement by a porous molecular network, which can be regarded as a regular array of quantum dots. A notable consequence of such periodic influence on the otherwise free-electron-like surface state is the formation of an artificial electronic band structure. The established and prospective possibilities to control the structures of porous networks, together with the characteristic degree of coupling between ad-molecules and the surface state, will allow the fabrication of related systems with different band structures resulting in “2D electronic metamaterials” in analogy to the well-established optical metamaterials [137, 138].

The geometry of the porous dehydro-DPDI network is a “real stroke of luck” for the study with ARPES. Its long-range order basically made it accessible to a lateral-averaging technique like ARPES. However, the study of the band structure in well-defined directions in reciprocal space (here:  $\overline{\Gamma M}$ ) was only possible because the dehydro-DPDI network consists of only *one* rotational domain.

## 5.3 Comments on the lateral confinement of the surface state within pores

This section deals with the aspect of lateral confinement of the surface state within molecular pores and comments on the picture of a “particle in a box”. Although this model is not an appropriate description of the periodic perturbation of the surface state induced by the DPDI network it is used here to allow for a comparison to the confinement of the surface state in Ag islands [127].

The concept of a “particle in a box” was already used in the first publications that reported on the confinement of the surface state. Crommie et al. [125] explained the

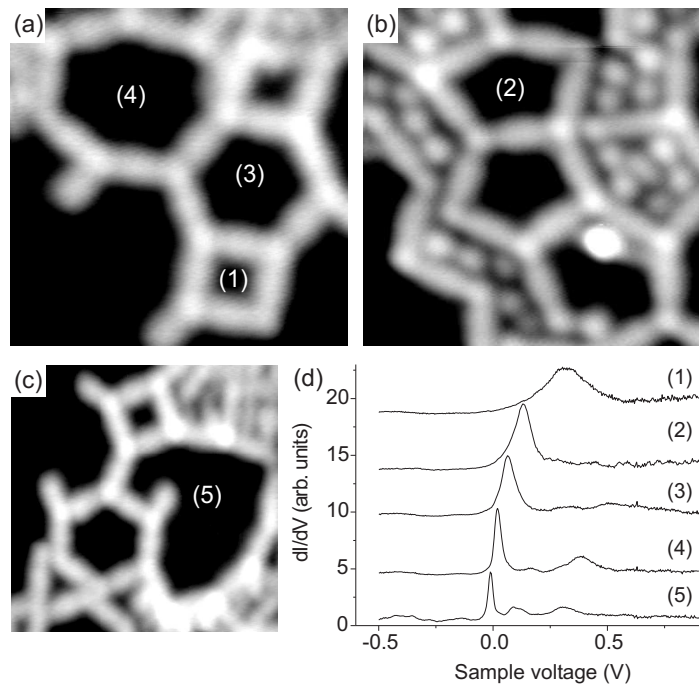


**Figure 5.12:** Confinement of the surface state in pores of different size and geometry formed by DIBOTAP and TMA (see Section 4.2.2). The STM and STS experiments were performed at 5 K. a)  $8.8 \times 8.8 \text{ nm}^2$ ,  $-0.5 \text{ V}/20 \text{ pA}$ . b)  $8 \times 8 \text{ nm}^2$ ,  $-0.5 \text{ V}/20 \text{ pA}$ . c)  $10.5 \times 10.5 \text{ nm}^2$ ,  $-0.5 \text{ V}/20 \text{ pA}$ . d) The spectra recorded in the center of the pores illustrate the dependency of the peak position on the pore size. Each spectrum can be assigned via the number on its right to the corresponding pore in the STM images.

discrete states measured within a circular quantum corral by calculating the eigenenergies for a circular confinement with boundaries of infinite height. Li et al. [127] extended this idea when studying the surface state that was confined within hexagonal islands on Ag(111). They showed as well that the experimentally determined discrete energies can be described by assuming confinement in hexagons with boundaries of infinite height. Moreover, this description included a proportionality between the eigenenergies and the reciprocal of the area of the hexagons. Hence, these results were strong indications for a lateral confinement of the surface state.

The comparison of the eigenenergies of quantum corrals of different size is not applicable to the dehydro-DPDI network with one pore size. However, the combination of DIBOTAP and TMA on Ag(111) resulted in pores of different size and geometry (see section 4.2.2 on page 59). With STS the electronic structure of the different pores was investigated. The experimental results show that the peak positions depend on the pore size (Fig. 5.12). In a more detailed quantitative analysis (Fig. 5.13) the peak positions of the different pores, which will be called “eigenenergies (of the ground state)”, are plotted against the reciprocal of the pore area. The diagram exhibits a direct dependence of the peak energy on the pore area, but the peak energy seems to be independent of the pore geometry. This finding can be explained in the following

way. The eigenenergies of the ground state for confinement in polygons of the same area with infinitely high barriers are observed to decrease when the number of sides is increased [139]. The difference between the eigenenergy of the ground state of a square and a circle (infinite number of sides) of the same area is only 9% and thus, is for our case within the error of the measurements (see Appendix C.4).

The determination of the pore area is not straightforward. Besides the impossibility to determine with STM a structure’s size with 100 % accuracy, the confining boundary needs to be determined appropriately [123, 127]. In our case the left hand side of the error bars (Fig. 5.13.b) represents the theoretically maximum pore size which is defined by the perimeter through the centers of the molecules (inset of Fig. 5.13.b). The right hand side of the error bars represents the minimum pore size which is defined by the dimension of the molecular vdW area. The latter area is derived from the maximum pore area by subtracting the product of the pore perimeter and the half width of the molecular vdW surface (half width here: 4.5 Å). For the determination of the values represented by the black squares scattering at the carbon atoms of the perylene backbone, which are closest to the inner pore edge, is assumed. Therefore, the maximum pore area is reduced by the product of the pore perimeter and the half width of the perylene core (hydrogen atoms are not taken into account, i.e. the carbon-carbon distance is used, half width here: 2.4 Å). Thus, the light blue area, which highlights the range defined by the error bars, is expected to cover the values of the areas that are relevant for the “real physical” confinement. However, the light blue area does not overlap with the red area, that covers the values expected from confinements within infinitely high barriers. The reason for this deviation that was not observed by Li et al. [127] may be the small pore sizes. If, for simplicity of the argumentation, a constant barrier height for the different pores is assumed, the eigenenergy of the ground state will approximate the barrier height when the pore size is decreased. Thus, the ground state of small pores will penetrate the barrier more strongly than the ground state of large pores. Hence, the wave function in the small pore is affected more strongly by the finite barrier height than the wave function in the large pore (see Appendix C.4).

The comparison to the confinement in the pores of the DPDI network shows that its ground state and its FWHM (red squares in Fig. 5.13) fit well into the scheme of the DIBOTAP-TMA system. This result, which is at first glance astonishing, is discussed in the following paragraphs.

The two different substrates, Ag(111) and Cu(111), exhibit nearly identical dispersions of the surface state, i.e. the reduced masses are comparable:  $m^* = 0.397 \cdot m_e$  for Ag(111) and  $m^* = 0.412 \cdot m_e$  for Cu(111) [64]. The different onsets of the surface states (Ag(111) at -63 meV and Cu(111) at -443 meV [64]) are accounted for in Fig. 5.13 by referring the eigenenergies of the ground state to the onsets of the corresponding surface state. Thus, the eigenenergies of the ground state, referred to the onset of the surface state, are expected to be similar for “identical” confinements on both substrates (i.e. identical sizes, geometries and barrier heights).

In contrast to the isolated confinements of the DIBOTAP-TMA system the DPDI network influences the surface state periodically. Moreover, the molecule substrate interactions for both systems are expected to be different. Unless both differences just

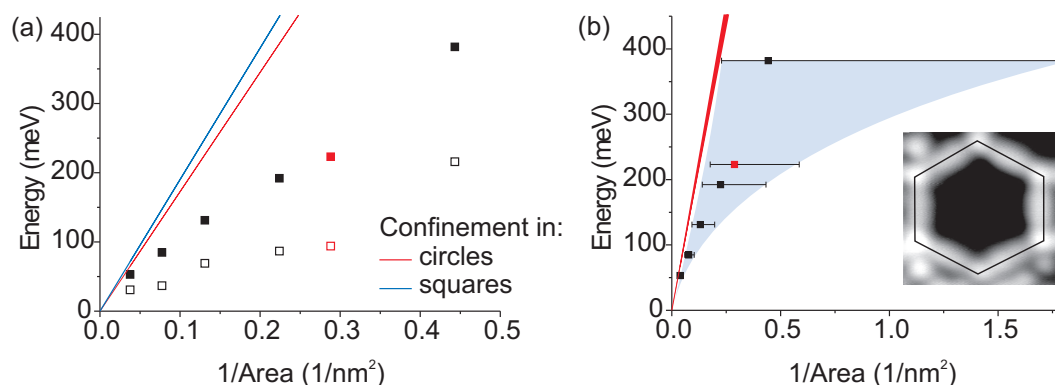


**Figure 5.13:** a) The peak position (filled black squares) and the FWHM (hollow black squares) with respect to the reciprocal of the area of the pore for the five different pores in Fig. 5.12. The red (blue) straight line shows the calculated confinement within infinitely high barriers in a circular (square) domain. b) The determination of the area of the pore in detail. Left boundary of the error bar: The center of the molecules determine the pore size (exemplarily highlighted by the black hexagon in the inset,  $4.3 \times 4.3 \text{ nm}^2$ ,  $-0.5 \text{ V}/20 \text{ pA}$ ). The black squares: Scattering at the carbon atoms of the perylene backbone is assumed. Right boundary of the error bar: Scattering at the boundary defined by the vdW radius of the molecules is assumed. If the error bar is not visible it is smaller than the symbol size. The light blue area indicates the range that is covered by the error bars whereas the red area highlights the range covered by the confinement in the different geometries in (a). The red squares in (a) and (b) show the corresponding values for the confinement of the surface state in the DPDI network (Section 5.2). The energies in (a) and (b) are denoted with respect to the onset of the surface state.

neutralize each other, the strong influence on the surface state, which was discussed for the DPDI network in the preceding section, is thought to explain the comparable confinement indicated by Fig. 5.13. In the picture of coupled quantum dots a strong influence on the surface state is interpreted as a weak coupling between the pores. A consequence of this weak coupling is the rather weak dispersion of the electronic band of the DPDI system. At the same time a weak coupling, i.e. a low transmission between the confinement and its surrounding area, results in a confinement that is not strongly affected by the confinement within neighboring pores.

It is noted that the interpretation of a weak coupling does not imply a confinement within high barriers or even barriers of infinite height. Otherwise, it would contradict the preceding discussion in which the deviation from the confinement within barriers of infinite height is considered. As the transmission through a barrier depends on both the barrier height and its width a “low” but “broad” barrier would fulfill both requirements: The deviation from the theoretically expected confinement within barriers of infinite height and the comparability between isolated and coupled confinements.

In summary, the observed dependency between eigenenergy of the ground state and pore size strongly indicates a lateral confinement of the surface state within pores and



extends the studies of Li et al. [127] to smaller quantum wells with sizes down to 4 nm<sup>2</sup> (this value refers to the maximum pore size of the smallest pore in Fig. 5.13). Moreover, the comparison to the dehydro-DPDI network further corroborates the weak coupling between the pores. Besides, the purely qualitative comparison to quantum mechanics of square potentials and barriers in one dimension allows for a careful assumption of “low” but “broad” barriers that characterize both systems.



## 6 Conclusions and Outlook

In the work at hand phenomena on quite different levels were discussed: Conformational trans-cis inversion (Chapter 3) on the *intramolecular* level, thermally induced changes of *intermolecular* interactions (Chapter 4) and band formation (Chapter 5) on the *supramolecular* level.

“Cooperative behavior” may be seen as a property or function that is common to the elements of an interacting system in analogy to a Mexican wave showing cooperative behavior of the people in a stadium. From this viewpoint, the chapters of this thesis are related to cooperative behavior by the interplay between molecules, adatoms and surfaces including their electronic structure.

On the *intramolecular level* (Chapter 3) a thermally induced transition between two long-range-ordered commensurate molecular superstructures on Ag(111) was observed. This transition involves a conformational trans-cis inversion of the molecular adsorbates that is based on the rotation of an acetyl group around an amidic unit and influences intermolecular interactions. Hence, the trans-cis inversion is not expected for a *single* molecule on the surface. Moreover, it is not observed in solution [75]. Thus, the interplay between the molecules on the one hand and the molecules and the substrate on the other hand results in a conformational trans-cis inversion that the molecules “cooperatively undergo”.

On the *intermolecular level* (Chapter 4) the perylene derivative TAPP was studied on Cu(111). The homomolecular system TAPP/Cu(111) comprises different types of intermolecular interactions which involve weak vdW forces, coordination to Cu-adatoms and covalent bonds. Here, the interplay between the TAPP molecules, the Cu surface and its adatoms is thought to result in a “cooperative change” of intermolecular interactions between the TAPP molecules. In particular the formation of covalent bonds, having in mind the rapidly increasing number of publications reporting equivalent effects [27, 28, 30–33], underlines the potential of “surface chemistry” under ultraclean conditions (UHV) [26]. In the latter publication, Gourdon discusses the easily controllable broad temperature range used for evaporation or sample annealing, the confinement to two dimensions on the substrate surface and the independence from solubility as potentials of “surface chemistry”. The Cu-adatoms, which allow for metal coordination and may as well act catalytically for the chain formation, indicate that the substrate exceeds the role of a workbench on which chemical reactions may occur.

The “surface chemistry” studied in the work at hand is mainly based on a homomolecular approach in which the chemical reaction is induced by the appropriate choice of substrate and substrate temperature. Several other “tools” that are already well-established in surface science like co-deposition of molecules (see Chapter 3 and Section 4.2.2) or metal atoms (e.g. [19]) or the exposure to gas (e.g. [109]) could en-

rich this approach. The next step would be the formation of a long-range-ordered and highly stable surface structure in two dimensions. Here, the experimental results of our approach which is based on the formation of B-O bonds after a preceding dehydrogenation as well as [31,33] indicate that the missing self-correction is a challenge for the formation of homogeneous covalently bound surface structures [34].

On the level of *molecule substrate interaction* (Chapter 5) the influence of the substrate on strongly bound (chemisorbed) molecular adsorbates was discussed. The possibly stabilizing influence of the substrate on a porous molecular network, built up from dehydro-DPDI, was studied in detail by taking into account geometric (i.e. adsorption heights, XSW) as well as electronic aspects (i.e. valence band, ARPES) in order to explain the extraordinary stability of the network. Direct indications for a hybridization between molecular orbitals and the valence band of Cu(111) in the energy window between the Fermi energy and the Cu d-bands were not found. However, a hybridization with deep-lying molecular orbitals could not be excluded and the observed removal of degeneracy of d-bands at the  $\bar{\Gamma}$ -point clearly showed an influence of the porous network on the substrate electronic structure. In particular, in combination with the large adsorption height of dehydro-DPDI these results led to the conclusion that dehydro-DPDI, and especially its perylene core, is not directly involved in a strong interaction with the substrate. Instead, a new working hypothesis is carefully introduced in which “locally stabilizing” metal adatoms interact with the imine groups of dehydro-DPDI. However, this model still needs to be evidenced.

On the *supramolecular level* (Chapter 5) the influence of the porous dehydro-DPDI network as a long-range-ordered periodic structure on the substrate was studied. In this case the periodic perturbation of the otherwise free-electron-like surface state induced the formation of a weakly dispersive electronic band. From the perspective of the pores, which the surface state is confined in, the electronic band results from “cooperative behavior” between the confinements. This observation opens a completely new playground. Different pore sizes or pore geometries may significantly affect the formation of bands. These findings may also provide new insight into the behavior of molecular guests within porous host networks on surfaces [101,140], and the expected influence of the guests on the electronic band structure may even induce long-range effects for the host-guest behavior [141]. Moreover, the resulting electronic bands may play a decisive role in the stabilization of the porous networks themselves.

In our case the band formation is based on the periodic influence on the surface state, in [35] an electronic band is observed resulting from an interface state of a well ordered assembly of C<sub>60</sub> on Cu(111). In conjugated periodic molecular superstructures in two dimensions the delocalized molecular orbitals themselves may form bands and exhibit high charge carrier mobilities compared to molecular crystals [34]. The latter usually exhibit weakly delocalized electronic states due to their weak intermolecular interactions as well as weakly dispersive electronic bands [3]. For a conjugated system realized for example as long-range-ordered porous network molecular guests may influence the band structure and perhaps even induce transitions from conducting to semiconducting behavior. Hence, progress in “surface chemistry” goes hand in hand with the exploitation of physical/electronic properties and makes the study of molecules on surfaces a still exiting part of surface science.

# A Appendix to Chapter 3

## A.1 The interplay between enthalpy and entropy

A further example for the complex balance between enthalpy and entropy is based on the thermally induced formation of a porous molecular network by 4,9-diaminoperylene-quinone-3,10-diimine (DPDI) on Cu(111). This formation is described in detail in the thesis of Markus Wahl [36] and in [37]. Moreover, Chapter 5 is dedicated to additional studies on this system.

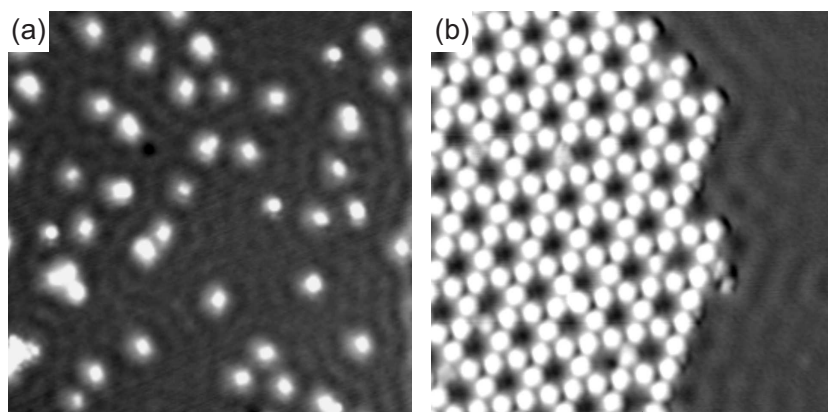


**Figure A.1:** Submonolayer coverage of DPDI on Cu(111) imaged at 4.7 K by STM. a) DPDI was deposited while the sample was held at RT ( $30.5 \times 30.5 \text{ nm}^2$ ,  $-0.1 \text{ V}/50 \text{ pA}$ ). b) Porous network of dehydro-DPDI whose formation is based on a thermally induced dehydrogenation of DPDI ( $21.4 \times 21.4 \text{ nm}^2$ ,  $-0.1 \text{ V}/50 \text{ pA}$ ). Standing wave patterns in the Shockley surface state of Cu(111), as they arise from scattering at the molecules, can be observed [46, 47].

Before annealing, STM images taken at RT indicate a mobile phase of DPDI [36, 37] what is a result of the missing possibility of attractive interactions between the molecules. Thus, enthalpy is not able to compensate for the loss of entropy that would occur during the aggregation of molecules in clusters. Even if the loss induced by entropy ( $T\Delta S$ ) is decreased by decreasing the temperature it cannot be compensated by enthalpy. Hence, DPDI is randomly immobilized and only forms clusters occasionally (Fig. A.1.a). However, after a thermally induced dehydrogenation, dehydro-DPDI can act as both H-bond donor and acceptor and thus, is able to overcome the loss of entropy during the formation of the ordered honeycomb network (Fig. A.1.b).

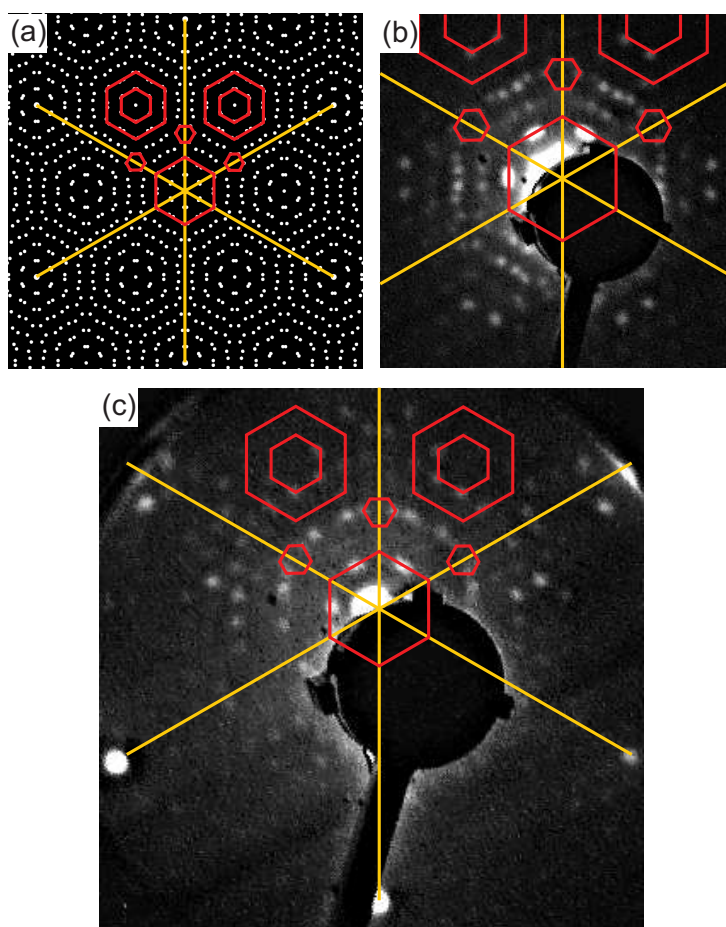


**Figure A.2:** LEED patterns for the porous network on Ag(111) formed by **3**. The yellow lines indicate the principal directions of the Ag substrate. The red lines highlight symmetries of the pattern in order to facilitate the comparison of the different figures. a) Simulated LEED pattern [68]. The LEED patterns were taken at energies of (b) 23 eV and (c) 37 eV.

## A.2 LEED of (3) on Ag(111)

LEED measurements were performed to determine the unit cell for both the hexagonal porous network and the close-packed assembly which is obtained after annealing the sample at 150°C. All LEED patterns were taken for samples held at room temperature (Fig. A.2.b and c for the porous network and Fig. A.3.a-c for the close-packed assembly).

The analysis of the LEED patterns supports for both molecular assemblies a superstructure which is commensurate to the underlying Ag substrate. For the porous network the following matrix describes the molecular ad-layer (Park and Madden) [79, 80]:

$$\begin{pmatrix} 11 & 1 \\ 10 & 1 \end{pmatrix}.$$

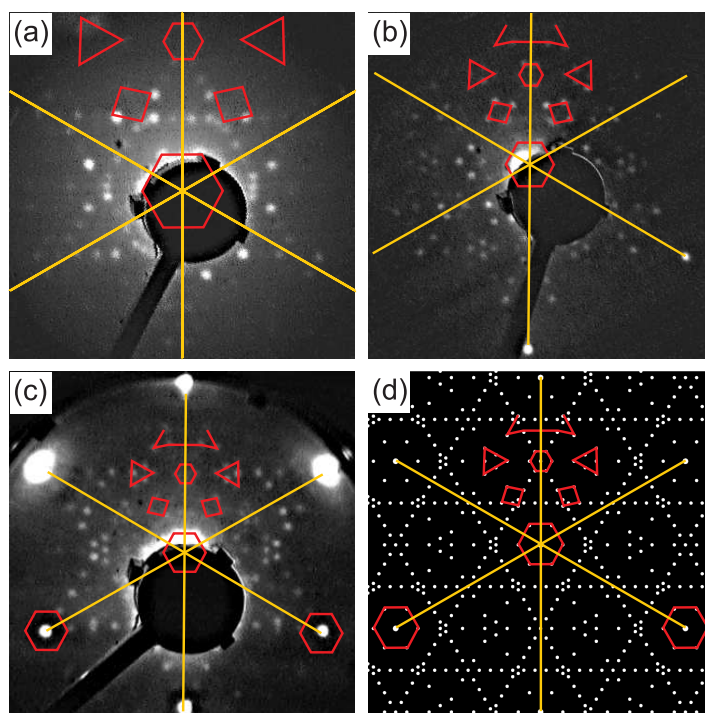


**Figure A.3:** LEED patterns for the close-packed assembly of **3** on Ag(111) observed after annealing at 150°C. The yellow lines indicate the principal directions of the Ag substrate. The red lines highlight symmetries of the pattern in order to facilitate the comparison of the different figures. The LEED patterns were taken at energies of (a) 15 eV, (b) 30 eV and (c) 42 eV. d) Simulated LEED pattern [68].

For the close-packed assembly the matrix reads as follows:

$$\begin{pmatrix} 8 & 3 \\ 2 & 4 \end{pmatrix}.$$

The information on the dimensions of the unit cell and the structural data of the molecule were used to determine the length of the H-bonds for the porous network. It was found that the CO···H distance amounts to about 2 Å.

The angle between the unit cell vectors of the hexagonal network and the close-packed structure was used to compare the STM results with the LEED results. We found that both measurement techniques lead to the same results (Fig. A.4). The following more detailed considerations support this statement.

As both assemblies could not be observed at the same time it is assumed that the sample is always mounted in the same way in the STM with respect to the x- and y-scanning directions of the STM and that no rotation of the sample with respect to these scanning directions happens. This is a reasonable assumption because the setup used for the STM experiments does not allow for a rotation of the sample.

The angle between both assemblies is unique except for an integer multiple of 60° that can be added (what is a result of the six-fold rotational symmetry of the topmost

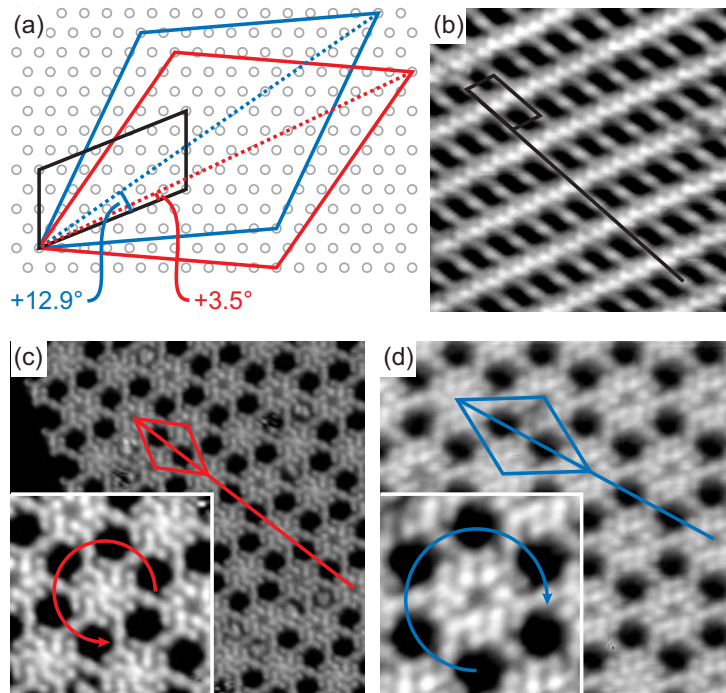


**Figure A.4:** a) Unit cell of the close-packed assembly (in black) and of the porous network with its mirrored counterpart (in blue and red, respectively). The geometry, the dimensions and the angles result from the LEED analysis (Appendix A.2). b) STM image of the close-packed assembly ( $10 \times 10 \text{ nm}^2$ ,  $-1.0 \text{ V}/20 \text{ pA}$ ). c-d) STM images of the porous network. c)  $20 \times 20 \text{ nm}^2$ , inset  $6.9 \times 6.9 \text{ nm}^2$ ,  $-1.7 \text{ V}/20 \text{ pA}$  d)  $12.4 \times 12.4 \text{ nm}^2$ , inset  $4.6 \times 4.6 \text{ nm}^2$ ,  $-1.3 \text{ V}/20 \text{ pA}$ . For both insets the chirality of the porous network is indicated, thus allowing to distinguish between mirrored patterns. The angles between the close-packed assembly and the porous network were determined by STM: (c)  $+4^\circ$  (red) and (d)  $+13^\circ$  (blue) and agree very well with the angles obtained from the LEED analysis (red and blue angle in a).

layer of the substrate). Moreover, the consideration of mirror-domains<sup>1</sup> leads to more than one possible angle between the two assemblies. For the close-packed assembly (Fig. A.4.a), the mirror operation results in non-congruent unit cells. Thus, an STM image of the close-packed assembly can unambiguously be attributed to one of the unit cells (either the unit cell or its mirrored counterpart) determined by LEED.

This attribution is not possible for the porous network as the mirror operation results in congruent unit cells (Fig. A.4.a). This means for our case that there are two possible angles which were determined to  $12.9^\circ$  and  $3.5^\circ$  (average of both unit cell vectors of the porous network minus angle of the long unit cell vector of the close-packed assembly, Fig. A.4.a). Both values compare very well with the angles derived from STM. However, as the STM provides “sub-unit-cell-resolution” it is possible to distinguish the chiral mirror domains of the porous network (Fig. A.4.c and d).

<sup>1</sup>Each domain can be mirrored at the principal directions of the substrate.



# B Appendix to Chapter 4

## B.1 Analysis of the metal coordinated close-packed assembly (assembly 2)

The dimensions of unit cells of different islands of assembly 2 and their rotation with respect to a common (arbitrarily chosen as the x-axis of the STM) straight line were determined according to Figure B.1.a. The aim was to gain information on the relationship between the substrate and the ad-layer in the following way.

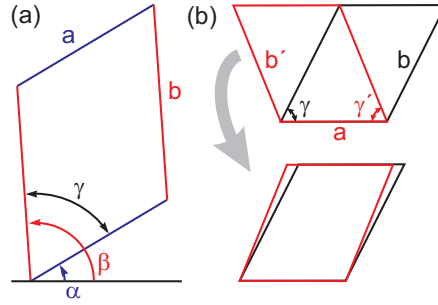


**Figure B.1:** Unit cells of assembly 2. a) Dimensions and orientation of the unit cell with respect to a straight line that is arbitrarily chosen. b) A unique determination of the unit cell is not possible as the difference between both unit cells (red and black parallelograms) lies within the error margin of the STM.

On the 111-surface rotations by  $60^\circ$  and mirror operations along the high symmetry directions lead to equivalent structures with respect to the substrate. As the mirror operations require information on the high symmetry directions only rotations were used to group the different unit cells. In doing so four non-congruent structures were found.

The use of a convention (e.g.  $\alpha < \beta$ ) to determine the orientation of the unit cell normally allows the distinction of the structures from their mirrored counterparts. (The mirrored counterpart should then exhibit  $\beta < \alpha$ ). However, this assembly bears the additional difficulty that the absolute value of the short diagonal of the unit cell  $\vec{b} - \vec{a}$  approximately equals  $\vec{b}$  (Fig. B.1.b). The deviation is only 4% and thus the structure cannot unambiguously be determined by STM.

The observation of four non-congruent structures may indicate that two of them are congruent if also mirror operations are considered. According to this assumption TAPP would then assemble in two independent structures. It is noted that the use of the above mentioned convention does not mix up the different structures as the

structures and their mirrored counterparts are in different groups. If it is known which structure is attributed to which mirrored counterpart,  $\gamma'$  and  $\vec{b}'$  of the mirrored structures can easily be transformed to  $\gamma$  and  $\vec{b}$  thus increasing the accuracy of the dimensions of the unit cells:

$$b = \sqrt{a^2 + (b')^2 - 2ab' \cdot \cos \gamma'}$$

$$\frac{b'}{\sin \gamma'} = \frac{b}{\sin \gamma} \Leftrightarrow \sin \gamma = \frac{b}{b'} \cdot \sin \gamma'.$$

In both cases (red and black parallelogram in Fig. B.1.b) the vector  $\vec{a}$  (absolute value and orientation) remains unchanged. If the hypothesis (two independent assemblies with their mirrored counterparts) was correct the two mirror axes, which are the average value of the two angles  $\alpha$  belonging to one structure and its mirrored counterpart, should be identical and furthermore correspond to the high symmetry directions (or to a direction rotated by  $90^\circ$  with respect to the high symmetry directions) of the substrate. If the angles  $\alpha$  of the four different structures were sorted in ascending order

$$\alpha_1 < \alpha_2 < \alpha_3 < \alpha_4$$

the following result would be expected:

$$\frac{\alpha_1 + \alpha_4}{2} \approx \frac{\alpha_2 + \alpha_3}{2} \approx [\text{angle of one of the mirror axes of the } 111 \text{ surface}].$$

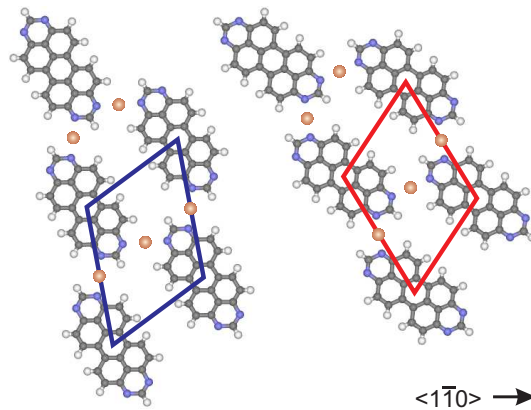


**Figure B.2:** Both structures of assembly 2. The black arrow indicates the high symmetry directions of Cu(111).

Indeed the three values differed by less than  $3^\circ$ . The angle of the high symmetry axis was determined by using an image with atomic resolution. Figure B.2 shows the resulting structures with respect to the high symmetry directions of Cu(111). The dimensions of the unit cells only differ within the error margin of the STM and were found to be  $(11 \pm 1.1) \text{ \AA} \times (13 \pm 1.3) \text{ \AA}$ , included angle:  $64^\circ \pm 4^\circ$ .

**Table B.1:** Number of Cu-adatoms/nm<sup>2</sup> estimated for different annealing temperatures and times.

	Number of Cu-adatoms/nm <sup>2</sup>	
	Needed	Provided according to [81]
Annealing at 40°C	0.28	1·10 <sup>-2±4</sup>
Annealing at 60°C	0.36	4·10 <sup>-2±4</sup>
Annealing at 85°C	0.18	2·10 <sup>-1±4</sup>

## B.2 The supply of the metal coordinated structures with Cu-adatoms

In order to gain information on the formation of the metal coordinated assemblies the samples were annealed at different temperatures and the determination of the number of converted molecules allowed an estimation of the number of Cu-adatoms needed for the conversion (Table B.1, second column). Compared to these values the density of free adatoms at room temperature of roughly 10<sup>-8</sup>/nm<sup>2</sup> [92] can be neglected.

The density of kinks [92], an assumed terrace width of typically 50 nm and the Arrhenius parameters [81] together with the time the system is annealed at a specific temperature enable a rough estimation of the number of Cu-adatoms/nm<sup>2</sup> that could be provided by the kinks. It is noted that the Arrhenius parameters were determined for temperatures around 200°C so that the range is extended to lower temperatures in our case which might induce further errors. The detachment of free adatoms diffusing along a step edge can be neglected as the energy for a detachment is higher than the energy for diffusion [142] so that the adatom will rather reach the next kink than it will detach.

The large error margin of the calculated values is due to the large error of the Arrhenius parameters [81]. The values estimated from the experiments (Table B.1, second column) are still within this error margin although a comparison of the densities of the Cu adatoms (Table B.1, second and third column) reveals that the number of Cu adatoms needed to form the metal coordinated assemblies clearly exceeds the number of adatoms that would detach from kinks at 40°C and 60°C. Furthermore the values in the third column should be considered as an upper limit as the system needs time to reach the annealing temperature whereas a constant annealing temperature is assumed for the calculations.

Thus, despite their inherent uncertainty these values indicate that the supply with Cu adatoms at temperatures around room temperature is not exclusively provided by Cu atoms detaching from kinks.

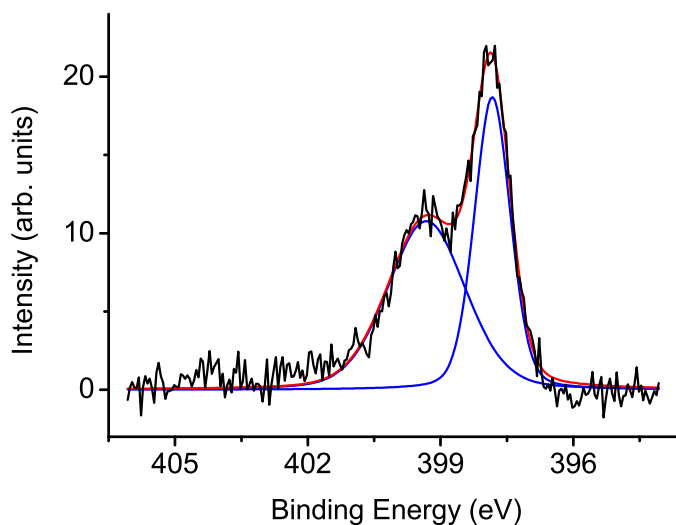


**Figure B.3:** XPS spectrum of the low temperature structures of TAPP. The substrate temperature during deposition as well as the sample temperature during the XPS experiment was  $-60^{\circ}\text{C}$ . For the preliminary fit two independently adjustable peak widths were used. The width of 1.0 eV for the peak at 397.8 eV (binding energy is shifted by  $-0.5$  eV with respect to the N1s peak of the porous network) agrees well to the width of 1.1 eV determined for the porous network at room temperature (Fig. 4.12). The width of the peak at 399.3 eV ( $+1.0$  eV with respect to the N1s peak of the porous network) was determined to 2.1 eV.

## B.3 Open questions

### TAPP/Cu(111): XPS of the low temperature assemblies

One open question refers to XPS measurements of the low temperature structures of TAPP (Section 4.1.1). The XPS spectrum depicted in Fig. B.3 exhibits a pronounced peak, shifted by 0.5 eV towards lower binding energies with respect to the N1s peak of the porous network used as reference in Section 4.1.3. Besides, a second broad peak is identified, shifted by 1.0 eV towards higher binding energies with respect to the same reference.

Until now, the second peak could not be explained as TAPP only exhibits *one* nitrogen species. Moreover, the low temperature structures observed with STM only indicate weak interactions between the TAPP molecules. However, if the second peak was related to a second nitrogen species a significant number of nitrogen atoms would need to be involved in quite strong interactions in order to explain the overall shift of 1.5 eV between both peaks.

### TAPP/Ag(111)

A second open question refers at first glance to a quite different aspect. At submonolayer coverages on Ag(111) TAPP assembles in two different close-packed structures

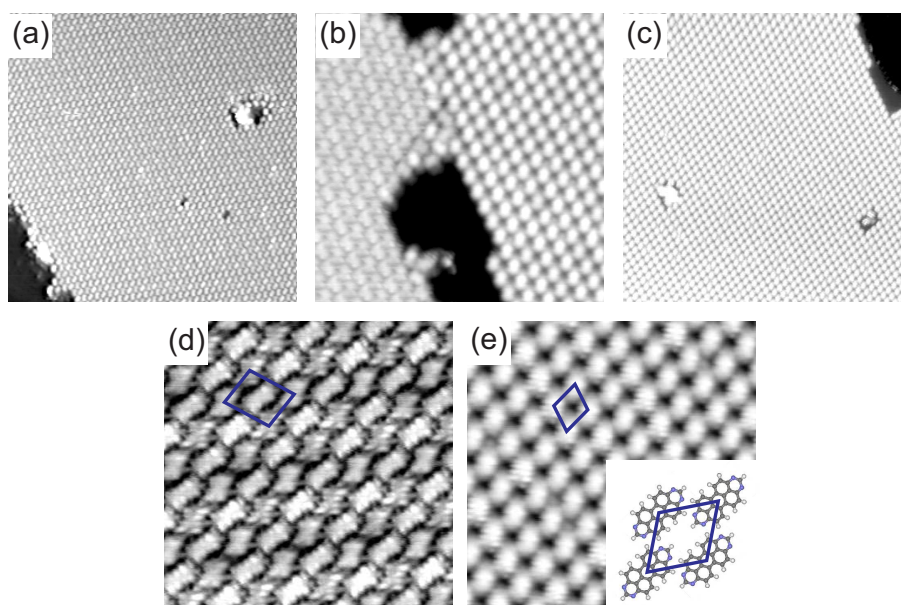


**Figure B.4:** STM study of a submonolayer of TAPP on Ag(111). The STM was operated at 77 K. Two close-packed assemblies were observed that form large homogeneous islands: a) After annealing at 155°C (45 x 45 nm<sup>2</sup>, -1.5 V/20 pA). b) Coexistence of both structures observed after annealing at 210°C (19 x 19 nm<sup>2</sup>, -1.3 V/20 pA). c) After annealing at 210°C (45 x 45 nm<sup>2</sup>, -1.3 V/20 pA) d) Detail of the structure observed in (a) (9 x 9 nm<sup>2</sup>, -1.5 V/20 pA). e) Detail of the structure observed in (c) with the corresponding tentative model as inset (11 x 11 nm<sup>2</sup>, -1.3 V/20 pA).

that could be observed at annealing temperatures of up to 210°C (Fig. B.4). Both assemblies form large homogeneous islands (Fig. B.4.a+c). At annealing temperatures of 300°C TAPP was observed to disassemble.

In Fig. B.4.d+e both structures are shown in detail. The dimensions of the unit cells are determined to  $(16 \pm 1.6) \times (12 \pm 1.2) \text{ \AA}^2$  with an included angle of  $(82 \pm 4)^\circ$  (Fig. B.4.d) and  $(11 \pm 1.1) \times (11 \pm 1.1) \text{ \AA}^2$  with an included angle of  $(68 \pm 4)^\circ$  (Fig. B.4.e), respectively. The tentative model shown in Figure B.4.e indicates weak vdW-interactions between the molecules.

At first glance the assembly shown in Figure B.4.d resembles the low temperature structure of TAPP on Cu(111) identified in Figure 4.2.b. The dimensions of the unit cells are comparable within the given error. For TAPP/Ag(111), the angle between principal molecular axes in neighboring “braids” was determined to  $(43 \pm 7)^\circ$ . Such an angle would support a chemical configuration that is not reasonable as two nitrogen atoms of neighboring molecules would directly face each other in this case. It is noted that the geometric analysis of surface structures with STM always involves errors. For the determination of unit cells, errors, e.g. due to imaging with a non-symmetric tip, are usually not relevant as “symmetry points” are used. However, for the determination of the aforementioned angle one has to rely on the “correct” imaging of the molecular topography by STM. Thus, the importance of this angle should not be overestimated.

Hence, both the structure of TAPP/Ag(111) shown in Fig. B.4.d and the low temperature assembly observed for TAPP/Cu(111) are related to the crystal structure of TAPP [76] as this structure provides a chemically reasonable model that fits to the unit cells derived for both surface structures.

### **Is there a relation between the angle and the XPS measurements?**

However, the aforementioned angle indicates that not every piece fits well in the puzzle. In this context it would be interesting if the highly-ordered surface structures of TAPP/Ag(111) also showed two N1s peaks in XPS. In this case, the models based on weak vdW interactions between TAPP molecules exhibiting only one chemical species may have to be reconsidered and the “odd angle” may become relevant.

# C Appendix to Chapter 5

## C.1 XSW: Separation of the nitrogen species

In order to discriminate between the amine (peak at lower binding energy, denoted as N1sL) and imine (peak at higher binding energy, N1sH) nitrogen of DPDI in the mobile phase, the spectra were fitted with two peaks. The corresponding peak intensities resulted in two photoelectron yield curves which were used to determine the coherent fraction and position for each nitrogen species (gray arrows in Fig. C.1).

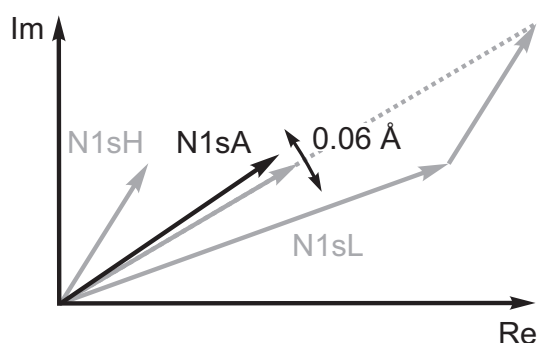


**Figure C.1:** Illustration of coherent fraction and position of the N1s species before annealing as complex numbers. The coherent fraction is represented by the absolute value whereas the coherent position is represented by the phase. The black arc exemplarily indicates a difference (of the coherent position) of  $0.06 \text{ \AA}$  to illustrate the errors that are dealt with. The gray arrows illustrate coherent fractions and positions that result from a separated analysis of the N1s peaks at low (N1sL) and high (N1sH) energy (standard analysis). For a cross-check their sum is compared to the coherent fraction and position that result from a direct determination of the overall intensity of both species (black arrow, N1sA).

In particular, the assumptions that are needed for the fits of the peaks may induce errors (Section 2.1.4). Thus, the reliability of the peak separation is checked in the following way: In Section 2.1.4 a straightforward strategy for the determination of the photoelectron yield curve is described in which the area of the peak(s)<sup>1</sup> is directly determined from the measured data. The reliability of this method is based on its simplicity (Section 2.1.4). However, if this strategy is used it is not possible to discriminate between both chemical species. Thus, a coherent fraction and position (black arrow, N1sA, in Fig. C.1) is determined which can be considered as a sort

<sup>1</sup>For the N1s spectra this would be the overall area of *both* peaks.

of average of the coherent vectors (i.e. the coherent fractions and positions) of the separated species. Such an average can be derived from the theory of XSW by using equation 2.4 on page 16 as a starting point [40] which is an expression for the XPS intensity of one chemical species in the standing wave field. In order to facilitate the argumentation the *cos*-term in that equation is replaced by a complex *exp*-term. The overall complex XPS intensity is then<sup>2</sup>:

$$\begin{aligned} \tilde{I}_G^{\text{XPS}} &\propto 1 + R + 2 \cdot \sqrt{R} \cdot F_{G,L} \cdot \exp\{i(\nu - 2\pi P_{G,L})\} \\ &\quad + 1 + R + 2 \cdot \sqrt{R} \cdot F_{G,H} \cdot \exp\{i(\nu - 2\pi P_{G,H})\} \\ &= 2 \cdot \left[ 1 + R + 2 \cdot \sqrt{R} \cdot e^{i\nu} \cdot \underbrace{\frac{1}{2} \left( F_{G,L} \cdot e^{-i \cdot 2\pi P_{G,L}} + F_{G,H} \cdot e^{-i \cdot 2\pi P_{G,H}} \right)}_{\equiv F_{G,A} \cdot \exp\{i(\nu - 2\pi P_{G,A})\}} \right] \end{aligned} \quad (\text{C.1})$$

$F_{G,L}, F_{G,H}, F_{G,A}$	Coherent fraction of N1sL, N1sH and N1sA
$P_{G,L}, P_{G,H}, P_{G,A}$	Coherent position of N1sL, N1sH and N1sA
$R = R(E)$	Reflectivity (cf. Fig. 2.1.c on page 14)
$\nu = \nu(E)$	Phase between the incident and reflected photon beam (cf. Fig. 2.1.c on page 14)
$\tilde{I}_G^{\text{XPS}} = \tilde{I}_G^{\text{XPS}}(E)$	Complex intensity of the photoelectrons of both nitrogen species.

Thus, the average coherent vector N1sA can easily be related to the coherent vectors of the separated species, N1sL and N1sH, by adding up the complex numbers in Fig. C.1. Both results, the sum and the average coherent vector N1sA, agree well. The average coherent fraction was determined to  $0.43 \pm 0.06$  whereas the average coherent position resulted in an adsorption height of  $2.29 \text{ \AA} \pm 0.04 \text{ \AA}$ . For the determination of the mean values 10 photoelectron yield curves were analyzed. The given error is the standard deviation.

It is noted that the height of  $2.29 \text{ \AA}$  agrees well to the mean value of the heights of the amine ( $2.20 \text{ \AA}$ ) and imine ( $2.4 \text{ \AA}$ ) nitrogens. Given the errors on the three coherent positions, a configuration in which the coherent fractions of the imine and amine nitrogens are comparable, can easily be imagined. Thus, the difference in coherent fraction is not interpreted in Section 5.1.1.

The good agreement between both results, which are based on different strategies (direct determination of the peak area vs. peak fit) corroborates that the adsorption heights of the nitrogen atoms are significantly lower than the height of the perylene core. Hence, the strong bending of DPDI in the mobile phase is further supported.

## C.2 ARPES studies of DPDI/Cu(111)

In Fig. C.2 the raw data of the photoemission intensity (bright color corresponds to high intensity) with respect to binding energy and emission angle ( $0^\circ$  corresponds to

<sup>2</sup>The real XPS intensity, which is not relevant in the following, is the real part of  $\tilde{I}_G^{\text{XPS}}$ .



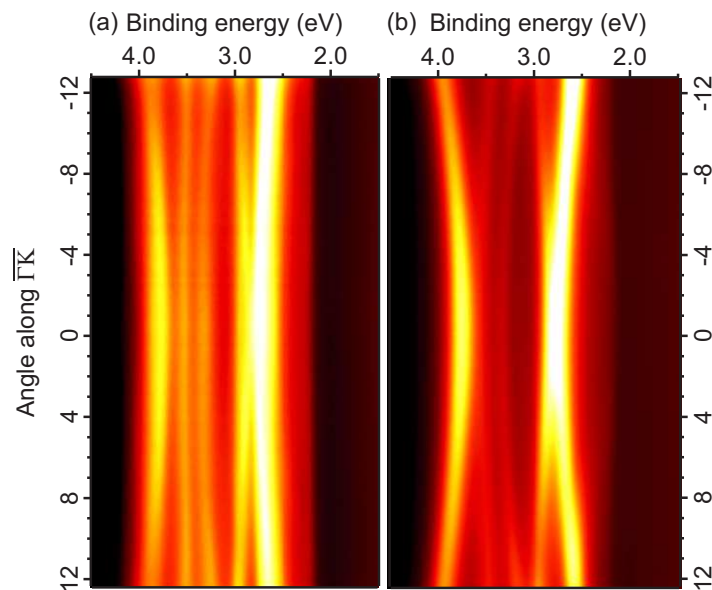


**Figure C.2:** Band dispersion of the d-bands for the porous network, measured at 7 K (a), and for Cu(111), measured at RT (b), along the  $\overline{\Gamma K}$  high symmetry direction. The measurements were performed at the CASSIOPEE end-station (Soleil). The comparison of both plots indicates the removal of degeneracy of the d-bands at normal emission on the sample covered by the porous network.

normal emission) is shown. The angle was changed along the  $\overline{\Gamma K}$  high symmetry direction. The intensity maxima that appear as vertical lines illustrate the dispersion of the five Cu d-bands that were measured for a sample covered by the porous network (Fig. C.2.a) and clean Cu (Fig. C.2.b). In Figure C.2.a the first two d-bands (from the left) are observed to be separated for all angles whereas these d-bands are degenerate at the  $\overline{\Gamma}$ -point ( $0^\circ$ , normal emission) in the case of clean Cu. Thus, the porous network induces a removal of degeneracy.

### C.3 Electronic states and bands

For isolated or weakly interacting molecules, localized electronic states, which are broadened in  $\vec{k}$  space due to their finite extent in real space, are expected at first glance. However, for sexithiophene on oxygen reconstructed Cu(110) [143] ARPES measurements were interpreted in terms of intra- and intermolecular *band dispersion*. The latter one was attributed to “coupling” between the periodically arranged molecules whereas the intramolecular band dispersion was understood as inter-ring overlap of thiophene orbitals which become delocalized over the length of the molecule. Even for “weakly” interacting molecules the bands can disperse strongly. This was observed for an interface state of  $C_{60}/Cu(111)$  where “coupling was mediated” by the surface [35]. In these cases the periodicity in momentum space matched the Brillouin zones of the superstructures.

In this context it is interesting whether the quantum mechanics of a surface superlattice are better described by isolated quantum well states or Bloch states in the superlattice. Berge et al. [144] discussed this issue for oxygen reconstructed Cu, Cu(110)(2x1)O. Moreover, such transitions between coherent emission from superlattice bands and incoherent emission from decoupled quantum well states were extensively studied for stepped surfaces. For stepped Cu(111) [145, 146] and Au(111) [132] “small” terrace widths indicated coherent emission from a superlattice band whereas “large” terrace widths indicated a terrace-confined quasi-one-dimensional state. For stepped Cu(111) this transition was found for a terrace width of 20 Å.

In our case, more information on the dispersion of the weak features in the ARPES measurements at the  $\bar{M}$  symmetry points is needed to discuss a possible relation to the peak found in STS on dehydro-DPDI.

## C.4 Quantum confinement

For a confinement in two-dimensional polygons with barriers of infinite height the eigenenergy of the ground state can be calculated according to [139] in the following way:

$$E[\text{eV}] = \frac{C}{m^*/m} \cdot \frac{1}{A[\text{nm}^2]} \quad (\text{C.2})$$

$E$	Eigenenergy of the groundstate in eV
$C$	Constants for the different geometries [139] : 0.75 eV·nm <sup>2</sup> (square), 0.72 eV·nm <sup>2</sup> (pentagon), 0.71 eV·nm <sup>2</sup> (hexagon), 0.69 eV·nm <sup>2</sup> (circle)
$m^*/m$	Ratio between reduced and real electron mass of the surface state [64]: 0.397 (Ag), 0.412 (Cu); in section 5.3 the average of 0.4 is used
$A$	Area of the polygon in nm <sup>2</sup> .

The influence of a finite barrier height on the eigenenergy of the ground state is exemplarily illustrated by the confinement in one dimension within a square potential of height  $V$ . A decrease of the pore size (higher values on x-axis) results in an increasing deviation between the eigenenergies of the confinement within barriers of finite height and the eigenenergies of the confinement within infinitely high barriers (Fig. C.3). This effect was observed in two dimensions in Section 5.3 (page 77).

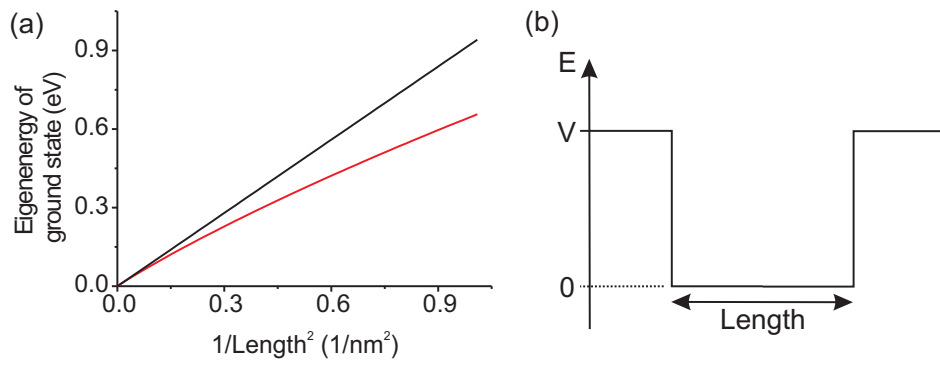


**Figure C.3:** Influence of a finite barrier height on the confinement in one dimension (e.g. [147]). a) The eigenenergy of the ground state for a confinement within barriers of infinite height (black) and within a square potential of  $V=1$  eV (red). b) The square potential in one dimension.



# Bibliography

- [1] Rick Rashid, *Why it's essential to invest in basic research during hard times*, Microsoft on the Issues, Blog (June 2009).
- [2] M. Schwoerer and H. C. Wolf, *Flach, flexibel und organisch*, Physik Journal der DPG **May 2008**, 29 – 32.
- [3] W. Brütting and W. Rieß, *Grundlagen der organischen Halbleiter*, Physik Journal der DPG **May 2008**, 33 – 38.
- [4] S. R. Forrest and M. E. Thompson, *Introduction: Organic Electronics and Optoelectronics*, Chemical Reviews **107**, 923–925 (2007).
- [5] D.-H. Kim, J.-H. Ahn, W. M. Choi, H.-S. Kim, T.-H. Kim, J. Song, Y. Y. Huang, Z. Liu, C. Lu, and J. A. Rogers, *Stretchable and Foldable Silicon Integrated Circuits*, Science **320**, 507 – 511 (2008).
- [6] W. Fix, *Elektronik von der Rolle*, Physik Journal der DPG **May 2008**, 47 – 50.
- [7] M. Klein and K. Heuser, *Lichthimmel und Lichttapeten*, Physik Journal der DPG **May 2008**, 43 – 46.
- [8] K. Leo, J. Blochwitz-Nimoth, and O. Langguth, *Vom Handy bis zum Fernseher*, Physik Journal der DPG **May 2008**, 39 – 42.
- [9] C. Deibel and V. Dyakonov, *Sonnenstrom aus Plastik*, Physik Journal der DPG **May 2008**, 51 – 54.
- [10] *nano.de-Report 2009 – Status Quo der Nanotechnologie in Deutschland*, Bundesministerium für Bildung und Forschung (2009).
- [11] C. Joachim, J. K. Gimzewski, and A. Aviram, *Electronics using hybrid-molecular and mono-molecular devices*, Nature **408**, 541 – 548 (2000).
- [12] C. Kenyon, A. Kornfeld, K. Kuhn, M. Liu, A. Maheshwari, W. Shih, S. Sivakumar, G. Taylor, P. VanDerVoorn, and K. Zawadzki, *Managing Process Variation in Intel's 45nm CMOS Technology*, Intel Technology Journal **12**, 93 – 110 (2008).
- [13] *Executive Summary*, in *International Technology Roadmap for Semiconductors (ITRS)* (2007).
- [14] *Emerging Research Devices*, in *International Technology Roadmap for Semiconductors (ITRS)* (2007).

- [15] W. Ho, *Single-molecule chemistry*, The Journal of Chemical Physics **117**, 11033 – 11061 (2002).
- [16] J. K. Gimzewski and C. Joachim, *Nanoscale Science of Single Molecules Using Local Probes*, Science **283**, 1683 – 1688 (1999).
- [17] S. De Feyter and F. C. De Schryver, *Two-dimensional supramolecular self-assembly probed by scanning tunneling microscopy*, Chemical Society Reviews **32**, 139 – 150 (2003).
- [18] J. V. Barth, J. Weckesser, N. Lin, A. Dmitriev, and K. Kern, *Supramolecular architectures and nanostructures at metal surfaces*, Applied Physics A: Materials Science & Processing **76**, 645 – 652 (2003).
- [19] U. Schlickum, R. Decker, F. Klappenberger, G. Zoppellaro, S. Klyatskaya, M. Ruben, I. Silanes, A. Arnau, K. Kern, H. Brune, and J. V. Barth, *Metal-Organic Honeycomb Nanomeshes with Tunable Cavity Size*, Nano Letters **7**, 3813 – 3817 (2007).
- [20] J. V. Barth, *Molecular Architectonic on Metal Surfaces*, Annual Review of Physical Chemistry **58**, 375 – 407 (2007).
- [21] D. Bonifazi, H. Spillmann, A. Kiebele, M. de Wild, P., F. Cheng, H.-J. Güntherodt, T. A. Jung, and F. Diederich, *Supramolecular Patterned Surfaces Driven by Cooperative Assembly of C<sub>60</sub> and Porphyrins on Metal Substrates*, Angewandte Chemie International Edition **43**, 4759 – 4763 (2004).
- [22] S. Weigelt, C. Busse, L. Petersen, E. Rauls, B. Hammer, K. V. Gothelf, F. Besenbacher, and T. R. Linderoth, *Chiral switching by spontaneous conformational change in adsorbed organic molecules*, Nature Materials **5**, 112 – 117 (2006).
- [23] M.-C. Blüm, M. Pivetta, F. Patthey, and W.-D. Schneider, *Probing and locally modifying the intrinsic electronic structure and the conformation of supported nonplanar molecules*, Physical Review B **73**, 195409 (2006).
- [24] T. A. Jung, R. R. Schlittler, and J. K. Gimzewski, *Conformational identification of individual adsorbed molecules with the STM*, Nature **386**, 696 – 698 (1997).
- [25] H. Wennerström and S. Lidin, *Scientific Background on the Nobel Prize in Chemistry 2007 "Chemical Processes on Solid Surfaces"*, The Royal Swedish Academy of Sciences (2007).
- [26] A. Gourdon, *On-Surface Covalent Coupling in Ultrahigh Vacuum*, Angewandte Chemie International Edition **47**, 6950 – 6953 (2008).
- [27] S. Weigelt, C. Busse, C. Bombis, M. M. Knudsen, K. V. Gothelf, T. Strunskus, Ch. Wöll, M. Dahlbom, B. Hammer, E. Laegsgaard, F. Besenbacher, and T. R. Linderoth, *Covalent Interlinking of an Aldehyde and an Amine on a Au(111) Surface in Ultrahigh Vacuum*, Angewandte Chemie International Edition **46**, 9227 – 9230 (2007).

- [28] L. Grill, M. Dyer, L. Lafferentz, M. Persson, M. V. Peters, and S. Hecht, *Nanoarchitectures by covalent assembly of molecular building blocks*, Nature Nanotechnology **2**, 687 – 691 (2007).
- [29] M. Matena, T. Riehm, M. Stöhr, T. A. Jung, and L. H. Gade, *Transforming Surface Coordination Polymers into Covalent Surface Polymers: Linked Polycondensed Aromatics through Oligomerization of N-Heterocyclic Carbene Intermediates*, Angewandte Chemie International Edition **47**, 2414 – 2417 (2008).
- [30] M. In't Veld, P. Iavicoli, S. Haq, D. B. Amabilino, and R. Raval, *Unique intermolecular reaction of simple porphyrins at a metal surface gives covalent nanostructures*, Chemical Communications pp. 1536 – 1538 (2008).
- [31] N. A. A. Zwaneveld, R. Pawlak, M. Abel, D. Catalin, D. Gigmes, D. Bertin, and L. Porte, *Organized Formation of 2D Extended Covalent Organic Frameworks at Surfaces*, Journal of the American Chemical Society **130**, 6678 – 6679 (2008).
- [32] S. Boz, M. Stöhr, U. Soydaner, and M. Mayor, *Protecting-Group-Controlled Surface Chemistry - Organization and Heat-Induced Coupling of 4,4prime-Di(tert-butoxycarbonylamino)biphenyl on Metal Surfaces*, Angewandte Chemie International Edition **48**, 3179 – 3183 (2009).
- [33] R. Gutzler, H. Walch, G. Eder, S. Kloft, W. M. Heckl, and M. Lackinger, *Surface mediated synthesis of 2D covalent organic frameworks: 1,3,5-tris(4-bromophenyl)benzene on graphite(001), Cu(111), and Ag(110).*, Chemical Communications pp. 4456 – 4458 (2009).
- [34] D. F. Perepichka and F. Rosei, *Extending Polymer Conjugation into the Second Dimension*, Science **323**, 216 – 217 (2009).
- [35] A. Tamai, A. P. Seitsonen, F. Baumberger, M. Hengsberger, Z.-X. Shen, T. Greber, and J. Osterwalder, *Electronic structure at the C<sub>60</sub>/metal interface: An angle-resolved photoemission and first-principles study*, Physical Review B **77**, 075134 (2008).
- [36] M. Wahl, *Reactions of Organic Molecules on Metal Surfaces studied by STM*, Ph.D. thesis, University of Basel (2006).
- [37] M. Stöhr, M. Wahl, C. H. Galka, T. Riehm, T. A. Jung, and L. H. Gade, *Controlling Molecular Assembly in Two Dimensions: The Concentration Dependence of Thermally Induced 2D Aggregation of Molecules on a Metal Surface*, Angewandte Chemie International Edition **44**, 7394 – 7398 (2005).
- [38] M. Henzler and W. Göpel, *Oberflächenphysik des Festkörpers*, B. G. Teubner (1994).
- [39] J. Zegenhagen, *Surface structure determination with X-ray standing waves*, Surface Science Reports **18**, 202 – 271 (1993).

- [40] D. P. Woodruff, *Surface structure determination using x-ray standing waves*, Reports on Progress in Physics **68**, 743 – 798 (2005).
- [41] E. J. Nelson, J. C. Woicik, P. Pianetta, I. A. Vartanyants, and J. W. Cooper, *Quadrupole effects in core and valence photoelectron emission from crystalline germanium measured via a spatially modulated x-ray interference field*, Physical Review B **65**, 165219 (2002).
- [42] A. Gerlach, F. Schreiber, S. Sellner, H. Dosch, I. A. Vartanyants, B. C. C. Cowie, T.-L. Lee, and J. Zegenhagen, *Adsorption-induced distortion of  $F_{16}CuPc$  on  $Cu(111)$  and  $Ag(111)$ : An x-ray standing wave study*, Physical Review B **71**, 205425 (2005).
- [43] J. Holton, *The Elves Manual*, <http://ucxray.berkeley.edu/~jamesh/elves/manual/>.
- [44] S. Hüfner, *Photoelectron Spectroscopy*, Springer (1996).
- [45] G. Binnig, H. Rohrer, Ch. Gerber, and E. Weibel, *Surface Studies by Scanning Tunneling Microscopy*, Physical Review Letters **49**, 57 – 61 (1982).
- [46] Y. Hasegawa and Ph. Avouris, *Direct observation of standing wave formation at surface steps using scanning tunneling spectroscopy*, Physical Review Letters **71**, 1071 – 1075 (1993).
- [47] M. F. Crommie, C. P. Lutz, and D. M. Eigler, *Imaging standing waves in a two-dimensional electron gas*, Nature **363**, 524 – 527 (1993).
- [48] S. Chiang, *Scanning Tunneling Microscopy Imaging of Small Adsorbed Molecules on Metal Surfaces in an Ultrahigh Vacuum Environment*, Chemical Reviews **97**, 1083 – 1096 (1997).
- [49] J. Repp, G. Meyer, S. M. Stojkovic, A. Gourdon, and C. Joachim, *Molecules on Insulating Films: Scanning-Tunneling Microscopy Imaging of Individual Molecular Orbitals*, Physical Review Letters **94**, 026803 (2005).
- [50] J. G. Simmons, *Generalized Formula for the Electric Tunnel Effect between Similar Electrodes Separated by a Thin Insulating Film*, Journal of Applied Physics **34**, 1793 – 1803 (1963).
- [51] J. Bardeen, *Tunnelling from a Many-Particle Point of View*, Physical Review Letters **6**, 57 – 59 (1961).
- [52] T. E. Feuchtwang, P. H. Cutler, and N. M. Miskovsky, *A theory of vacuum tunneling microscopy*, Physics Letters A **99**, 167 – 171 (1983).
- [53] J. Tersoff and D. R. Hamann, *Theory of the scanning tunneling microscope*, Physical Review B **31**, 805 – 813 (1985).



- 
- [54] A. D. Gottlieb and L. Wesoloski, *Bardeen's tunnelling theory as applied to scanning tunnelling microscopy: a technical guide to the traditional interpretation*, *Nanotechnology* **17**, R57 – R65 (2006).
- [55] V. A. Ukraintsev, *Data evaluation technique for electron-tunneling spectroscopy*, *Physical Review B* **53**, 11176 – 11185 (1996).
- [56] C. Wagner, R. Franke, and T. Fritz, *Evaluation of  $I(V)$  curves in scanning tunneling spectroscopy of organic nanolayers*, *Physical Review B* **75**, 235432 (2007).
- [57] B. Koslowski, C. Dietrich, A. Tschetschetkin, and P. Ziemann, *Evaluation of scanning tunneling spectroscopy data: Approaching a quantitative determination of the electronic density of states*, *Physical Review B* **75**, 035421 (2007).
- [58] A. Selloni, P. Carnevali, E. Tosatti, and C. D. Chen, *Voltage-dependent scanning-tunneling microscopy of a crystal surface: Graphite*, *Physical Review B* **31**, 2602 – 2605 (1985).
- [59] N. D. Lang, *Spectroscopy of single atoms in the scanning tunneling microscope*, *Physical Review B* **34**, 5947 – 5950 (1986).
- [60] L. Limot, T. Maroutian, P. Johansson, and R. Berndt, *Surface-State Stark Shift in a Scanning Tunneling Microscope*, *Physical Review Letters* **91**, 196801 (2003).
- [61] J. Kröger, L. Limot, H. Jensen, R. Berndt, and P. Johansson, *Stark effect in  $Au(111)$  and  $Cu(111)$  surface states*, *Physical Review B* **70**, 033401 (2004).
- [62] J. A. Stroscio, R.M. Feenstra, and A. P. Fein, *Electronic Structure of the  $Si(111) 2 \times 1$  Surface by Scanning-Tunneling Microscopy*, *Physical Review Letters* **57**, 2579 – 2583 (1986).
- [63] W. A. Hofer and A. Garcia-Lekue, *Differential tunneling spectroscopy simulations: Imaging surface states*, *Physical Review B* **71**, 085401 (2005).
- [64] F. Reinert, G. Nicolay, S. Schmidt, D. Ehm, and S. Hüfner, *Direct measurements of the  $L$ -gap surface states on the  $(111)$  face of noble metals by photoelectron spectroscopy*, *Physical Review B* **63**, 115415 (2001).
- [65] L. Bürgi, L. Petersen, H. Brune, and K. Kern, *Noble metal surface states: deviations from parabolic dispersion*, *Surface Science* **447**, L157 – L161 (2000).
- [66] A. Mugarza-Ezpeleta, *Electronic Structure of Low-Dimensional Systems Analyzed by Angle-Resolved Photoemission Spectroscopy*, Ph.D. thesis, University of the Basque Country (2002).
- [67] I. Horcas, R. Fernandez, J. M. Gomez-Rodriguez, J. Colchero, J. Gomez-Herrero, and A. M. Baro, *WSXM: A software for scanning probe microscopy and a tool for nanotechnology*, *Review of Scientific Instruments* **78**, 013705 (2007).

- [68] K. Hermann and M. A. van Hove, *LEED pattern simulator LEEDpat Version 2.1* (2006).
- [69] J.-M. Lehn, *Toward complex matter: Supramolecular chemistry and self-organization*, Proceedings of the National Academy of Sciences of the United States of America **99**, 4763 – 4768 (2002).
- [70] J. A. Theobald, N. S. Oxtoby, M. A. Phillips, N. R. Champness, and P. H. Beton, *Controlling molecular deposition and layer structure with supramolecular surface assemblies*, Nature **424**, 1029 – 1031 (2003).
- [71] A. Llanes-Pallas, M. Matena, T. A. Jung, M. Prato, M. Stöhr, and D. Bonifazi, *Trimodular Engineering of Linear Supramolecular Miniatures on Ag(111) Surfaces Controlled by Complementary Triple Hydrogen Bonds*, Angewandte Chemie International Edition **47**, 7726 – 7730 (2008).
- [72] F. H. Beijer, R. P. Sijbesma, J. A. J. M. Vekemans, E. W. Meijer, H. Kooijman, and A. L. Spek, *Hydrogen-Bonded Complexes of Diaminopyridines and Diaminotriazines: Opposite Effect of Acylation on Complex Stabilities*, The Journal of Organic Chemistry **61**, 6371 – 6380 (1996).
- [73] G. M. Whitesides, J. P. Mathias, and C. T. Seto, *Molecular self-assembly and nanochemistry: a chemical strategy for the synthesis of nanostructures*, Science **254**, 1312 – 1319 (1991).
- [74] N. Wintjes, *Tailoring Supramolecular Assemblies on a Metal Surface by Specifically Functionalized Porphyrins*, Ph.D. thesis, University of Basel (2007).
- [75] M. Matena, A. Llanes-Pallas, M. Enache, T. A. Jung, J. Wouters, B. Champagne, M. Stöhr, and D. Bonifazi, *Conformation-controlled networking of H-bonded assemblies on surfaces*, Chemical Communications pp. 3525 – 3527 (2009).
- [76] M. Matena, M. Stöhr, T. Riehm, S. Martens, J. Björk, M. S. Dyer, M. Persson, J. Lobo-Checa, K. Müller, H. Wadepohl, J. Zegenhagen, T. A. Jung, and L. H. Gade, *Aggregation and Contingent Metal/Surface Reactivity of Tetraazaperopyrene (TAPP) on Cu(111)*, accepted for publication in Chemistry - A European Journal .
- [77] T. Riehm, G. De Paoli, A. E. Konradsson, L. De-Cola, H. Wadepohl, and L. H. Gade, *Tetraazaperopyrenes: A New Class of Multifunctional Chromophores*, Chemistry - A European Journal **13**, 7317 – 7329 (2007).
- [78] K. Glöckler, C. Seidel, A. Soukopp, M. Sokolowski, E. Umbach, M. Böhringer, R. Berndt, and W. D. Schneider, *Highly ordered structures and submolecular scanning tunnelling microscopy contrast of PTCDA and DM-PBDCI monolayers on Ag(111) and Ag(110)*, Surface Science **405**, 1 – 20 (1998).

- 
- [79] K. Oura, V. G. Lifshits, A. A. Saranin, A. V. Zotov, and M. Katayama, *Surface Science – An Introduction*, Springer (2003).
- [80] D. E. Hooks, T. Fritz, and M. D. Ward, *Epitaxy and Molecular Organization on Solid Substrates*, *Advanced Materials* **13**, 227 (2001).
- [81] M. Giesen, *Scaling transition of the time dependence of step fluctuations on Cu(111)*, *Surface Science* **442**, 543 – 549 (1999).
- [82] L. H. Gade, *Koordinationschemie*, Wiley-VCH, Weinheim (1998).
- [83] S. Fölsch, P. Hyldgaard, R. Koch, and K. H. Ploog, *Quantum Confinement in Monatomic Cu Chains on Cu(111)*, *Physical Review Letters* **92**, 056803 (2004).
- [84] F. E. Olsson, M. Persson, A. G. Borisov, J.-P. Gauyacq, J. Lagoute, and S. Fölsch, *Localization of the Cu(111) Surface State by Single Cu Adatoms*, *Physical Review Letters* **93**, 206803 (2004).
- [85] S. Stepanow, N. Lin, and J. V. Barth, *Modular assembly of low-dimensional coordination architectures on metal surfaces*, *Journal of Physics: Condensed Matter* **20**, 184002 – 15 (2008).
- [86] C. C. Perry, S. Haq, B. G. Frederick, and N. V. Richardson, *Face specificity and the role of metal adatoms in molecular reorientation at surfaces*, *Surface Science* **409**, 512 – 520 (1998).
- [87] J. V. Barth, *Fresh perspectives for surface coordination chemistry*, *Surface Science* **603**, 1533 – 1541 (2009).
- [88] S. Stepanow, M. Lingenfelder, A. Dmitriev, H. Spillmann, E. Delvigne, N. Lin, X. Deng, C. Cai, J. V. Barth, and K. Kern, *Steering molecular organization and host-guest interactions using two-dimensional nanoporous coordination systems*, *Nature Materials* **3**, 229 – 233 (2004).
- [89] S. Stepanow, N. Lin, J. V. Barth, and K. Kern, *Surface-Template Assembly of Two-Dimensional Metal-Organic Coordination Networks*, *Journal of Physical Chemistry B* **110**, 23472 – 23477 (2006).
- [90] N. Lin, A. Dmitriev, J. Weckesser, J. V. Barth, and K. Kern, *Real-Time Single-Molecule Imaging of the Formation and Dynamics of Coordination Compounds*, *Angewandte Chemie International Edition* **41**, 4779 – 4783 (2002).
- [91] M. Schunack, F. Rosei, Y. Naitoh, P. Jiang, A. Gourdon, E. Laegsgaard, I. Stensgaard, C. Joachim, and F. Besenbacher, *Adsorption behavior of Lander molecules on Cu(110) studied by scanning tunneling microscopy*, *The Journal of Chemical Physics* **117**, 6259 – 6265 (2002).
- [92] M. Giesen, *Step and island dynamics at solid/vacuum and solid/liquid interfaces*, *Progress in Surface Science* **68**, 1 – 154 (2001).

- [93] M. Giesen and G. Schulze Icking-Konert, *Equilibrium fluctuations and decay of step bumps on vicinal Cu (111) surfaces*, Surface Science **412 – 413**, 645 – 656 (1998).
- [94] L. Bartels, G. Meyer, and K.-H. Rieder, *Basic Steps of Lateral Manipulation of Single Atoms and Diatomic Clusters with a Scanning Tunneling Microscope Tip*, Physical Review Letters **79**, 697 – 700 (1997).
- [95] F. Moresco, G. Meyer, K.-H. Rieder, H. Tang, A. Gourdon, and C. Joachim, *Low temperature manipulation of big molecules in constant height mode*, Applied Physics Letters **78**, 306 – 308 (2001).
- [96] F. Moresco, *Manipulation of large molecules by low-temperature STM: model systems for molecular electronics*, Physics Reports **399**, 175 – 225 (2004).
- [97] N. Lin, D. Payer, A. Dmitriev, T. Strunskus, Ch. Wöll, J. V. Barth, and K. Kern, *Two-Dimensional Adatom Gas Bestowing Dynamic Heterogeneity on Surfaces*, Angewandte Chemie International Edition **44**, 1488 – 1491 (2005).
- [98] D. Payer, A. Comisso, A. Dmitriev, T. Strunskus, N. Lin, Ch. Wöll, A. DeVita, J. V. Barth, and K. Kern, *Ionic Hydrogen Bonds Controlling Two-Dimensional Supramolecular Systems at a Metal Surface*, Chemistry - A European Journal **13**, 3900 – 3906 (2007).
- [99] L. H. Gade, C. H. Galka, K. W. Hellmann, R. M. Williams, L. De Cola, I. J. Scowen, and M. McPartlin, *Tetraaminoperylenes: Their Efficient Synthesis and Physical Properties*, Chemistry - A European Journal **8**, 3732 – 3746 (2002).
- [100] M. Wahl, M. Stöhr, H. Spillmann, T. A. Jung, and L. H. Gade, *Rotation-libration in a hierarchic supramolecular rotor-stator system: Arrhenius activation and retardation by local interaction.*, Chemical Communications pp. 1349 – 1351 (2007).
- [101] M. Stöhr, M. Wahl, H. Spillmann, L. H. Gade, and T. A. Jung, *Lateral Manipulation for the Positioning of Molecular Guests within the Confinements of a Highly Stable Self-Assembled Organic Surface Network*, Small **3**, 1336 – 1340 (2007).
- [102] A. Gerlach, S. Sellner, F. Schreiber, N. Koch, and J. Zegenhagen, *Substrate-dependent bonding distances of PTCDA: A comparative x-ray standing-wave study on Cu(111) and Ag(111)*, Physical Review B **75**, 045401 (2007).
- [103] S. Duhm, A. Gerlach, I. Salzmänn, B. Broeker, R.L. Johnson, F. Schreiber, and N. Koch, *PTCDA on Au(111), Ag(111) and Cu(111): Correlation of interface charge transfer to bonding distance*, Organic Electronics **9**, 111 – 118 (2008).

- 
- [104] A. Hauschild, K. Karki, B. C. C. Cowie, M. Rohlfing, F. S. Tautz, and M. Sokolowski, *Molecular Distortions and Chemical Bonding of a Large  $\pi$ -Conjugated Molecule on a Metal Surface*, Physical Review Letters **94**, 036106 (2005).
- [105] R. Rurali, N. Lorente, and P. Ordejon, *Comment on “Molecular Distortions and Chemical Bonding of a Large  $\pi$ -Conjugated Molecule on a Metal Surface”*, Physical Review Letters **95**, 209601 (2005).
- [106] A. Hauschild, K. Karki, B. C. C. Cowie, M. Rohlfing, F. S. Tautz, and M. Sokolowski, *Hauschild et al. Reply*, Physical Review Letters **95**, 209602 (2005).
- [107] L. Romaner, G. Heimel, J.-L. Bredas, A. Gerlach, F. Schreiber, R. L. Johnson, J. Zegenhagen, S. Duhm, N. Koch, and E. Zojer, *Impact of Bidirectional Charge Transfer and Molecular Distortions on the Electronic Structure of a Metal-Organic Interface*, Physical Review Letters **99**, 256801 (2007).
- [108] N. Koch, A. Gerlach, S. Duhm, H. Glowatzki, G. Heimel, A. Vollmer, Y. Sakamoto, T. Suzuki, J. Zegenhagen, J. P. Rabe, and F. Schreiber, *Adsorption-Induced Intramolecular Dipole: Correlating Molecular Conformation and Interface Electronic Structure*, Journal of the American Chemical Society **130**, 7300 – 7304 (2008).
- [109] K. Müller, *Organic Semiconductor Interfaces with Insulators and Metals*, Ph.D. thesis, Paul Scherrer Institute, Villigen (2009).
- [110] L. Kilian, A. Hauschild, R. Temirov, S. Soubatch, A. Schöll, A. Bendounan, F. Reinert, T.-L. Lee, F. S. Tautz, M. Sokolowski, and E. Umbach, *Role of Intermolecular Interactions on the Electronic and Geometric Structure of a Large  $\pi$ -Conjugated Molecule Adsorbed on a Metal Surface*, Physical Review Letters **100**, 136103 (2008).
- [111] Y. Zou, L. Kilian, A. Schöll, Th. Schmidt, R. Fink, and E. Umbach, *Chemical bonding of PTCDA on Ag surfaces and the formation of interface states*, Surface Science **600**, 1240 – 1251 (2006).
- [112] M. Eremtchenko, D. Bauer, J. A. Schäfer, and F. S. Tautz, *Polycyclic aromates on close-packed metal surfaces: functionalization, molecular chemisorption and organic epitaxy*, New Journal of Physics **6**, 4 (2004).
- [113] A. Bendounan, F. Forster, A. Schöll, D. Batchelor, J. Ziroff, E. Umbach, and F. Reinert, *Electronic structure of 1ML NTCDA/Ag(111) studied by photoemission spectroscopy*, Surface Science **601**, 4013 – 4017 (2007).
- [114] S. J. Chase, W. S. Bacsa, M. G. Mitch, L. J. Piloni, and J. S. Lannin, *Surface-enhanced Raman scattering and photoemission of  $C_{60}$  on noble-metal surfaces*, Physical Review B **46**, 7873 – 7877 (1992).

- [115] F. Forster, G. Nicolay, F. Reinert, D. Ehm, S. Schmidt, and S. Hufner, *Surface and interface states on adsorbate covered noble metal surfaces*, Surface Science **532** – **535**, 160 – 165 (2003).
- [116] F. Forster, A. Bendounan, J. Ziroff, and F. Reinert, *Systematic studies on surface modifications by ARUPS on Shockley-type surface states*, Surface Science **600**, 3870 – 3874 (2006).
- [117] R. Courths and S. Hüfner, *Photoemission experiments on copper*, Physics Reports **112**, 53 – 171 (1984).
- [118] J. Björk, *Private communication*.
- [119] J. Repp, G. Meyer, K.-H. Rieder, and P. Hyldgaard, *Site Determination and Thermally Assisted Tunneling in Homogenous Nucleation*, Physical Review Letters **91**, 206102 (2003).
- [120] J. Lobo-Checa, M. Matena, K. Müller, J. H. Dil, F. Meier, L. H. Gade, T. A. Jung, and M. Stöhr, *Band Formation from Coupled Quantum Dots Formed by a Nanoporous Network on a Copper Surface*, Science **325**, 300 – 303 (2009).
- [121] F. X. Redl, K.-S. Cho, C. B. Murray, and S. O'Brien, *Three-dimensional binary superlattices of magnetic nanocrystals and semiconductor quantum dots*, Nature **423**, 968 – 971 (2003).
- [122] A. L. Rogach, *Binary Superlattices of Nanoparticles: Self-Assembly Leads to "Metamaterials"*, Angewandte Chemie International Edition **43**, 148 – 149 (2004).
- [123] L. Gross, F. Moresco, L. Savio, A. Gourdon, C. Joachim, and K.-H. Rieder, *Scattering of Surface State Electrons at Large Organic Molecules*, Physical Review Letters **93**, 056103 (2004).
- [124] T. C. Chiang, *Photoemission studies of quantum well states in thin films*, Surface Science Reports **39**, 181 – 235 (2000).
- [125] M. F. Crommie, C. P. Lutz, and D. M. Eigler, *Confinement of Electrons to Quantum Corrals on a Metal Surface*, Science **262**, 218 – 220 (1993).
- [126] J. Kliewer, R. Berndt, and S. Crampin, *Scanning tunnelling spectroscopy of electron resonators*, New Journal of Physics **3**, 22 (2001).
- [127] J. Li, W.-D. Schneider, R. Berndt, and S. Crampin, *Electron Confinement to Nanoscale Ag Islands on Ag(111): A Quantitative Study*, Physical Review Letters **80**, 3332 – 3335 (1998).
- [128] H. Jensen, J. Kröger, R. Berndt, and S. Crampin, *Electron dynamics in vacancy islands: Scanning tunneling spectroscopy on Ag(111)*, Physical Review B **71**, 155417 (2005).

- 
- [129] Y. Pennec, W. Auwärter, A. Schiffrin, A. Weber-Bargioni, A. Riemann, and J.V. Barth, *Supramolecular gratings for tuneable confinement of electrons on metal surfaces*, Nature Nanotechnology **2**, 99 – 103 (2007).
- [130] U. Bischler and E. Bertel, *One-dimensional surface states (chain states) on a metal surface: H on Ni(110)*, Physical Review Letters **71**, 2296 – 2299 (1993).
- [131] O. Sanchez, J. M. Garcia, P. Segovia, J. Alvarez, A. L. Vazquez de Parga, J. E. Ortega, M. Prietsch, and R. Miranda, *Lateral confinement of surface states on stepped Cu(111)*, Physical Review B **52**, 7894 – 7897 (1995).
- [132] A. Mugarza and J. E. Ortega, *Electronic states at vicinal surfaces*, Journal of Physics: Condensed Matter **15**, S3281 – S3310 (2003).
- [133] C. P. Collier, R. J. Saykally, J. J. Shiang, S. E. Henrichs, and J. R. Heath, *Reversible Tuning of Silver Quantum Dot Monolayers Through the Metal-Insulator Transition*, Science **277**, 1978 – 1981 (1997).
- [134] N. Nicoara, E. Román, J. M. Gómez-Rodríguez, J. A. Martín-Gagoa, and J. Méndez, *Scanning tunneling and photoemission spectroscopies at the PTCDA/Au(111) interface*, Organic Electronics **7**, 287 – 294 (2006).
- [135] R. Temirov, S. Soubatch, A. Luican, and F. S. Tautz, *Free-electron-like dispersion in an organic monolayer film on a metal substrate*, Nature **444**, 350 – 353 (2006).
- [136] C. H. Schwalb, S. Sachs, M. Marks, A. Schöll, F. Reinert, E. Umbach, and U. Höfer, *Electron Lifetime in a Shockley-Type Metal-Organic Interface State*, Physical Review Letters **101**, 146801 (2008).
- [137] R. A. Shelby, D. R. Smith, and S. Schultz, *Experimental Verification of a Negative Index of Refraction*, Science **292**, 77 – 79 (2001).
- [138] D. R. Smith, J. B. Pendry, and M. C. K. Wiltshire, *Metamaterials and Negative Refractive Index*, Science **305**, 788 – 792 (2004).
- [139] E. Lijnen, L. F. Chibotaru, and A. Ceulemans, *Radial rescaling approach for the eigenvalue problem of a particle in an arbitrarily shaped box*, Phys. Rev. E **77**, 016702 – 9 (2008).
- [140] H. Dil, J. Lobo-Checa, R. Laskowski, P. Blaha, S. Berner, J. Osterwalder, and T. Greber, *Surface Trapping of Atoms and Molecules with Dipole Rings*, Science **319**, 1824 – 1826 (2008).
- [141] A. Kiebele, D. Bonifazi, F. Cheng, M. Stöhr, F. Diederich, T. A. Jung, and H. Spillmann, *Adsorption and Dynamics of Long-Range Interacting Fullerenes in a Flexible, Two-Dimensional, Nanoporous Porphyrin Network*, ChemPhysChem **7**, 1462 – 1470 (2006).

- [142] M. Karimi, T. Tomkowski, G. Vidali, and O. Biham, *Diffusion of Cu on Cu surfaces*, Physical Review B **52**, 5364 – 5374 (1995).
- [143] S. Berkebile, G. Koller, P. Puschnig, C. Ambrosch-Draxl, F. Netzer, and M. Ramsey, *Angle-resolved photoemission of chain-like molecules: the electronic band structure of sexithiophene and sexiphenyl*, Applied Physics A: Materials Science & Processing **95**, 101 – 105 (2009).
- [144] K. Berge, A. Gerlach, G. Meister, A. Goldmann, and E. Bertel, *Surface state confinement in a lateral quantum well: The striped Cu (110)(2x1)O surface*, Physical Review B **70**, 155303 (2004).
- [145] J. E. Ortega, S. Speller, A. R. Bachmann, A. Mascaraque, E. G. Michel, A. Nürmann, A. Mugarza, A. Rubio, and F. J. Himpsel, *Electron Wave Function at a Vicinal Surface: Switch from Terrace to Step Modulation*, Physical Review Letters **84**, 6110 – 6113 (2000).
- [146] F. Baumberger, M. Hengsberger, M. Muntwiler, M. Shi, J. Krempasky, L. Patthey, J. Osterwalder, and T. Greber, *Localization of Surface States in Disordered Step Lattices*, Physical Review Letters **92**, 196805 (2004).
- [147] Wolfgang Nolting, *Grundkurs Theoretische Physik 5/1*, Springer (2004).



# Acknowledgements

During the past years in Basel I could rely on many people whose support and advice is a substantial and vital part of my thesis.

I am grateful to **Prof. H. J. Güntherodt**, **Meike Stöhr** and **Thomas A. Jung** who gave me the opportunity to work in an inspiring scientific environment and granted me all the scientific freedom I wished to explore surface science with and beyond STM. I wish to thank Thomas for many helpful discussions and good ideas and the three of them for being referees of my thesis. I really appreciated the great support of my supervisor Meike. I gratefully acknowledge her time-consuming and excellent proof-reading of the thesis and other manuscripts, her availability for advice and discussion at all times and her inexhaustible knowledge of literature. I am also grateful for scientific experiences beyond the lab in Basel on many conferences, during external experiments (at synchrotrons) and in fruitful collaborations.

I wish to thank all my former and present colleagues with whom I shared a great time in Basel, **Serpil Boz**, **Andreas Kiebele**, **Sascha Koch**, **Nicholas Reynolds**, **Tomas Samuely**, **Silvia Schintke**, **Bartosz Such**, **Saranyan Vijayaraghavan**, **Jerome Wiss** as well as **Hannes Spillmann** and **Nikolai Wintjes** who introduced me to the LT-STM and whose support in particular at the beginning of my thesis I gratefully acknowledge. With Niko, there was another soul from Ruhrgebiet whose company I could enjoy on our journeys visiting home. I am also very grateful to **Markus Wahl** with whom I shared my first beam time and who put a lot of effort into the XSW project. I am deeply indebted to **Stefan Schnell** for his invaluable support in the lab, in particular for his assistance during repairs in which I could appreciate his always friendly and relaxed attitude. I am very grateful to **Mihaela Enache** for support in many experiments and proof-reading. Without **Kathrin Müller** and **Jorge Lobo-Checa** the spectroscopic experiments would not have been possible. I really appreciated their cooperation and am very grateful to both for proof-reading and for many discussions that substantially helped me to write this thesis. With Jorge I could enjoy several measurement and beam times in which he introduced me to ARPES.

I appreciated the collaboration with **Sonja Hölzl**, **Susanne Martens**, **Till Riehm** and **Prof. L. H. Gade** at the University of Heidelberg that did not only include helpful discussions and good ideas, but also warm hospitality and a friendly atmosphere. I am very grateful to Prof. Gade for many patient explanations to questions concerning chemistry and for being referee of my thesis. I also appreciated the friendly collaboration with **Jonas Björk**, **Matthew S. Dyer** and **Prof. Mats Persson**. Their theoretical studies essentially facilitated interpretation and validation of the experimental results. I am very grateful to Jonas for the many helpful discussions and answers to my questions. I gratefully acknowledge the collaboration with **Anna Llanes-Pallas**

and **Prof. Davide Bonifazi** who introduced me to supramolecular chemistry and the support from **Sebastian Thiess**, **Tien-Lin Lee** and **Jörg Zegenhagen** in the analysis of the XSW experiment.

I am grateful for the support from the mechanical and electronic workshops, in particular from **Andreas Tonin** and **Dominik Sifrig**, the assistance of **G. Weaver**, **A. Fischer**, **B. Kammermann** and **A.' Kalt** with the omnipresent bureaucracy and creative support from **Timothy Ashworth**, **Klaus Rodemann** and **Anja Matena**.

Finally, my heartfelt thanks go to **my parents** and **my sisters and their families** who always warmly welcome me, make me feel home and offer me a relaxing time during every visit. I also wish to thank **my friends in Ruhrgebiet** for making my visits there even more enjoyable.

# Publications

- M. Matena, M. Stöhr, T. Riehm, S. Martens, J. Björk, M. S. Dyer, M. Persson, J. Lobo-Checa, K. Müller, H. Wadepohl, J. Zegenhagen, T. A. Jung, and L. H. Gade, *Aggregation and Contingent Metal/Surface Reactivity of Tetraazaperopyrene (TAPP) on Cu(111)*, accepted for publication in Chemistry - A European Journal.
- J. Lobo-Checa, M. Matena, K. Müller, J. H. Dil, F. Meier, L. H. Gade, T. A. Jung, and M. Stöhr, *Band Formation from Coupled Quantum Dots Formed by a Nanoporous Network on a Copper Surface*, Science **325**, 300 – 303 (2009).
- M. Matena, A. Llanes-Pallas, M. Enache, T. A. Jung, J. Wouters, B. Champagne, M. Stöhr, and D. Bonifazi, *Conformation-controlled networking of H-bonded assemblies on surfaces*, Chemical Communications, 3525 – 3527 (2009).
- A. Llanes-Pallas, M. Matena, T. A. Jung, M. Prato, M. Stöhr, and D. Bonifazi, *Trimodular Engineering of Linear Supramolecular Miniatures on Ag(111) Surfaces Controlled by Complementary Triple Hydrogen Bonds*, Angewandte Chemie International Edition **47**, 7726 – 7730 (2008).
- M. Matena, T. Riehm, M. Stöhr, T. A. Jung, and L. H. Gade, *Transforming Surface Coordination Polymers into Covalent Surface Polymers: Linked Polycondensed Aromatics through Oligomerization of N-Heterocyclic Carbene Intermediates*, Angewandte Chemie International Edition **47**, 2414 – 2417 (2008).
- A. Bannani, C. A. Bobisch, M. Matena, and R. Möller, *Ballistic electron emission spectroscopy on Ag/Si devices*, Nanotechnology **19**, 375706 (2008).
- C. Bobisch, A. Bannani, M. Matena, and R. Möller, *Ultrathin Bi films on Si(100)*, Nanotechnology **18**, 055606 (2007).



# Curriculum vitae

## Persönliche Daten

Name	Manfred Matena
Geburtsort und -tag	Essen, 13.08.1981
Staatsangehörigkeit	deutsch

## Schulbildung

1987 bis 1991	Grundschule in Essen
1991 bis 2000	Gymnasium in Essen
	Abschluss: Abitur (Notendurchschnitt: 1,0)

## Zivildienst

2000 bis 2001	Zivildienst im katholischen Jugendamt in Essen
---------------	--

## Hochschulstudium

2000 bis 2001	Zweisemestriges Teilzeitfernstudium der Physik an der Universität Kaiserslautern (FiPS)
2001 bis 2005	Physikstudium an der Universität Duisburg-Essen
2004 bis 2005	Diplomarbeit in der Gruppe von Prof. Möller Titel: "Mikroskopie mit ballistischen Elektronen" Abschluss: Diplomphysiker (mit Auszeichnung)
Seit 2006	Doktorarbeit an der Universität Basel in der Gruppe von Prof. Güntherodt

## Stipendium

2003 bis 2005	Stipendiat des Cusanuswerks (Begabtenförderungswerk der katholischen Kirche)
---------------	---

Folgenden Dozentinnen und Dozenten verdanke ich meine Ausbildung:

A. Guthmann (K), H. J. Jodl (K), H. J. Korsch (K), H. F. Döbele (DE), G. Frey (DE), H. Frentzen (DE), M. Goedicke (DE), R. Graham (DE), F. Haake (DE), G. Hackenbroich (DE), J. Krug (DE), K. Lebelt (DE), D. von der Linde (DE), R. Möller (DE), H. Nienhaus (DE), T. van Tran (DE), R. Unland (DE), G. Wolf (DE), A. Wucher (DE), H.-J. Güntherodt (BS), M. Stöhr (BS)

K: Universität Kaiserslautern, DE: Universität Duisburg-Essen, BS: Universität Basel